Lehrstuhl für Theoretische Chemie
der Technischen Universität München

Photo-induced Nonadiabatic Dynamics of Aromatic Molecules via Conical Intersections. Electronic-structure and Time-dependent Quantum Dynamics Calculations

Zhenggang Lan

Vollständiger Abdruck der von der Fakultät für Chemie der Technischen Universität München zur Erlangung des akademischen Grades eines

Doktors der Naturwissenschaften

genehmigten Dissertation.

Vorsitzender:		Univ.-Prof. Dr. Kai-Olaf Hinrichsen
Prüfer der Dissertation:	1.	Univ.-Prof. Dr. Wolfgang Domcke
	2.	Univ.-Prof. Dr. Hans Jürgen Neusser
	3.	Univ.-Prof. Dr. Steffen Johannes Glaser

Die Dissertation wurde am 22.02.2007 bei der Technischen Universität München eingereicht und durch die Fakultät für Chemie am 18.04.2007 angenommen.

Photo-induced Nonadiabatic Dynamics of Aromatic Molecules via Conical Intersections. Electronic-structure and Time-dependent Quantum Dynamics Calculations

Zhenggang Lan
Directed by Professor Wolfgang Domcke
Department of Chemistry
Technical University of Munich
Garching D-85748, Munich, Germany

February 2007

To

My Mother, Min Wang

My Father, Qiying Lan

and

My Wife, Yi Tan

Acknowledgments

In this special winter (2006/07), I finish my doctoral thesis in the Institute of Theoretical Chemistry at the Technical University of Munich, as the epilogue of my student life and the prologue of my future career in chemical physics. The forthcoming doctor degree has a special meaning for my 30 year's age: an old Chinese proverb says "a 30-year-old man should plant his feet firmly on the ground." Before the discussion of my doctoral work, I would like to express my great gratefulness to all people who have been significant for my life in the last 30 years.

First and foremost, I would like to express my great gratitude to my advisor, Prof. Wolfgang Domcke, for his guidance, support and inspiration of my work. He introduced me to the wonderful realm of conical intersections and offered me an excellent opportunity to develop my knowledge of theoretical chemistry. From the close interactions and discussions with him from time to time, I have benefitted a lot, both for the theoretical solutions of particular chemical problems, as well as for the broad view of the field of theoretical chemistry. In addition, Prof. Domcke supported me to attend many academic conferences and to make several short-term visits of other laboratories. All of these communications greatly broadened my scope and deepened my understanding of many fields of chemical physics. Most importantly, I begin to realize, although still not completely clear, the answer to a fundamental question: "What is science and what are scientific questions".

I am also indebted to all collaborators, who have been involved in direct or indirect cooperations during my doctoral work. From many simulating discussions with Prof. A. L. Sobolewski, I have learned to understand many interesting photochemical properties of aromatic biomolecules. During the long-term collaboration with Dr. V. Vallet, I learned a lot about electronic-structure theory. I enjoyed many important discussions with Dr. C. Woywod concerning the basic knowledge of conical intersections. Dr. A. Dupays show me many beautiful insights into physics and mathematics, from the view of a pure theoretical physicist. From the critical questions of Dr. O. Vieuxmaire and Dr. A. Motzke, I

learned the correct attitude to scientific work. Although Prof. S. Mahapatra is in Hyderabad in India, far from Germany, his helpful comments improved my understanding of important questions. I thank them for the happy cooperation time.

I would like to express my great thanks to Dr. M. Thoss, Dr. C. Woywod, Dr. O. Vieuxmaire, L. Zimmerman for their proof reading and corrections for this thesis. I benefit a lot through their invaluable suggestions, both for science and for language.

During my doctoral work, I received much support from everyone in the institute, concerning both the science, as well as the daily life. Particularly, I would like to thank Dr. M. Thoss, Dr. W. Eisfeld, Dr. C. Scheurer, Dr. A. Markmann, Dr. D. Egorova, Dr. L. M. F. Gaite, Dr. S. Mishra, Dr. I. Kondov and J. Li for many instructive discussions. I also thank the secretary, Frau. R. Mösch, for her help. In fact, all members of the institute made my stay here truly enjoyable.

My life in the last three years has been enriched by many friends in Munich. During this period, we shared many wonderful experiences. I believe that we can develop our future careers by mutual support.

I am very glad that I had the opportunitiy to visit the Tohuko University in Sendai, Japan, the Institute of Physics in Warsaw, Poland and the Freie Universität in Berlin. I would like to deeply thank Prof. Y. Fujimura, Prof. Y. Ohtsuki, Prof. Kono and their group members for their assistance during my stay in Japan and many helpful discussions with them. I also thank Prof. A. L. Sobolewski for inviting me to his group for a short-term visit. I am really appreciated the happy time which I could spend with his group members, Dr. M. Rode, Dr. S. Perun and B. Chmura. I also should mention that Prof. J. Manz provided me the chance to visit his group and exchange scientific ideas.

Most important of all, I would like to express my thanks to my parents and my wife. My parents always supported and encouraged me in my life. They always give their love to me and are proud of me all the time, while I really regret that I could not spend sufficient time with them since the beginning of university time.

Munich is a unique place for me because I met my wife here. As a Chinese man, the family is one of the most important parts of my life. I really wish that I could make her happy forever to thank her for her love and her care for me.

Abstract

This thesis focuses on the photoinduced ultrafast dynamics of aromatic molecules through conical intersections. Pyrrole and phenol are selected as two typical systems to explore the dissociation dynamics via repulsive $^1\pi\sigma^*$ states and the nonadiabatic transitions at conical intersections. Electronic-structure calculations are employed to identify the relevant degrees of freedom of the chemical reactions. In a first approximation, reduced-dimensional models, including the NH or OH stretching motion and the relevant coupling coordinates of the conical intersections, are considered to capture the main features of the hydrogen-detachment photochemistry of pyrrole and phenol. Diabatic potential-energy surfaces have been obtained based on *ab inito* data and a suitable diabatization procedure. Quantum wave-packet calculations have been performed to explore the photoinduced dissociation and internal-conversion dynamics of these molecules. The electronic population transfer processes at the conical intersections, the branching ratio for the different dissociation channels, the internal-conversion probability, and their dependence on the initial preparation of the system have been investigated for both pyrrole and phenol. It is shown that the excitation of the NH or OH stretching motion strongly enhances the photodissociation rate, while the excitation of the strongest coupling mode has a pronounced effect on the branching ratio of the photodissociation process. Time-dependent wavepackets are displayed to provide the insight into the photodissociation dynamics through conical intersections. To exhibit the role of vibrational relaxation effects on the nonadiabatic transition dynamics, we apply the reduced density-matrix formalism. With these methods, we explore the main features of the quantum dissipative dynamics of pyrrole through conical intersections. The internal conversion probability is enhanced when the coupling of the active degrees of freedom with the environment is taken into account. The cooling of the system by the coupling with the environment is visualized by time-dependent nuclear density probabilities of the system degrees of freedom.

Contents

Chapter 1

Introduction

1.1 History of the concepts of conical intersections

The interaction between light and matter raises many important subjects and is becoming one of the central research topics in today's physical chemistry [1–4]. The electronic excitation of a molecular system after the absorption of a photon induces a complex sequence of dynamical processes, which are conventionally classified as photophysical and photochemical processes. The former refer to the situations in which a molecule retains in its chemical identity, while the latter imply that the photoexcited molecules have undergone chemical reactions. These dynamical processes are of interest both from experimental and theoretical points of view, because all life on earth depend on, directly and indirectly, the sun's visible and ultraviolet radiation. In fact, the conversion of solar energy by photosynthesis not only permits the continued existence of life on the planet, but also is important for the evolution of life.

The photophysical processes include radiative electronic transitions (*e.g.* fluorescence, phosphorescence) and nonradiative electronic transition (*e.g.* internal conversions and intersystem crossing). The photochemical processes, on the other hand, refer to photoinduced chemical reactions, such as photoionization, photodissociation, photolysis, photosynthesis and photoinduced isomerization [1].

Although photoinduced processes became an important research topic in the early part of last century, the mechanisms behind them were not known. For example, the existence of metastable states had already been known, but their importance in photoinduced processes was not recognized. It was not clear whether the well-established electronic-structure theories based on the Born-Oppenheimer (BO) approximation [5] for the ground state were applicable to electronic excited states. The early attempts of Kasha and Vavilov to treat the lowest excited states of each multiplicity within the BO framework could not explain many photoinduced processes. The reason is that many photoinduced processes, such as internal conversion, intersystem-crossing, electron transfer, as well as most photochemical reaction, are governed by transitions between different BO adiabatic electronic states. These so-called nonadiabatic transitions induced by the non-BO coupling between different electronic states cause the breakdown of the BO approximation [4]. The efforts to understand these nonadiabatic phenomena have been a central topic of research until today. The reason is that with the development of the time-resolved laser spectroscopy, it has been realized that nonadiabatic transitions exist in all kinds of molecular reaction processes [6, 7], in particular for polyatomic molecular systems.

Many nonadiabatic transitions, in particular the ultrafast ones, are governed by the strong non-BO couplings which arise when different electronic potential-energy (PE) surfaces come close to each other or cross. These non-BO couplings exist, in particular at conical intersections, which are defined as points (actually hypersurfaces in the multidimensional nuclear coordinate space) where different electronic PE surfaces touch. Today, it has been realized that this degeneracy is a very common phenomenon in polyatomic systems, and the understanding of conical intersections is undergoing a spectacular transformation.

In the first half of last century, the role of conical intersections was little appreciated. The earliest discussion about surface crossings was given by Hund in 1927 [8], the same year in which the BO approximation was formulated [5]. He provided the following argument: If potential curves cross, two electronic states must be degenerate at the crossing point. However, this degeneracy cannot be

established if only one parameter is varied. Thus, the PE curves of diatomic molecules will not cross by varying the nuclear distance unless these two states differ in some essential way. Two years later (1929), von Neumann and Wigner gave the mathematical formulation of this argument [9]. They formulated the famous non-crossing rule, which became the foundation of all further discussions. In 1937, Teller [10] reviewed the non-crossing rule again and found that crossings can exist in polyatomic systems because "the whole atomic configuration, not only a single interatomic distance, can be varied". He also indicated that the energy surfaces near the crossing point form a double cone. This was the first time that the concept of the conical intersection was defined, as well as its topography. In this remarkable paper, he emphasised that transitions between different electronic surfaces take place by passing through the crossing point of the double cone, such as the Jahn-Teller (JT) case [11], Renner-Teller (RT) case [12] and curve-crossings in polyatomic systems.

The knowledge of conical intersections was quite limited after these early studies, although this idea was still mentioned occasionally. In 1957, Kauzmann assumed that, due to the existence of many degrees of freedom, as well as the complexity of the PE surfaces, of polyatomic molecules, "these cross-overs are not unusual in molecules" [13]. In 1963, Herzberg and Longuet-Higgins first noticed the geometric phase effect of conical intersections [14]. They showed that the phase change of the electronic wavefunctions provided direct evidence of the existence of a conical intersection. They concluded that conical intersections not only exist in symmetrical systems (JT effect), but also in asymmetrical systems such as three dissimilar hydrogen-like-atoms. Later, efforts were made to determine the surface crossings with the help of newly-developed electronic-structure theories. For example, Zimmerman developed molecular-orbital (MO) correlation diagrams in 1966 to predict the existence of conical intersections based on the symmetry of reactants and products for the photochemical cyclization of butadiene to cyclobutene [15]. The PE surfaces of the ground and excited states for this reaction were obtained by van der Lugt and Oosterhoff in 1969 [16]. This is the first successful attempt to obtain the geometry of a surface crossing with

ab inito calculations in a polyatomic molecule, while the knowledge about conical intersections was still limited. In 1970, Förster introduced the concepts of "adiabatic" and "diabatic" photoreactions [17]. In 1971, Dougherty suggested a perturbation approach based on the MO theory to treat the breakdown of the BO approximation in nonadiabatic transitions [18]. The symmetry properties of the molecular orbitals were also employed by Evleth, Horowitz and Lee in 1973 to predict surface crossings between the $^1\pi\sigma^*$ and S_0 states, taking place for the stretching of NH or OH bonds in imidazolyl and related heteroradicals [19].

In 1974, Michl [20], in a review article on the understanding of organic photochemistry in terms of the MO theory, stated that true surface touchings are "uncommon" and "strongly avoided". He referred to conical intersections as the "funnels" of photochemistry and suggested that a molecule can be transferred to the electronic ground state when the nuclear wave packet (WP) accesses one of these funnels. In the same year, as an extension to Zimmerman's work, Salem systematically investigated the PE surfaces for a few prototype photochemical reactions and discussed their common features, in particular the decays through surface crossings [21]. In 1975, Longuet-Higgins emphasized that conical intersections widely exist in polyatomic systems, even for systems with no symmetry [22]. In addition, he tried to classify the types of conical intersections according to their symmetry properties. For highly symmetrical molecules (e.g. JT systems), conical intersections occur in highly symmetrical configurations. On the other hand, less symmetrical molecules also can exhibit conical intersections at particular nuclear geometries which cannot be determined by symmetry arguments alone.

At the end of the 1980s, the development of *ab initio* methods in quantum chemistry, in particular the configuration interaction (CI) approach, provided powerful tools to compute excited PE surfaces and localize conical intersections. This opened the modern era in the theory of conical intersections. This new era began with the characterization of conical intersections for several biradicals, performed by Bonačić-Koutecký, Koutecký and Michl in 1987 [23]. More systematic investigations have been performed by the groups of Yarkony [4, 24–26] and Ruedenberg [27] for small molecules, as well as by the team of Robb, Bernari and

Olivucci [4, 28–30] for larger organic molecules. Armed with new algorithms and powerful computers, these groups showed that conical intersections are in fact very common in many photochemical reactions, rather than "relatively uncommon", as previously believed. Several researchers have developed highly efficient algorithms to localize the minima of the seams of intersection in multi-dimensional spaces [4, 24, 26, 28–30]. Their contributions, which are implemented in standard quantum chemistry packages, such as GAUSSIAN [31] and COLUMBUS [32], permit us to search systematically for conical intersections. The discussion of the role of conical intersections in photoinduced reactions is now an important topic in standard textbooks of photochemistry [33].

Although the development of electronic-structure methods has improved our knowledge of conical intersections, one needs to understand the dynamics at conical intersections to acquire a complete picture of photoinduced reactions. Such calculations are quite challenging, because the nonadiabatic dynamics involves the strong mixing of several electronic states induced by nuclear displacements.

Early attempts to treat the dynamics at conical intersections were based on the Landau-Zener-Stückelberg approach [10,34–36]. While these treatments provided a transparent picture of nonadiabatic transitions in one-dimensional avoided-crossing situations, their extension to multi-dimensional cases are nontrivial and no quantitative results for electronic population probabilities and transition rates have been obtained in these studies.

Since the early 1990's, exact time-dependent quantum WP methods have been employed to explore the dynamics through conical intersections. Kuppermann *et. al.* performed systematic calculations for H_3 to explore the geometric phase effect [37–40]. Schinke's group performed many calculations of the photodissociation dynamics of small molecules (*e.g.* H_2S), which showed perfect agreement with the experimental observations [3]. Cederbaum, Domcke and Köppel developed the linear vibronic coupling model and explored a series of photoinduced reactions in polyatomic molecules [4, 41, 42].

Nowadays, WP calculations are standard methods which can be employed to understand the nonadiabatic dynamics at conical intersections. In these ap-

proaches, the propagation of a WP on coupled surfaces is obtained by solving the time-dependent Schrödinger equation. Because the computational effort increases dramatically with the number of degrees of freedom, these treatments require the construction of reduced-dimensional models for polyatomic systems. This is often a good approximation for ultrafast processes, because only a few active modes dominate the dynamics at short timescales. The large number of inactive modes are spectators and are weakly coupled with the active modes. The WP method is one of the most important ways to explore the dynamics at conical intersections, because a detailed analysis of exact WP dynamics in reduced dimensionality can provide mechanistic insight into the dynamics at conical intersections. In particular, the WP method fully accounts for quantum effects, such as hydrogen-tunnelling and the geometric phase, which are difficult to describe with classical trajectory methods.

An alternative approach to treat the multidimensional quantum dynamics through conical intersections is to apply the multi-configuration time-dependent Hartree (MCTDH) method, proposed by Meyer, Manthe and Cederbaum [43–45]. Developed by a few groups [4, 45–49], this method is the only one at present, which can treat the multi-mode quantum dynamics of polyatomic systems with controllable accuracy. Using MCTDH, the photoinduced dynamics of pyrazine with all of its 24 degrees of freedom has been studied [46,47]. A powerful extension of MCTDH is the so-called multi-layer MCTDH, recently developed by Wang and Thoss [50,51]. It has been shown that this new method provides a promising way to treat the quantum dynamics of systems with hundreds or more degrees of freedom.

As an alternative to quantum dynamical methods, many attempts have been made to treat the dynamics through conical intersections with classical, mixed quantum-classical, or semiclassical approaches. Because these theories are beyond the scope of this thesis, only the main ideas are summarized here. A typical approach is to treat the electronic motions with quantum mechanics and the nuclear motions with classical mechanics. For the model of pyrazine, Stock and Thoss used mean-field theory to treat the nuclear dynamics driven by the mean-field

potential formed by averaging electronic motions [3, 52]. They also showed that it is possible to calculate the classical trajectories of nuclear motions on a single surface and treat nonadiabatic transitions using the surface hopping method [53]. For large systems, so-called "on-the-fly"methods have been developed by several groups, *e.g.* Lischka [32,54–57], Bonačić-Koutecký [57,58], and Martinez [59–61]. Here, the nuclear motions are described by classical trajectories. The gradients of the potential energies are computed at the different points along classical trajectories and these provide the driving forces for the nuclear motions. Most on-the-fly calculations are performed in the adiabatic representation. It is thus necessary to evaluate the nonadiabatic couplings between different surfaces. Nowadays, the progress of analytical ways to evaluate these couplings has improved the speed of the calculations. Since the gradients are evaluated along the trajectories, rather than over the whole PE surfaces, the on-the-fly methods are much more efficient than WP methods for large systems if the number of trajectories is small. Therefore these methods are only ones which can include all nuclear degrees of freedom in the exploration of the nonadiabatic dynamics at conical intersections in polyatomic molecules. However, as these methods are based on classical mechanics, they can not account for more subtle effects, such as coherence and the geometric phase. Martinez has developed the *ab initio* multiple spawning (AIMS) method [59–61], which relies on classical mechanics, while allowing quantum mechanical effects to be included in the nuclear dynamics.

Although WPs can be transferred to the electronic ground state through conical intersections, the large excess energies of these WPs represent "hot"molecules, inducing highly excited vibrational states are populated on the ground surface. Internal conversion can take place only if the excess energy can be dissipated. For polyatomic molecules or solute molecules surrounded by solvent molecules, the active modes (tuning and coupling modes) of conical intersections will be coupled with many other degrees of freedom. This coupling will induce energy transfer from the active modes to a large number of other vibrational modes. This vibrational energy flow will result in the vibrational cooling of the active modes and will thus enhance the probability of internal conversion. Thus, for a com-

plete theoretical description of the internal-conversion dynamics, intramolecular vibrational relaxation and solvent effect must be included.

In the last ten years, a few theoretical approaches have been developed to take dissipative environments into account in the calculations of the internal-conversion dynamics at conical intersections. Among them, the reduced-density-matrix formalism based on the system-bath model has become the most popular method [4,42,62–64]. In this approach, a system and a bath are defined to include the active modes and the inactive modes, respectively. The system-bath coupling describes the interactions between active and inactive modes. In the weak coupling case, the equation of motion for the reduced density matrix of the system part can be constructed explicitly using perturbation theory. This treatment has revealed interesting behaviour of the WP motion through conical intersections under the influence of a dissipative environment, such as decoherence, vibrational damping and vibrational cooling. Alternative treatments of this problem are based on path integral [65–67] or Monto-Carlo-wavefunction methods [68,69].

These theoretical efforts to understand conical intersections have not only identified the most important conical intersections in different classes of photoinduced reactions, but also have revealed the details of the photoinduced dynamics at conical intersections. Nowadays, it is widely recognized that conical intersections play a crucial role in many photoinduced chemical reactions. The research on conical intersections has covered many important parts of photochemistry, such as the understanding of many important elementary reactions, the explanation of ultrafast phenomena, the control of chemical reactions, the exploration of photosynthesis and the investigation of the effects of solar light on the evolution of live.

1.2 Photochemistry of aromatic biomolecules

The aromatic amino acids and the nucleic acid bases represent some of the most important building blocks of life. Therefore, their photoinduced reactions are of great interest both from the experimental and theoretical points of view. A characteristic feature of the photochemistry of these molecules in the condensed

phase is the low quantum yield of fluorescence after Ultraviolet (UV) absorption [2, 70–72]. This indicates the existence of nonradiative processes which quench the fluorescence with particular efficiency. As far as we know, these nonradiative processes involve ultrafast internal conversion to the electronic ground state. These processes dissipate the photon energy before more profound chemical reactions can happen. This so-called "photostability" of the building blocks protects living matter from dangerous photoreactions [70–73]. It is conceivable that photostability has been a major criterion in the evolutionary selection of the building blocks of life.

In recent years, the investigation of isolated biomolecules and their clusters has provided a significant amount of new and precise information on the photophysics and photochemistry of these these systems. Among them, three molecules, pyrrole [74–95], phenol (the chromophore of tyrosine) [83, 95–121] and indole [71, 83, 99, 122–128], as well as their derivatives and clusters, have emerged as interesting prototype molecules for the exploration of ultrafast excited-state dynamics. These molecules strongly absorb in UV *via* excitation to their $^1\pi\pi^*$ states. Previous studies have tried to identify the different radiationless decay channels, which may involve dark states ($^1\pi\sigma^*$ or $^1n\pi^*$). These dark states couple with the optically bright $^1\pi\pi$ states, as well as the ground state, to induce the nonadiabatic transitions and deplete the population in the $^1\pi\pi$ states. In addition, radiationless transitions also take place between the $^1\pi\pi$ and S_0 states directly *via* their vibronic couplings.

One of the dominant decay channels of these molecules has been pointed out by Sobolewski *et. al.* [83], namely hydrogen-detachment in the isolated systems and chromophore-to-solvent hydrogen transfer in their clusters. The mechanism in these representative systems seems to be universal to all aromatic molecules containing hydroxy (OH) or azine (NH) groups.

The UV photochemistry of isolated pyrrole, phenol and indole involves the electronic states S_0, $^1\pi\pi^*$ and $^1\pi\sigma^*$, see Fig. 1 [83]. At a first glance, the PE surfaces of these systems share similar features. The $^1\pi\pi^*$ states, corresponding to valence excitations from π to π^* orbitals, are the UV absorbing states and

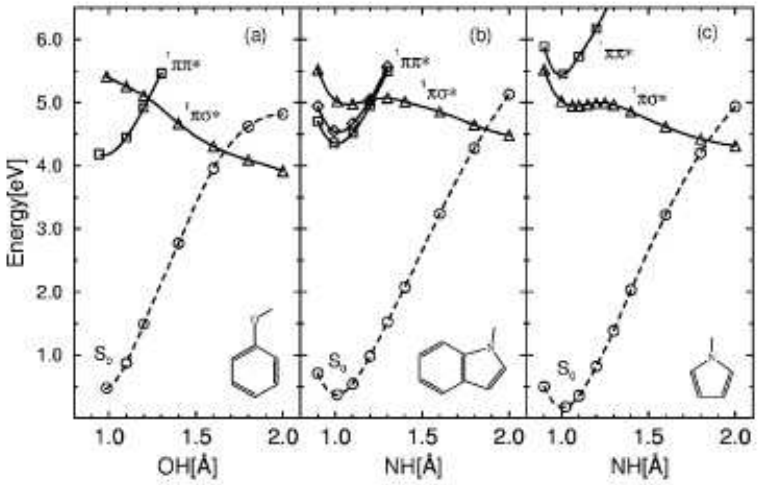

Figure 1.1: PE profiles of the lowest $^1\pi\pi^*$ states (squares and diamonds), the lowest $^1\pi\sigma^*$ state (triangles) and the electronic ground state (circle) as a function of the OH stretch (phenol) or NH stretch (indole, pyrrole) reaction coordinate. Geometries have been optimized in the $\pi\sigma^*$ excited electronic state at the CASSCF level; the PE profiles have been obtained with the CASPT2 method [83].

are responsible for the intense bands in the absorption spectra. The $^1\pi\sigma^*$ states correspond to excitations from the valence π orbitals of the ring to the Rydberg-like $3s$ orbital. These states cannot be observed spectroscopically, because these electronic transitions possess very small oscillator strengths [81]. The $3s$ Rydberg orbital has a significant anti-bonding character with respect to the NH or OH bond (σ^* character), see Fig. 1.2 [83]. The change of character of the $^1\pi\sigma^*$ electronic wavefunction is reflected by large variations of the dipole moment (DM) along the OH or NH stretching coordinates. The large DM indicates that these $^1\pi\sigma^*$ states exhibit considerable charge-transfer character. Upon stretching of the NH or OH bond, the $^1\pi\sigma^*$ PE functions intersect the potential functions of the $^1\pi\pi^*$ states, resulting in conical intersections along the reaction path. Due to the existence of conical intersections between the bright $^1\pi\pi^*$ states and the dark $^1\pi\sigma^*$ states, the population of the bright state can be transferred to the dark state through internal conversion after excitation. The repulsive $^1\pi\sigma^*$ PE function also crosses the PE function of the ground state, providing a mechanism

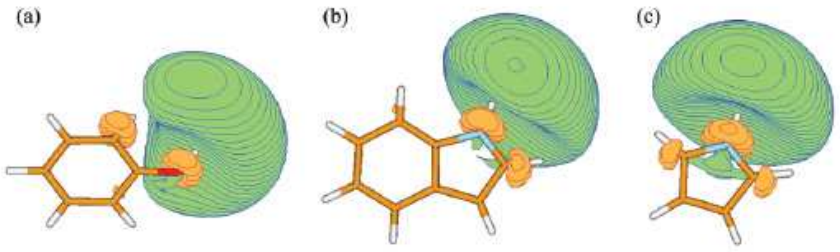

Figure 1.2: The σ^* natural orbital obtained by a CASSCF calculation for the $\pi\sigma^*$ state of (a) phenol, (b) indole and (c) pyrrole at the ground-state equilibrium geometry [83].

for ultrafast internal conversion to the electronic ground state, as well as hydrogen abstraction. This mechanism can explain many experimental observations and the different photoinduced dynamics of these systems can be understood in terms of the relative location of the $^1\pi\pi^*$, $^1\pi\sigma^*$ and S_0 states [83].

For pyrrole, there are two $\pi\sigma^*$ states ($^1A_2$ and $^1B_1$) and two $\pi\pi^*$ ($^1B_1$ and $^1A_1$) in the energy region around 6 eV. Although the ordering of the vertical excitation energies of these four states has been quite controversial [80–82], there is agreement that the two $^1\pi\pi^*$ states are responsible for the broad and intense absorption band near 6 eV [74–76]. The lowest $\pi\sigma^*$ ($^1A_2$) surface is below the two $^1\pi\pi^*$ surfaces, while the excitation energy of the other $\pi\sigma^*$ ($^1B_1$) state is similar to those of the $^1\pi\pi^*$ states. Because the $^1\pi\pi^*$–$^1\pi\sigma^*$ conical intersections are close to the Frank-Condon (FC) region, the populations of the bright $^1\pi\pi^*$ states are expected to decay to the dark $^1\pi\sigma^*$ states very quickly. This has recently been confirmed by Köppel *et. al.* [86] for pyrrole and related five-membered heterocycles. This ultrafast transition explains the complete absence of fluorescence in pyrrole. Afterwards, the dynamics is governed by the repulsive $^1\pi\sigma^*$ PE surface and its conical intersection with the ground state surface. This $^1\pi\sigma^*$–S_0 conical intersection may cause the internal conversion to the ground state, or may lead to H-atom detachment. The latter process has been confirmed by the experimental detection of fast hydrogen atoms in the photodissociation of pyrrole [77,87,88,90].

When the $^1\pi\pi^*$ surface is lower than the $^1\pi\sigma^*$ surface in the FC region, like in phenol, a $^1\pi\pi^*$–$^1\pi\sigma^*$ curve crossing occurs at intermediate OH distances. The

photoinduced dynamics is strongly dependent on the excess energy available in the $^1\pi\pi^*$ state. If the initial energy is below the $^1\pi\pi^*$–$^1\pi\sigma^*$ crossing seam, the system will be trapped in the well of the $^1\pi\pi^*$ surface, resulting in a sharp absorption spectra and a high quantum yield of fluorescence. This qualitatively explains the fluorescence lifetimes of the lowest vibronic levels of the S_1 states of phenol and deuterated phenol, which are 2 ns and 12 ns [97, 129, 130], respectively. Photoexcitation of system above the $^1\pi\pi^*$–$^1\pi\sigma^*$ crossing, on the other hand, leads to a diffuse absorption spectrum and a complete quenching of the fluorescence. Since a rather small energy difference is expected between the $^1\pi\pi^*$–$^1\pi\sigma^*$ crossing seam and the minimum of the $^1\pi\pi^*$ surface in phenol, the excitation of the ν=1 level of the OH stretching motion in the $^1\pi\pi^*$ state should induce an ultrafast population transfer between the $^1\pi\pi^*$ and $^1\pi\sigma^*$ states. This can explain the absence of the fundamental OH stretching vibration in excited-state infrared (IR) spectra [108, 131]. After the $^1\pi\pi^*$–$^1\pi\sigma^*$ population transfer, the dynamics is governed by the repulsive $\pi\sigma^*$ PE surface, resulting in the ultrafast hydrogen detachment, which has experimentally been verified [104, 120].

It is a typical phenomenon of the ultrafast radiationless decay dynamics *via* conical intersections in these aromatic systems that their photoinduced products, the corresponding radicals, are formed in a remarkably limited subset of their available state density. The state-selective product formation after photoexcitation of medium-size organic molecules has been observed by Ashfold and collaborators, using high-resolution photofragment translational spectroscopy at several excitation wavelengths, for pyrrole, phenol and several other heteroaromatic molecules [91, 94, 95, 120, 132]. Such vibrational mode-specific dynamics is now recognized as a signature of this type of photoinduced reactions [95].

This $\pi\sigma^*$ mechanism can also explain the photochemistry of the phenol-water and phenol-ammonia clusters. Fig. 1.3 shows the PE functions along the minimum-energy reaction path for hydrogen transfer in phenol-H_2O and phenol-NH_3 as two typical examples [83, 116]. The energies of the S_0 states of these clusters are lowered for large OH distances, compared with free phenol, due to the stabilization of the ion-pair configuration $Ph^-(H_3O)^+$ or $Ph^-(N_4H)^+$.

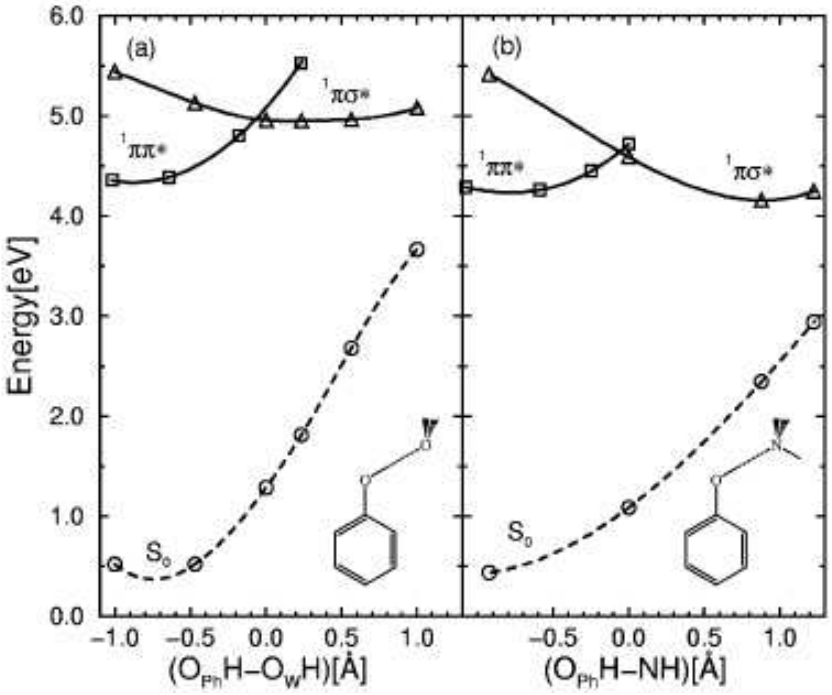

Figure 1.3: PE profiles of the lowest $^1\pi\pi^*$ state (squares), the lowest $\pi\sigma^*$ state (triangles) and the electronic ground state (circles) as a function of the hydrogen-transfer coordinate for the phenol-water (a) and phenol-ammonia (b) cluster. Geometries have been optimized in the $\pi\sigma^*$ excited electronic state at the CASSCF level; the PE profiles have been obtained with the CASPT2 method [83].

On the other hand, the $\pi\sigma^*$ state shifts to higher energies for larger OH distances, resulting in a minimum of this surface. This minimum denotes the biradical configurations $Ph^\bullet(H_3O)^\bullet$ or $Ph^\bullet(N_4H)^\bullet$. Thus, a hydrogen atom, rather than a bare proton, is transferred from phenol to solvent molecules in the $\pi\sigma^*$ state. This hydrogen transfer process has been observed in phenol-ammonia clusters [83, 101–103, 116–118]. The excited-state hydrogen-transfer reaction is a concerted electron- and proton-transfer process, which replaces the traditional picture of an excited-state proton transfer in these systems. Similar to bare phenol, the reaction rate of hydrogen transfer is highly enhanced by the excitation of the OH stretching mode [108, 109, 131].

Although quite limited theoretical calculations have been performed for the

excited states of DNA bases up to now [73,83,133–151], it has been shown that the PE profiles for hydrogen detachment in 9H-adenine are quite similar to indole and phenol [83, 143, 144, 146, 147], see Fig. 1.4. Thus, the same hydrogen-detachment

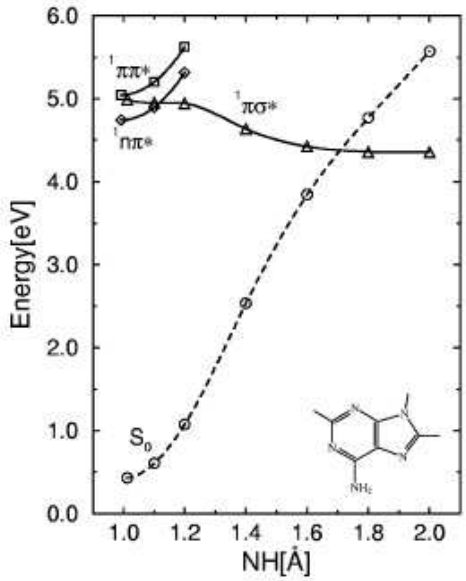

Figure 1.4: PE profiles of the lowest $^1\pi\pi^*$ state (squares), the lowest $^1n\pi^*$ state (diamonds), the lowest $^1\pi\sigma^*$ state (triangles) and the electronic ground state (circles) of 9H-adenine, as a function of the NH stretching coordinate (see Ref. [83] for details).

dynamics driven by the $\pi\sigma^*$ state should be expected. However, it is not the dominant channel at low excitation energies due to the comparatively high energy of the $^1\pi\pi^*$–$^1\pi\sigma^*$ conical intersection. The *ab initio* calculations have identified the existence of other conical intersections, including $^1\pi\pi^*$–$^1n\pi^*$, $^1\pi\pi^*$–S_0 and $^1n\pi^*$–S_0. Considering the energies of these conical intersections, the widely accepted decay mechanism of electronically excited adenine molecules involves the successive $^1\pi\pi^* \rightarrow ^1 n\pi^* \rightarrow S_0$ radiationless transitions [72, 138, 152–162]. On the other hand, the channel of hydrogen detachment through the $^1\pi\sigma^*$ state will open upon shortening the wavelength of exciting laser [157,161]. In addition, the probability of the dominant decay channel is reduced in the adenine dimer and vanishes in adenine-water clusters due to the competition with the relaxation path through the $^1\pi\sigma^*$ state [163].

The PE surfaces of the adenine-thymine (AT) and guanine-cytosine (GC) base pairs, as functions of the appropriate hydrogen-transfer coordinate, share similar features, except that the lowest charge-transfer state is a dark $^1\pi\pi^*$ state rather than a $\pi\sigma^*$ state [72, 73, 164–168]. This dark state connects the optically bright excited state, and the electronic ground state *via* two conical intersections along the hydrogen-transfer coordinate, see Fig. 1.5. For the Watson-Crick conformer

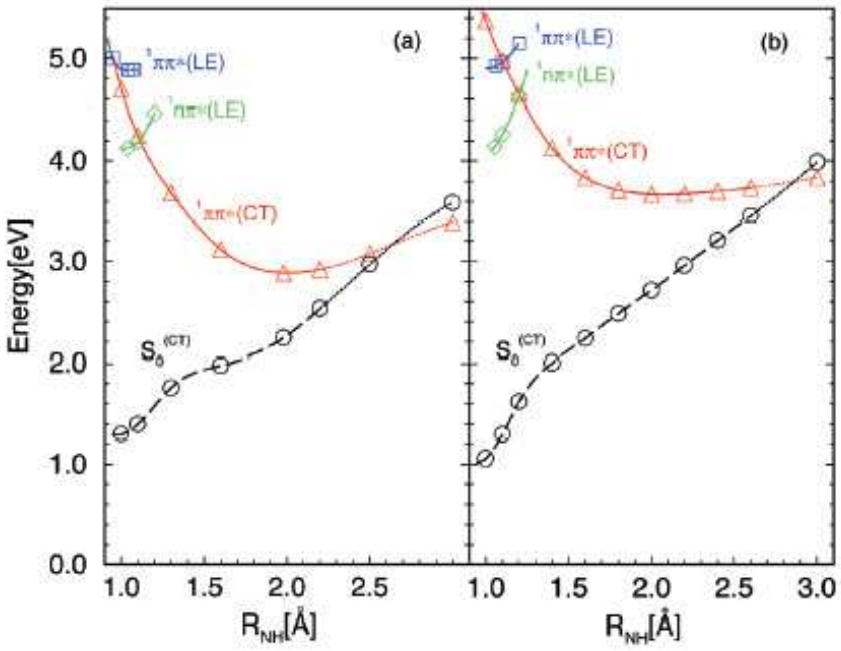

Figure 1.5: PE profiles of the electronic ground state (circles), the lowest locally-excited state [$^1\pi\pi^*$ (squares) and $^1n\pi^*$(diamonds)], the lowest $^1\pi\pi^*$ charge-transfer state (triangles) of the GC (a) and AT (b) base pair, as a function of the hydrogen-transfer coordinate (see Ref. [73] for details).

of the GC pair, the barrierless access to the reactive charge-transfer state after photoexcitation provides a pathway for fast return to the electronic ground state. This mechanism can explain the weak and broad multi-photon ionization spectrum of the Watson-Crick conformer of GC pair [72, 73] as well as the short lifetime of the bright excited state [72, 73], in contrast to the other conformers of the GC pair [73, 167]. This indicates that the unique features of the PE profiles

along the hydrogen-transfer coordinate play a key role in the photochemistry of the biologically relevant Watson-Crick conformer, which efficiently enhances the population decay of the electronic excited state and maximizes the photostability. Thus, it is reasonable to assume that the Watson-Crick structure of the GC pair has been selected on account of its unique photophysicl properties in the biological evolution. Although the UV spectrum of the Watson-Crick conformer of the AT pair has not yet been observed, the similar PE profiles, obtained from *ab initio* calculations [73, 168], indicate that the same ultrafast decay of the excited state takes place and that the Watson-Crick conformer of the AT pair also maximizes the photostability.

1.3 Our goal and outline of my thesis

In recent theoretical investigations of radiationless decay mechanism of aromatic biomolecules, conical intersections of the PE surfaces along reaction paths have been identified, but no calculations of the photoinduced dynamics through conical intersections has been reported. Time-dependent quantum WP calculations for the nuclear dynamics at conical intersections are the topic of the present work. We select pyrrole and phenol as two prototype systems, for the exploration of the photoinduced hydrogen-elimination and internal-conversion dynamics *via* $^1\pi\sigma^*$ states. Multi-reference electronic-structure methods have been employed to identify the photochemically relevant nuclear degrees of freedom at conical intersections and characterize the PE surfaces of the electronic states. The essential features of ultrafast internal-conversion and photodissociation dynamics at conical intersections are systematically explored, using standard methods of time-dependent quantum WP propagations and density-matrix formalisms.

Different topics are covered here, including well-established theories, the development of new methods, as well as calculations for specific molecular systems (pyrrole and phenol). The theoretical part includes electronic-structure theory, WP dynamics, and quantum dissipative dynamics. This theoretical background is discussed in Chapters 2 - 5. The efforts to understand the ultrafast internal-conversion and photodissociation dynamics of pyrrole and phenol are discussed

Table 1.1: Notations used in this thesis.

$\hat{A}$	Operator
$\mathbf{A}$	Matrix
A	Scale
A_{mn}	Matrix element

in Chapters 6 - 8. Throughout the whole thesis, atomic units are used to simplify the calculations. In the equations, I have adopted the conventions defined in Table. 1.1.

Chapter 2 gives a systematic introduction of the theory of conical intersections. The basic ideas of the BO approximation are discussed. The non-BO theory is introduced to describe the coupled motions of electrons and nuclei. A few important technical aspects, such as the adiabatic-to-diabatic transformation, symmetry selection rules , topography of conical intersections and the geometric phase are discussed. The effective mode formalism is introduced to simplify the treatment of multi-mode dynamics at conical intersections.

Chapter 3 outlines the basic ideas of the *ab initio* methods used in the present thesis, such as the Hartree-Fock (HF), multi-configuration self-consistent field (MCSCF), complete-active-space self-consistent-field (CASSCF) and multi-reference configuration interaction (MRCI) methods.

Chapter 4 introduces the time-dependent WP dynamics. The construction of the kinetic-energy operator is the first topic of this chapter. Then, the ways to solve the time-independent and time-dependent Schrödinger equations are described. A few important methods, such as the Discrete Variable Representation (DVR) and Fourier-transformation methods, are discussed. Some useful techniques for the WP calculations of nonadiabatic systems are explained.

Chapter 5 deals with quantum dissipative dynamics. I have used the reduced density-matrix approach based on the system-plus-bath model. The Born-Markov approximation is applied to obtain the Redfield equation, which completely describes the system dynamics in the presence of coupling to a bath. A new method for the solution of the Redfield equation is proposed and applied for the explo-

ration of the quantum dissipative dynamics at conical intersections.

In Chapter 6, the photoinduced nonadiabatic dynamics of pyrrole *via* the $^1B_1(\pi\sigma^*)$ and $^1A_2(\pi\sigma^*)$ states is investigated [89, 93]. The two $^1\pi\sigma^*$–S_0 conical intersections are treated separately. Electronic-structure calculations have been employed to characterize the coupling modes. In a first approximation, we consider two dimensional (2D) models including the NH stretching mode as well as the dominant coupling mode at the $^1A_2(\pi\sigma^*)$–S_0 and $^1B_1(\pi\sigma^*)$–S_0 conical intersections, respectively. The diabtic PE surfaces have been constructed from *ab initio* data. The electronic population transfer at the conical intersections, the branching ratio between different dissociation channels, and their dependence on the initial preparation of the system have been investigated. The influence of the mode-specific vibration excitation on the nonadiabatic dynamics is discussed. The WP motion is shown to display the details of the dissociation and internal-conversion dynamics. To understand the effect of all symmetry-allowed coupling modes [41], the 2D models have been extended to explore the multimode dynamics for both $^1\pi\sigma^*$–S_0 conical intersections. The comparison between the three-mode and two-mode model calculations displays the influence of the inclusion of weak coupling modes on the photoinduced dynamics of pyrrole.

Chapter 7 explores the photoinduced dynamics of phenol. Here, a model including three intersecting electronic potential-energy surfaces (S_0, $^1\pi\sigma^*$, $^1\pi\pi^*$) has been constructed on the basis of accurate *ab initio* multi-reference electronic-structure data. Similar to pyrrole, the nonadiabatic population transfer dynamics and the branching ratio of the dissociation are calculated by photoexciting phenol from different vibrational levels of its electronic ground state. The effect of the geometric phase on the WP motion is analyzed to understand the interplay between these two conical intersections.

Chapter 8 deals with the quantum dissipative dynamics of pyrrole *via* the lowest $^1\pi\sigma^*$ state using density-matrix formalism. In the system-plus-bath model, the system part involves the NH stretching and dominant coupling mode; the harmonic-oscillator bath is assumed to mimic the photoinactive modes. The dissipative dynamics is explored by the numerical propagation of the reduced

density operator. The influence of the system-bath coupling on the internal-conversion probability has been investigated. The nuclear probability densities are displayed to understand the cooling of the vibrational motion of the NH stretching mode by the environment.

Chapter 9 summaries the theoretical efforts, in my Ph.D work (Sept. 2003 - Feb. 2007), towards the understanding of the photoinduced dynamics of aromatic biomolecules and proposes interesting research topics for the future.

Chapter 2

Theory of conical intersections

2.1 Noncrossing rule

To begin the discussion of conical intersections, we should first investigate the possibility of the existence of a crossing between two electronic states. Following the original idea of von Neumann and Wigner [9], let us consider Teller's [10] analysis to give the necessary condition for the case of a surface crossing.

If we neglect the spin terms in the electronic Hamiltonian, the electronic wavefunctions can be taken to be real. Suppose a case that we already know the electronic wavefunctions of all energy levels except for the last two states that cross each other. Under this condition, we can select two arbitrary wave functions, ϕ_1 and ϕ_2, which are orthogonal to each other and to the other known electronic functions. Then it is possible to express each of two electronic wave functions in the form:

$$\psi = c_1\phi_1 + c_2\phi_2, \tag{2.1}$$

and the electronic Schrödinger equations becomes:

$$\begin{bmatrix} H_{11} - E & H_{12} \\ H_{21} & H_{22} - E \end{bmatrix} \begin{bmatrix} c_1 \\ c_2 \end{bmatrix} = 0, \tag{2.2}$$

all quantities in this equation being real.

For degenerate solutions to exist for Eq. 2.2, it is necessary to satisfy two

independent conditions, namely

$$H_{11} = H_{22}, \tag{2.3}$$

$$H_{12} = H_{21} = 0. \tag{2.4}$$

This requires the existence of at least two independent variables. In a diatomic molecule, there is only one variable coordinate, the interatomic distance. Thus the degeneracy cannot occur in general. This is the so-called non-crossing rule. In a molecular system with three or more atoms, on the other hand, there are enough independent degrees of freedoms which can be varied to satisfy Eqs. 2.3 and 2.4. Therefore, we should expect that degeneracies, or surface crossings, are quite typical for polyatomic systems.

Following Teller [10], Herzberg and Longuet-Higgins [14], we denote two independent internal nuclear coordinates by x and y, and take the origin at the point where Eqs. 2.3 and 2.4 are satisfied. Next, a first order Taylor expansion of the matrix elements of the Hamiltonian leads to

$$\begin{bmatrix} W + h_1 x - E & ly \\ ly & W + h_2 x - E \end{bmatrix} \begin{bmatrix} c_1 \\ c_2 \end{bmatrix} = 0. \tag{2.5}$$

If we assume $m = \frac{1}{2}(h_1 + h_2)$ and $k = \frac{1}{2}(h_1 - h_2)$, the eigenvalues are

$$E = W + mx \pm \sqrt{k^2 x^2 + l^2 y^2}. \tag{2.6}$$

This indicates that the PE surfaces form a double cone with the vertex at the origin. Therefore, this type of surface crossing is called "conical intersection".

2.2 BO approximation and beyond

Since molecules are quite complicated quantum objects, it is difficult to treat the electronic and nuclear motions simultaneously, even for small molecular systems. However, the large masses of the nuclei, compared to that of an electron, permit a separation of the electronic and nuclear motions in the treatment of molecular systems. This leads to the well-known Born-Oppenheimer (BO) approximation [5]. The BO approximation is very accurate for the electronic ground states of most

molecular systems, because the ground state is usually well separated from other electronic states. For the electronic excited electronic states, the BO approximation fails in many situations, because the electronic excited states are often quite close in energy. In particular, the BO approximation breaks down for degenerate states, for example at conical intersections, also called "photochemical funnels" [20], which play a central role in many photo-induced reactions and the internal-conversion dynamics of molecules. Therefore, it is necessary to go beyond the BO approximation when treating the dynamics at conical intersections.

The starting point of molecular quantum mechanics is the Schrödinger equation:

$$\hat{H}\Psi(\mathbf{r_e}, \mathbf{R_n}) = E\Psi(\mathbf{r_e}, \mathbf{R_n}), \tag{2.7}$$

where $\Psi(\mathbf{r_e}, \mathbf{R_n})$ is the total wavefunction for the molecular system and the vectors $\mathbf{r_e}$ and $\mathbf{R_n}$ correspond to the coordinates for electrons and nuclei, respectively. The Hamiltonian is written as follows:

$$\hat{H} = \hat{T}_n + \hat{T}_e + \hat{V}(\mathbf{r_e}, \mathbf{R_n}), \tag{2.8}$$

where $\hat{T}_n$ and $\hat{T}_e$ are the kinetic-energy operators of nuclei and electrons, respectively. $\hat{V}(\mathbf{r_e}, \mathbf{R_n})$ is the total potential energy of the molecular system, including the nuclei-nuclei, nuclei-electron and electron-electron Coulomb interactions.

For a particular geometry of the molecule, we can define the electronic Hamiltonian as:

$$\hat{H}_e(\mathbf{R_n}) = \hat{T}_e + \hat{V}(\mathbf{r_e}, \mathbf{R_n}). \tag{2.9}$$

Here $\hat{H}_e$ is an operator in the electronic space which depends on the nuclear geometry, which is characterized by the coordinate $\mathbf{R_n}$.

2.2.1 BO approximation

The masses of nuclei are much greater (at least 1836 times heavier) than the mass of the electron. This means that the electrons can adjust their motion almost instantaneously to any change in the positions of the nuclei. It is therefore reasonable to assume that the electronic wavefunction depends only on the positions

of nuclei, and not on their momenta. Thus, the total wavefunction $\Psi(\mathbf{r_e}, \mathbf{R_n})$ for a molecule can be written as:

$$\Psi(\mathbf{r_e}, \mathbf{R_n}) = \Phi(\mathbf{r_e}, \mathbf{R_n})\chi(\mathbf{R_n}), \tag{2.10}$$

where $\Phi(\mathbf{r_e}, \mathbf{R_n})$ and $\chi(\mathbf{R_n})$ are the electronic and nuclear wavefunctions, respectively. Note that the electronic wavefunction $\Phi(\mathbf{r_e}, \mathbf{R_n})$ are parametrically dependent on the nuclear geometry $\mathbf{R_n}$. Insertion of Eq. 2.10 into Eq. 2.7 leads to the decoupled equations:

$$\hat{H}_e(\mathbf{R_n})\Phi(\mathbf{r_e}, \mathbf{R_n}) = V(\mathbf{R_n})\Phi(\mathbf{r_e}, \mathbf{R_n}), \tag{2.11}$$

$$\left[\hat{T}_n + V(\mathbf{R_n})\right] \chi(\mathbf{R_n}) = E\chi(\mathbf{R_n}), \tag{2.12}$$

which represent the BO approximation. These expressions indicate that the electronic motion for fixed nuclear geometry determines an effective potential $V(\mathbf{R_n})$, which governs the motion of the nuclei. Since this effective potential is a function of $\mathbf{R_n}$, we call it a "potential energy (PE) surface". In the BO approximation, the nuclei move on an single PE surface.

In molecular excited-state dynamics, the nuclei many "jump" from one PE surface to another. These so-called "nonadiabatic transitions" are induced by the strong couplings between the motions of electrons and nuclei, especially at conical intersections. We therefore have to go beyond the BO approximation to set up the theoretical framework for photoinduced dynamics.

2.2.2 Born-Oppenheimer-Huang expansion

Since $\hat{H}_e$ is an operator in electronic space, its eigenfunctions $\Phi_i^a(\mathbf{r_e}, \mathbf{R_n})$ form a set of complete orthogonal basis functions for every $\mathbf{R_n}$:

$$\hat{H}_e(\mathbf{R_n})\Phi_i^a(\mathbf{r_e}, \mathbf{R_n}) = V_i^a(\mathbf{R_n})\Phi_i^a(\mathbf{r_e}, \mathbf{R_n}), \tag{2.13}$$

$$\int d\mathbf{r_e}\Phi_i^{a*}(\mathbf{r_e}, \mathbf{R_n})\Phi_j^a(\mathbf{r_e}, \mathbf{R_n}) \equiv \langle i(\mathbf{R_n}) | \, j(\mathbf{R_n})\rangle = \delta_{ij}. \tag{2.14}$$

In this bra and ket notation, the scalar product involves the integral over the electronic coordinates at a fixed nuclear geometry $\mathbf{R_n}$.

In this basis set, the total wavefunction can be expressed as:

$$\Psi(\mathbf{r_e}, \mathbf{R_n}) = \sum_i \Phi_i^a(\mathbf{r_e}, \mathbf{R_n})\chi_i^a(\mathbf{R_n}). \tag{2.15}$$

This expansion is also called the Born-Oppenheimer-Huang expansion [169]. It leads to the following coupled equations for the nuclear motions:

$$\sum_j \langle i(\mathbf{R_n})| \hat{T}_n \chi_j^a(\mathbf{R_n}) |j(\mathbf{R_n})\rangle + V_i^a(\mathbf{R_n})\chi_i^a(\mathbf{R_n}) = E\chi_i^a(\mathbf{R_n}). \tag{2.16}$$

The kinetic-energy operator $\hat{T}_n$ is defined as:

$$\hat{T}_n = -\frac{1}{2}\nabla^2, \tag{2.17}$$

where ∇ is the gradient operator in the space of mass-weighted nuclear coordinates. The Born-Oppenheimer-Huang coupled equations take the form:

$$\begin{aligned}&[-\frac{1}{2}\nabla^2 + V_i(\mathbf{R_n})]\chi_i^a(\mathbf{R_n}) - \frac{1}{2}\sum_j [2\vec{F}_{ij}^a(\mathbf{R_n}) \cdot \nabla + G_{ij}^a(\mathbf{R_n})]\chi_j^a(\mathbf{R_n}) \\ &= E\chi_i^a(\mathbf{R_n}),\end{aligned} \tag{2.18}$$

where $\vec{F}_{ij}^a(\mathbf{R_n})$ is the first-order nonadiabatic coupling vector

$$\vec{F}_{ij}^a(\mathbf{R_n}) = \langle i(\mathbf{R_n})| \nabla |j(\mathbf{R_n})\rangle . \tag{2.19}$$

The second-order nonadiabatic coupling $G_{ij}^a(\mathbf{R_n})$ is a scalar:

$$G_{ij}^a(\mathbf{R_n}) = \langle i(\mathbf{R_n})| \nabla^2 |j(\mathbf{R_n})\rangle . \tag{2.20}$$

Although the above theoretical framework is based on the time-independent picture and the mass-weighted Cartesian kinetic-energy operator, the whole procedure is also valid in the time-dependent picture and for more general kinetic-energy operators.

2.3 Adiabatic representation

It is known that any orthogonal complete set of basis functions can be used to expand the total wavefunction. In the preceding section, the basis functions are the eigenfunctions of the electronic Hamiltonian. This defines the "adiabatic" representation.

2.3.1 Adiabatic electronic states

At a single nuclear geometry, the solutions of the Schrödinger equation for the electronic motion define a complete set of adiabatic electronic states. The energies of these electronic states are functions of the nuclear geometry. This implies that electronic-structure calculations generate the adiabatic PE surfaces.

The motions of nuclear WP are driven by the adiabatic PE surfaces. But in violation of the BO approximation, the nuclei can "jump" between different adiabatic electronic states, which is called a nonadiabatic transition. This transition is induced by the derivative couplings $\vec{F}_{ij}^{a}(\mathbf{R_n})$ and $G_{ij}^{a}(\mathbf{R_n})$.

When the energies of two states cross each other, the adiabatic electronic wavefunctions will interchange their characters at the crossing point. This means that the adiabatic electronic wavefunctions are not smooth functions of the nuclear geometry at a conical intersection. This discontinuity is directly reflected in the abrupt change of electronic properties, such as DMs.

2.3.2 Derivative couplings

The derivative couplings are composed of the vector part $\vec{F}_{ij}^{a}$ and the scalar part G_{ij}^{a}. It has been demonstrated that the vector part $\vec{F}^{a}$ plays the dominant role in nonadiabatic transitions [4].

According to the Hellmann-Feynman theorem [170], one can write:

$$\vec{F}_{ij}^{a} = \frac{\langle i(\mathbf{R_n}) | \nabla \hat{H}_e(\mathbf{r_e}, \mathbf{R_n}) | j(\mathbf{R_n}) \rangle}{V_i^a(\mathbf{R_n}) - V_j^a(\mathbf{R_n})}. \tag{2.21}$$

This expression implies three different situations for nonadiabatic transitions:

1. If two states are well separated in energy, $\vec{F}_{ij}^{a}$ goes to zero and the BO approximation should be valid.

2. In the case of small values of $\vec{F}_{ij}^{a}$, the nonadiabatic dynamics can be explored by perturbation theory. The slow radiationless decay of excited electronic states belongs to this case [35, 171, 172].

3. When the energy gap between two adiabatic electronic states is very small, nonadiabatic coupling terms become large and induce pronounced nonadiabatic

transitions. At the conical intersection, in particular, the degeneracy causes $\vec{F}^a_{ij}$ go to infinity.

2.4 Diabatic representation

To avoid the singularity in the adiabatic representation, a so-called diabatic representation is often applied to explore the nonadiabatic dynamics at conical intersections.

2.4.1 Diabatic basis

If a general electronic basis set $\Phi^d_i(\mathbf{r_e}, \mathbf{R_n})$ is used to expand the total molecular wavefunction:

$$\Psi(\mathbf{r_e}, \mathbf{R_n}) = \sum_i \Phi^d_i(\mathbf{r_e}, \mathbf{R_n})\chi^d_i(\mathbf{R_n}), \tag{2.22}$$

the coupled equations become:

$$-\frac{1}{2}\nabla^2\chi^d_i(\mathbf{R_n}) + \sum_j V_{ij}(\mathbf{R_n})\chi^d_j(\mathbf{R_n}) - \frac{1}{2}\sum_j [2\vec{F}^d_{ij}(\mathbf{R_n})\cdot\nabla + G^d_{ij}(\mathbf{R_n})]\chi^d_j(\mathbf{R_n}) = E\chi^d_i(\mathbf{R_n}) \tag{2.23}$$

with

$$V_{ij}(\mathbf{R_n}) = \left\langle i^d(\mathbf{R_n})\right| \hat{H}_e \left|j^d(\mathbf{R_n})\right\rangle, \tag{2.24}$$

$$\vec{F}^d_{ij}(\mathbf{R_n}) = \left\langle i^d(\mathbf{R_n})\right| \nabla \left|j^d(\mathbf{R_n})\right\rangle, \tag{2.25}$$

$$G^d_{ij}(\mathbf{R_n}) = \left\langle i^d(\mathbf{R_n})\right| \nabla^2 \left|j^d(\mathbf{R_n})\right\rangle. \tag{2.26}$$

Since any complete orthogonal basis can be used to get the above expressions, we may select the so-called "diabatic basis" $\Phi^d_i(\mathbf{r_e}, \mathbf{R_n})$ by minimizing the derivative coupling term $\vec{F}^d_{ij}(\mathbf{R_n})$. In general, a strict diabatic basis, for which $\vec{F}^d_{ij}(\mathbf{R_n}) = 0$, does not exist and only an approximate diabatic basis can be obtained, see below.

In this representation, $\Phi^d_i(\mathbf{r_e}, \mathbf{R_n})$ should be smooth functions of the nuclear geometry and $G^a_{ij}(\mathbf{R_n})$ should be negligible. The Eq. 2.23 thus becomes:

$$-\frac{1}{2}\nabla^2\chi^d_i(\mathbf{R_n}) + \sum_j V_{ij}(\mathbf{R_n})\chi^d_j(\mathbf{R_n}) = E\chi^d_i(\mathbf{R_n}). \tag{2.27}$$

This means that the singular derivative coupling $\vec{F}_{ij}^{a}$ in the adiabatic representation is transformed to the non-singular potential coupling V_{ij} in the diabatic representation.

2.4.2 Adiabatic-to-diabatic transformation

The adiabatic-to-diabatic transformation is a unitary transformation between the two basis set:

$$\chi^{\mathbf{a}}(\mathbf{R_n}) = \mathbf{U}\chi^{\mathbf{d}}(\mathbf{R_n}), \tag{2.28}$$

$$\mathbf{\Phi^a}(\mathbf{r_e}, \mathbf{R_n}) = \mathbf{\Phi^d}(\mathbf{r_e}, \mathbf{R_n})\mathbf{U}^{+}, \tag{2.29}$$

where $\mathbf{U}$ is a unitary matrix and $\chi^{\mathbf{a}}$ ($\chi^{\mathbf{d}}$) is the column vector of nuclear amplitudes for the adiabatic (diabatic) basis.

Some algebra leads to the following relation

$$\nabla\mathbf{U} + \mathbf{F^a U} = 0. \tag{2.30}$$

The necessary condition to solve this equation is the so-called "curl condition" [170, 173, 174]:

$$\nabla \times \mathbf{F^a} - \mathbf{F^a} \times \mathbf{F^a} = 0. \tag{2.31}$$

When this condition is satisfied, it is possible to construct a strictly diabatic basis. However, the curl condition cannot be satisfied in general [170, 173, 174]. In this case, we can only define an approximate diabatic basis by performing a "quasidiabatization" *via* the minimization of derivative couplings [170, 173].

It has been shown that diatomic systems always satisfy the curl condition [174]. For polyatomic systems, the situation is more complicated. If the adiabatic-to-diabatic transformation includes all electronic states, the curl condition is satisfied. In other words, the strictly diabatic basis only exists for a complete electronic Hilbert space [174]. In practice, it is impossible to include all electronic states. Therefore, only approximate diabatic basis can be defined in suitable subspaces including the relevant electronic states. The general way to deal with this problem is to separate the whole Hilbert space into two subspaces, P and Q [170].

The primary P space includes a few electronic states which are involved in the reaction dynamics. The complementary Q part contains all other electronic states. The diabatization is performed in the P space. As expected, the nonadiabatic couplings between different electronic states within the P space can be removed by the adiabatic-to-diabatic transformation, which are called the "removable couplings" or "longitudinal parts" [174]. In contrast, the couplings between the P and Q parts can not be eliminated by this diabatization, which are called the "nonremovable couplings"or " transverse parts" [174].

2.4.3 Conical intersections of two electronic states

After the introduction of the general adiabatic-to-diabatic transformation, we will demonstrate its application in a typical example, *i.e.* the two-state conical intersection.

According to the discussion in the preceding subsection, the P space includes two relevant electronic states which form a conical intersection. In the vicinity of a conical intersection, the nonadiabatic coupling goes to infinity. This means that the interaction within the P space is much larger than the coupling between the P and Q subspaces. Therefore, the latter can be neglected to a good approximation.

The adiabatic-to-diabatic transformation matrix in this two-dimensional space is determined by the mixing angle θ:

$$\mathbf{U}(\mathbf{R_n}) = \begin{pmatrix} \cos\theta(\mathbf{R_n}) & \sin\theta(\mathbf{R_n}) \\ -\sin\theta(\mathbf{R_n}) & \cos\theta(\mathbf{R_n}), \end{pmatrix}. \tag{2.32}$$

The relation Eq. 2.30 becomes:

$$\nabla\theta(\mathbf{R_n}) = \vec{F}^a_{12}, \tag{2.33}$$

and the curl condition becomes:

$$\nabla \times \vec{F}^a_{12} = 0. \tag{2.34}$$

The electronic potential energies in the two different representations are related as

$$\mathbf{V^d}(\mathbf{R_n}) \;=\; \mathbf{U}^+(\mathbf{R_n})\mathbf{V^a}(\mathbf{R_n})\mathbf{U}(\mathbf{R_n}), \tag{2.35}$$

where

$$\mathbf{V^d} = \begin{pmatrix} V_{11}^d & V_{12}^d \\ V_{21}^d & V_{22}^d \end{pmatrix}, \tag{2.36}$$

$$\mathbf{V^a} = \begin{pmatrix} V_1^a & 0 \\ 0 & V_2^a \end{pmatrix}. \tag{2.37}$$

Thus, the matrix $\mathbf{U}(\mathbf{R_n})$ is the eigenvector matrix of the diabatic potential matrix $\mathbf{V^d}(\mathbf{R_n})$ and the mixing angle is given by

$$\theta(\mathbf{R_n}) = \frac{1}{2}\tan^{-1}\left(\frac{2V_{12}^d}{V_{22}^d - V_{11}^d}\right). \tag{2.38}$$

The adiabatic PE is expressed as:

$$V_{1,2}^a = \frac{1}{2}\left[(V_{11}^d + V_{22}^d) \pm \sqrt{(V_{11}^d - V_{22}^d)^2 + (2V_{12}^d)^2}\right]. \tag{2.39}$$

2.5 Construction of diabatic basis set

After this discussion of conical intersections, as well as the adiabatic and diabatic representations, it is necessary to mention practical ways to perform the diabatization (more accurate, quasidiabatization) for real systems. In this section, I review three commonly employed diabatization methods.

2.5.1 Diabatization based on derivative couplings

This type of quasidiabatization method, originally proposed by Smith and by Baer [170, 173], takes the adiabatic-to-diabatic transformation matrix in Eq. 2.30 to eliminate the derivative coupling elements. The formal solution of this equation can be written in the form of a contour integral [170, 175–178]:

$$\mathbf{U}(\mathbf{R}) = \mathbf{U}(\mathbf{R_0}) - \int_\Gamma d\mathbf{R}' \cdot \mathbf{F^a}(\mathbf{R}')\mathbf{U}(\mathbf{R}'), \tag{2.40}$$

where Γ is a contour from $\mathbf{R_0}$ to $\mathbf{R}$. For the two-state case, the mixing angle is determined by:

$$\theta(\mathbf{R}) = \theta(\mathbf{R_0}) - \int_\Gamma d\mathbf{R}' \cdot \vec{F}_{12}^a(\mathbf{R}'). \tag{2.41}$$

Since the longitudinal part can be entirely removed by this procedure, it is probably the most precise way to obtain optimum quasidiabatic states.

Although the method discussed so far is the most accurate one, it requires the largest computational effort to determine the derivative coupling over a large range of nuclear coordinates. In addition, in the vicinity of a conical intersection, a large amount of calculations has to be performed because the nonadiabatic coupling displays a sharp peak, which requires a very dense grid in nuclear coordinate space. Despite recent progress in electronic-structure methods, this calculation is still a serious bottleneck, especially for polyatomic molecules. Thus, this direct method needs a lot of computational time.

2.5.2 Diabatization based on electronic wavefunctions

To avoid a large computational effort required for the evaluation of the derivative couplings, an alternative diabatization method has been proposed, which is based on the properties of adiabatic wavefunctions. As discussed above, the large nonadiabatic coupling at conical intersections is the result of an abrupt change of the orbital character of the adiabatic electronic wavefunctions. The elimination of such fast configuration changes of electronic wavefunctions provides a natural way to determine the transformation between the adiabatic and diabatic representation. The methods based on this idea can be divided into two types. The first type tries to enforce the smoothness of a suitable physical property, such as the DM [179, 180], the quadrupole moment [181] and the transition dipole moment (TDM) [182, 183]. Because the eigenstates of such operators remove the singular couplings at the intersection, the diagonalization of such operators in the subspace of the intersecting electronic states provides us the (quasi)diabatic basis [184]. The second type of methods tries to directly obtain the electronic wavefuntions as smooth functions of the nuclear geometry [185–192]. The starting point of this approach is to choose reference states or configurations, which are sufficiently diabatic, at a particular nuclear geometry. The diabatic wavefunctions should weakly depend on the nuclear coordinates $\mathbf{R_n}$ and change as little as possible with small displacements away from the reference geometry. The block-

diagonalization of the electronic Hamiltonian has been derived from the least-action principle [185, 186]. This method has been further extended [188, 189] and implemented in the quantum chemistry package MOLPRO [191, 193].

These wave-function based methods require less computational effort than the evaluation of the derivative coupling. On the other hand, the quality of the diabatic basis is not easily controlled and is dependent on the physical properties of the system. In this sense, these methods are still far from black-box methods. The direct *ab initio* diabatization methods, as well as their numerical implementations, are subjects of ongoing research.

2.5.3 Diabatization based on potential energies

Instead of the two rather sophisticated methods described above, an even simpler approach has been chosen in this work, which is inherently more approximate and relies only on PEs themselves [4, 41, 194, 195]. According to Eqs. 2.35 and 2.38, the unitary transformation matrix $\mathbf{U}$ diagonalizes the diabatic potential matrix $\mathbf{V^d}$ to generate its eigenvalues, corresponding to the diagonal elements of the adiabatic potential matrix $\mathbf{V^a}$. Therefore, the diabatic electronic potentials can be constructed from the adiabatic potential if we have some information on the adiabatic-to-diabatic mixing angle.

2.5.3.1 Vibronic coupling Hamiltonian

Let us consider a suitable reference geometry, such as the equilibrium geometry of the electronic ground state or the conical intersection itself. We consider small nuclear displacements, such as the displacements along the internal coordinates or normal coordinates, to calculate the adiabatic PE and construct the diabatic Hamiltonian. A convenient way to describe the normal mode displacements from the reference geometry is to choose dimensionless normal coordinates Q_j, with associated frequencies ω_j. This set of coordinates is convenient to express the kinetic and potential part of the vibrational Hamiltonian in the harmonic ap-

proximation as

$$\hat{H}_{vib} = \sum_j \hat{T}_j + \hat{V}_j \tag{2.42}$$

$$\hat{T}_j = -\frac{1}{2}\omega_j \frac{\partial^2}{\partial Q_j^2} \tag{2.43}$$

$$\hat{V}_j = \frac{1}{2}\omega_j Q_j^2. \tag{2.44}$$

The details of the construction of dimensionless normal coordinates can be found in Appendix A.

The PE functions and the diabatic interstate couplings can be expressed as Taylor expansions up to second order with respect to the dimensionless normal coordinates at the reference geometry:

$$\mathbf{V} = \begin{pmatrix} V_{11} & V_{12} \\ V_{21} & V_{22} \end{pmatrix} \tag{2.45}$$

with

$$V_{11}(\mathbf{Q}) = E_1 + V_0(\mathbf{Q}) + \sum_t \kappa_t^{(1)} Q_t + \sum_{m,m'} \gamma_{m,m'=t,c}^{(1)} Q_m Q'_m, \tag{2.46}$$

$$V_{22}(\mathbf{Q}) = E_2 + V_0(\mathbf{Q}) + \sum_t \kappa_t^{(2)} Q_t + \sum_{m,m'} \gamma_{m,m'=t,c}^{(2)} Q_m Q'_m, \tag{2.47}$$

$$V_{12}(\mathbf{Q}) = V_{21}(\mathbf{Q}) = \sum_c \lambda_c Q_c, \tag{2.48}$$

$$V_0(\mathbf{Q}) = \frac{1}{2}\sum_t \omega_t Q_t^2 + \frac{1}{2}\sum_t \omega_c Q_c^2, \tag{2.49}$$

where E_1 and E_2 are energies of the two electronic states at the reference geometry. The $\kappa_t^{(n)}\,(n = 1, 2)$ are the gradients of the PE functions at the reference geometry and they represent the first-order intra-state couplings. Since the modes Q_t tune the energy gap of two electronic states and may lead to a crossing between diabatic PE surfaces, they are termed "tuning modes" [4, 42]. The λ_c represents the first-order inter-state electronic-vibronic coupling constant and the modes Q_c are called "coupling modes" [4, 42]. The intra-state bilinear coupling constants $\gamma_{m,m'}^{(n)}\,(n = 1, 2)$ are related to the so-called "Dushinsky effect"(rotations of the normal modes due to the coupling of the state n and the vibrational motion) [4, 42].

Eq. 2.45 defines a class of model Hamiltonians describing the coupling between electronic motion and nuclear vibration, which are called "vibronic coupling Hamiltonians". Retaining only the first-order coupling constants leads to "the linear coupling model", which has been used in many calculations of low-resolution absorption spectra, photoelectron spectra, time-resolved spectra and nonadiabatic dynamics of polyatomic molecules [4, 41].

2.5.3.2 Symmetry selection rules

The selection of the most important tuning and coupling modes play a central role in the characterization of a conical intersection. Eq. 2.45 itself provides a way to identify the tuning and coupling modes through symmetry selection rules.

Let us assume that the two electronic states belong to different irreducible representations, Γ_1 and Γ_2, respectively. Since the electronic Hamiltonian is always totally symmetric, the linear intra-state electron-vibrational coupling coefficients

$$\kappa_t^{(n)} = \langle \Phi_n | \frac{\partial \hat{H}_{el}}{\partial Q_t} | \Phi_n \rangle \Big|_{\mathbf{Q_0}} \tag{2.50}$$

can be nonzero only for the totally symmetric coordinates. These nonzero gradients induce the nuclear motions in the electronic states. Thus, a linear combination of the tuning coordinates defines the minimum-energy reaction path.

For the coupling modes, the direct product of the irreducible representations of two states and the vibrational motion must contain A_1:

$$\Gamma_1 \times \Gamma_{Q_c} \times \Gamma_2 \supset A_1 \quad \Rightarrow \quad \Gamma_{Q_c} = \Gamma_1 \times \Gamma_2. \tag{2.51}$$

In this case, the inter-state coupling constant

$$\lambda_c^{nm} = \frac{\partial}{\partial Q_c} \langle \Phi_n | \hat{H}_{el} | \Phi_m \rangle \Big|_{\mathbf{Q_0}} \tag{2.52}$$

is nonzero.

For the special case $\Gamma_1 = \Gamma_2$, two states with the same symmetry can cross, leading to so-called "accidental intersections", which are relevant in many photo-induced excited-state processes. For this type of conical intersection, both of the tuning and coupling modes are of A_1 symmetry.

2.5.3.3 Coupling constants

When there is no displacement along coupling coordinates, $Q_c = 0$, the diabatic states are identical with the adiabatic states. Thus, the diagonal elements of the PE matrix as functions of Q_t can be determined by performing least-square fits to the *ab initio* results.

For a coupling coordinate, we first rewrite the adiabatic-to-diabatic transformation (Eq. 2.39) for the two-state problem as

$$V_1^a + V_2^a = V_{11}^d + V_{22}^d, \tag{2.53}$$

$$(V_1^a - V_2^a)^2 = (V_{11}^d - V_{22}^d)^2 + (V_{12}^d)^2. \tag{2.54}$$

These two equations explain how one can obtain the diabatic PEs (V_{11}^d, V_{22}^d), as well as their coupling V_{12}^d, from the adiabatic potential energies V_1^a and V_2^a. The fitting procedure based on the first equation yields the sum of the two diabatic potential functions as functions of Q_c, while the fitting based on the second equation predicts the energy difference of the two diabatic states, as well as their coupling.

In the linear vibronic coupling model, the linear intra-state coupling constants $\kappa_t^{(n)}$ of Eq. 2.50 can also conveniently be determined as the energy gradient of the electronic states at the reference geometry $\mathbf{Q}_0$ [4, 41]:

$$\kappa_t^{(1,2)} = \left.\frac{\partial V_{1,2}^d}{\partial Q_t}\right|_{\mathbf{Q}_0}. \tag{2.55}$$

The interstate coupling, λ_c, can be estimated according to [4, 41]:

$$\lambda_c = \left.\left[\frac{1}{8}\frac{\partial^2}{\partial Q_c^2}(V_1^a - V_2^a)^2\right]\right|_{\mathbf{Q}_0}. \tag{2.56}$$

2.6 Topography of conical intersections

To illustrate the characteristic features of conical intersections, we consider an example: the conical intersection of the $S_1(n\pi^*)$ and $S_2(\pi\pi^*)$ surfaces of pyrazine [194].

This conical intersection has been characterized by *ab inito* calculations. The S_1 and S_2 states of pyrazine belong to $^1B_{3u}$ and $^1B_{2u}$ symmetry, respectively.

Within the normal-mode approach, the *ab initio* calculations have revealed that the coordinates Q_{6a} and Q_{10a} are the dominant tuning and coupling coordinates, respectively. Fig. 2.1 shows the shape of the conical intersection in the space spanned by these tuning and coupling coordinates. The global view of the surfaces in Fig. 2.1 (a) shows that there is a point of contact of the two adiabatic surfaces. Looking at the conical intersection more closely in Fig. 2.1 (b), we immediately note the double-cone shape of the adiabatic PE surfaces in the vicinity of the intersection. The diabatic PE surfaces and the diabatic PE coupling are shown in Fig. 2.1 (c) and (d), respectively. In contrast to the adiabatic surfaces, the diabatic surfaces and the diabatic coupling are smooth functions of the nuclear geometry.

The characters of the electronic wavefunctions are directly reflected by their physical properties, such as TDMs. Consistent with the previous discussion, Fig. 2.2 shows that the x and y components of the S_0-S_1 TDM vary rapidly as functions of the nuclear coordinate, reflecting the abrupt changes of the electronic wavefunctions in the vicinity of the conical intersection. The corresponding elements in the diabatic representation, on the other hand, obtained by the adiabatic-to-diabatic transformation, become smooth functions of Q_{6a} and Q_{10a}. This reflects the fact that the diabatic wavefunctions are slowly varying functions of the nuclear geometry.

The mixing angle defined in Eq. 2.38 is displayed in Fig. 2.3 (a). The discontinuity is related to the well-known topological phase or "Berry phase"(see later discussions), which is enforced by the conical intersection. The derivatives $\partial\theta/\partial Q_{6a}$ and $\partial\theta/\partial Q_{10a}$, which determine the first-order nonadiabatic couplings in Eq. 2.33, are shown in Fig. 2.3 (b) and (c), respectively. As expected, they are singular at the conical intersection.

For general molecular systems with N internal degrees of freedom, many tuning and coupling modes can be involved in the characterization of the conical intersection. In the multi-mode case, an alternative language may be chosen to describe the topology of a conical intersection. This is the so-called g–h branching space introduced by Yarkony [24,26] and Robb [28,30,196]. The directions of

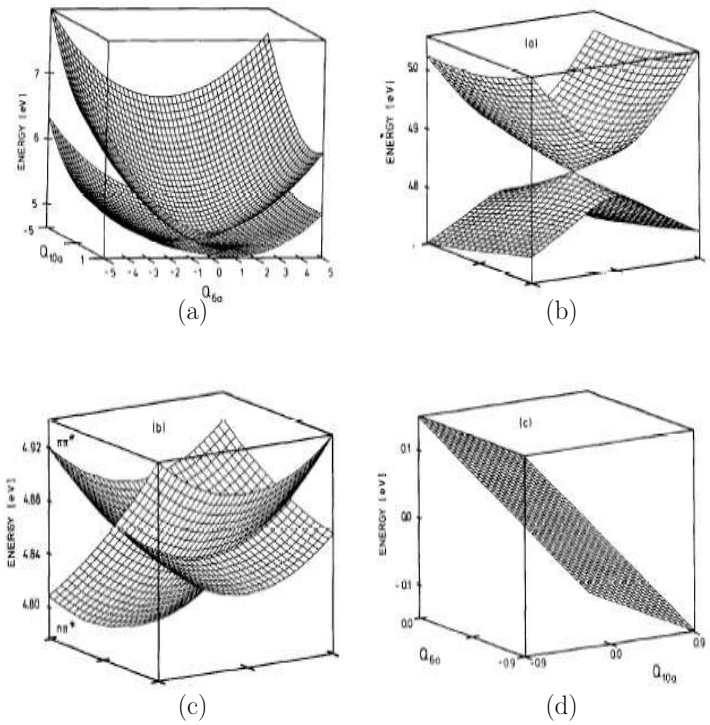

Figure 2.1: View of the conical intersection between the S_1 and S_2 excited states of pyrazine in the two-dimensional space spanned by the tuning coordinate Q_{6a} and the coupling coordinate Q_{10a}: (a) global view of the adiabatic PE surfaces; (b) close-up view of the adiabatic PE surfaces; (c) close-up view of the diabatic PE surfaces; (d) the diabatic coupling element. See Ref. [194] for details.

maximum energy-gradient difference and the nonadiabatic coupling vectors define the so-called g and h vectors, respectively. The topography of the conical intersection (the double cone shape) can be displayed in this g–h branching space. If all degrees of freedom are taken into account, the conical intersection actually occurs along a intersection seam with the dimension N-2.

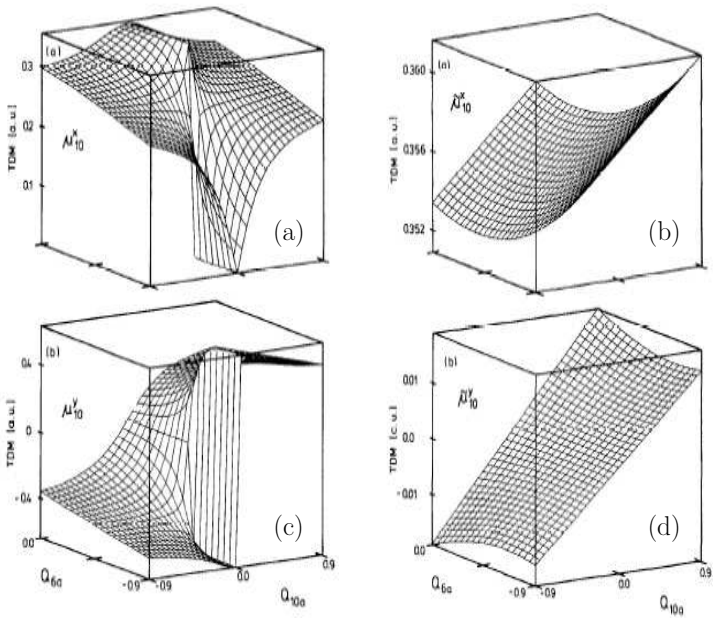

Figure 2.2: The S_0-S_1 TDMs as functions of the tuning coordinate Q_{6a} and the coupling coordinate Q_{10a}: the x component in adiabatic (a) and diabatic (b) representation; the y component in adiabatic (c) and diabatic (d) representation. See Ref. [194] for details.

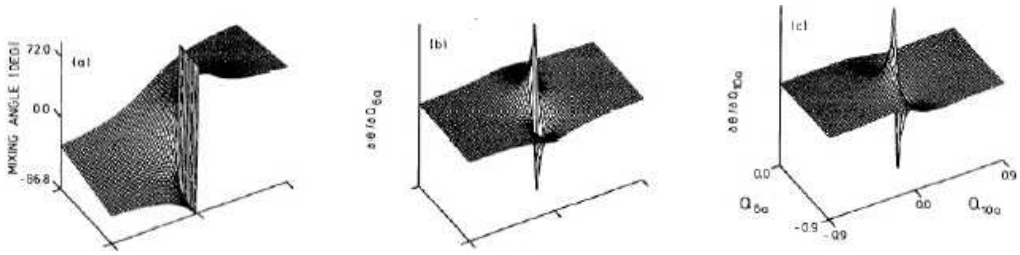

Figure 2.3: The mixing angle (a) and the nonadiabatic coupling elements, *i.e.* the derivative of the mixing angle over the tuning coordinate Q_{6a} (b) and the coupling coordinate Q_{10a} (c). See Ref. [194] for details.

2.7 Geometric phase

When an adiabatic electronic wavefunction Φ_i is transported on the lower (or upper) cone around a closed circle, we expect that Φ_i should return to itself after a loop, that is, Φ_i should be a single-valued function. This expectation is correct when the circle does not contain a conical intersection. The transport of Φ_i around a closed loop surrounding a conical intersection leads to an sign change of the adiabatic electronic wavefunction [14, 22]. This is the so-called geometric phase or the Berry phase. Within the g–h space, the relation can be expressed in the polar coordinates (ρ, ϑ) as:

$$\Phi_i(\rho, \vartheta + 2\pi) = -\Phi_i(\rho, \vartheta). \tag{2.57}$$

As a consequence, the nuclear wavefunction must change its sign to compensate this effect.

There are two ways to include the Berry phase effect in the theoretical treatments of conical intersections in the adiabatic representation. The first option is to maintain real electronic wavefunctions and to add Eq. 2.57 as the boundary condition. Then the adiabatic wavefunctions become double-valued functions. An alternative approach is to employ complex electronic wavefunctions. This complex function can be chosen to be single valued ones and to undergo smooth changes along the closed path encircling the conical intersection [4, 37].

In fact, the Berry phase is a general phenomenon in adiabatic transport processes, reflecting the geometrical properties of the Hamiltonian [197–200]. This phase difference does not arise from the dynamical properties but from the geometric properties of the Hamiltonian, reflecting the existence of a holonomy [197]. It appears, in particular in the theories of the Aharonov-Bohm effect and of conical intersections. Therefore, the geometric phase effect at a conical intersection is also called the "molecular Aharonov-Bohm effect" [201].

2.8 Effective tuning and coupling modes

For a general conical intersection, it is quite common that a large number of tuning or coupling modes are involved in the description of the nonadiabatic dynamics. Despite the progress of quantum dynamics in the last 30 years, the computational cost of the dynamics calculations increases dramatically with the inclusion of more degrees of freedom. One possible way to explore the multi-mode nonadiabatic dynamics at conical intersections is to use the "effective-mode" approach [41, 202–204].

Consider the linear vibronic-coupling Hamiltonian given by:

$$\begin{aligned}\hat{H} = \quad & \sum_t \frac{\omega_t}{2}(-\frac{\partial^2}{\partial Q_t^2}^2 + Q_t^2)\mathbf{I} + \sum_c \frac{\omega_c}{2}(-\frac{\partial^2}{\partial Q_c^2} + Q_c^2)\mathbf{I} \\ & + \begin{pmatrix} \sum_t \kappa_t^{(1)} Q_t & \sum_c \lambda_c Q_c \\ \sum_c \lambda_c Q_c & \sum_t \kappa_t^{(2)} Q_t \end{pmatrix} + \begin{pmatrix} E_1 & 0 \\ 0 & E_2 \end{pmatrix}, \end{aligned} \tag{2.58}$$

where $\mathbf{I}$ is a unit matrix and all variables are defined as before. Next we define a unitary matrix $\mathbf{S}$ which transforms the original set of coordinates $\mathbf{Q} = (Q_t, Q_c)$ to the new set of coordinates $\mathbf{X}$ [41, 202–204]

$$\mathbf{Q} = \mathbf{S}\mathbf{X} \tag{2.59}$$

The first two elements in $\mathbf{X}$ can be defined as the linear combinations of all tuning coordinates [41, 202–204]

$$X_1 = \frac{1}{K_1}\sum_t \frac{1}{2}\left(\frac{\kappa_t^{(1)}}{\overline{\kappa}^{(1)}} + \frac{\kappa_t^{(2)}}{\overline{\kappa}^{(2)}}\right) Q_t, \tag{2.60}$$

$$X_2 = \frac{1}{K_2}\sum_t \frac{1}{2}\left(\frac{\kappa_t^{(1)}}{\overline{\kappa}^{(1)}} - \frac{\kappa_t^{(2)}}{\overline{\kappa}^{(2)}}\right) Q_t, \tag{2.61}$$

$$\overline{\kappa}^{(1)} = \sqrt{\sum_t (\kappa^{(1)})^2}, \tag{2.62}$$

$$\overline{\kappa}^{(2)} = \sqrt{\sum_t (\kappa^{(2)})^2}, \tag{2.63}$$

where $K_{1,2}$ are normalization factors. The third coordinate is defined as a linear

combination of all coupling coordinates:

$$X_3 = \sum_c \frac{\lambda_c}{\overline{\lambda}} Q_c, \tag{2.64}$$

$$\overline{\lambda} = \sqrt{\sum_c \lambda_c^2}. \tag{2.65}$$

These three modes are orthogonal to each other. The first three rows of the transformation matrix $\mathbf{S}$ are

$$S_{i,1} = \frac{1}{2K_1}\left(\frac{\kappa_t^{(1)}}{\overline{\kappa}^{(1)}} + \frac{\kappa_t^{(2)}}{\overline{\kappa}^{(2)}}\right), \tag{2.66}$$

$$S_{i,2} = \frac{1}{2K_2}\left(\frac{\kappa_t^{(1)}}{\overline{\kappa}^{(1)}} + \frac{\kappa_t^{(2)}}{\overline{\kappa}^{(2)}}\right), \tag{2.67}$$

$$S_{i,3} = \frac{\lambda_c}{\overline{\lambda}}. \tag{2.68}$$

Note that $\mathbf{S}$ is an orthogonal matrix and that the first three rows have already been obtained. The elements of other rows can be constructed because any two rows (or two columns) of the matrix $\mathbf{S}$ should be orthogonal and normalized. Using this new set of coordinates X_i, the Hamiltonian can be rearranged as [41, 202–204]:

$$\hat{H} = \hat{H}_{eff} + \hat{H}_b + \hat{V}_b, \tag{2.69}$$

$$\begin{aligned}\hat{H}_{eff} = {} & \frac{1}{2}\Omega_1(P_1^2 + X_1^2)\mathbf{I} + \frac{1}{2}\Omega_2(P_2^2 + X_2^2)\mathbf{I} + \frac{1}{2}\Omega_3(P_3^2 + X_3^2)\mathbf{I} \\ & \begin{pmatrix} \overline{\kappa}^{(1)}(K_1X_1 + K_2X_2) & \overline{\lambda}X_3 \\ \overline{\lambda}X_3 & \overline{\kappa}^{(2)}(K_1X_1 - K_2X_2) \end{pmatrix} + \begin{pmatrix} E_1 & 0 \\ 0 & E_2 \end{pmatrix} \\ & + d_{12}\left(-\frac{\partial^2}{\partial X_1 \partial X_2} + X_1X_2\right)\mathbf{I},\end{aligned} \tag{2.70}$$

$$\hat{H}_b = \sum_{i>3} \frac{1}{2}\Omega_i(P_i^2 + X_i^2)\mathbf{I} \tag{2.71}$$

$$+ \sum_{j>3}\sum_{i>j} d_{ij}\left(-\frac{\partial^2}{\partial X_i \partial X_j} + X_iX_j\right)\mathbf{I}, \tag{2.72}$$

$$\hat{V}_b = \sum_{j=1}^{3}\sum_{i>3} d_{ij}\left(-\frac{\partial^2}{\partial X_i \partial X_j} + X_iX_j\right)\mathbf{I} \tag{2.73}$$

with

$$\Omega_i = \sum_j \omega_j S_{ji}^2, \tag{2.74}$$

$$d_{ij} = \sum_k \omega_k S_{ki} S_{kj}. \tag{2.75}$$

Here, the original Hamiltonian is divided into an effective part $\hat{H}_{eff}$, which describes the coupling between two electronic states, an environment part $\hat{H}_b$, which does not reflect the vibronic coupling of different electronic states, and a system-environment coupling term $\hat{V}_b$. The effective part $\hat{H}_{eff}$ includes three coordinates, two effective tuning coordinates $X_{1,2}$ and one effective coupling coordinate X_3. $\Omega_{1,2}$ and Ω_3 are frequencies of the two effective tuning modes and the effective coupling mode, respectively. $\overline{\kappa^{(1)}}$, $\overline{\kappa^{(2)}}$ and $\overline{\lambda}$ are effective coupling constants. The environment part $\hat{H}_b$ contains two parts: the energy of the environment modes, as well as their couplings. The interaction term $\hat{V}_b$ describes the couplings between the effective modes and the environment modes.

Since $\hat{H}_b$ and $\hat{V}_b$ do not induce nonadiabatic transitions between different electronic states at conical intersections, it is possible to drop them, thus reducing the dimensionality of the model to three. This elimination will largely reduce the computational cost. The effect of neglecting $\hat{V}_b$, the couplings between the environment modes and the effective modes, should be examined. Here, $\mathbf{S}$ is an unitary matrix, in which any two rows (or columns) should be orthogonal. Thus, if the frequencies of the tuning or coupling modes are quite similar, Eq. 2.75 indicates $d_{ij} \sim 0$ and the coupling term $\hat{V}_b$ can be ignored.

For a system with a large number of tuning and coupling modes of different frequencies, a few effective modes, instead of only three, can be constructed to describe the conical intersection approximately. Each effective mode can represent a group of modes with similar frequencies. Previous calculations have already confirmed the efficiency of the effective-mode approximation in short-time dynamics calculations [41, 202–204].

Chapter 3

Electronic-structure theory

The first step in the characterization of conical intersections is to obtain adiabatic PE surfaces from *ab initio* calculations. Although descriptions of the most common electronic-structure methods can be found in any standard textbook of quantum chemistry [205,206], this chapter gives a brief discussion of the *ab initio* methods which are used in our calculations, to make the thesis self-contained.

3.1 Hartree-Fock method

The time-independent Schrödinger equation of a many-electron system can be written as:

$$\hat{H}_e(\mathbf{R_n})\Phi_i(\mathbf{r_e},\mathbf{R_n}) = V_i(\mathbf{R_n})\Phi_i(\mathbf{r_e},\mathbf{R_n}), \tag{3.1}$$

$$\hat{H}_e(\mathbf{R_n}) = -\frac{1}{2}\sum_i \nabla_i^2 - \sum_{A,i}\frac{Z_A}{r_{Ai}} + \sum_{A>B}\frac{Z_A Z_B}{r_{AB}} + \sum_{i>j}\frac{1}{r_{ij}} \tag{3.2}$$

where the first term of $\hat{H}_e$ describes the kinetic energies of electrons, the second term is the nuclei-electron interaction, and the third and forth terms describe the nuclei-nuclei and electron-electron pair interactions, respectively.

For a N-electron molecule, the Slater determinant is used to express the total

electronic wavefunction to satisfy the antisymmetry principle:

$$\Phi(r_1, ...r_n) = \begin{pmatrix} \phi_1(r_1) & \phi_2(r_1) & ... & \phi_n(r_1) \\ \phi_1(r_2) & \phi_2(r_2) & ... & \phi_n(r_2) \\ ... & ... & ... & ... \\ \phi_1(r_n) & \phi_2(r_n) & ... & \phi_n(r_n) \end{pmatrix}, \tag{3.3}$$

where $\{\phi_i\}$ is a set of orthogonal spin orbitals and r_i is the position of the ith electron.

For the ground electronic state, the variational theorem gives:

$$\frac{\langle \Phi | \, \hat{H}_e \, | \Phi \rangle}{\langle \Phi | \, \Phi \rangle} = E_{HF} \geq E_g. \tag{3.4}$$

The energy E_{HF} is an upper bound to the true ground-state energy E_g. The purpose of the Hartree-Fock (HF) method is to determine a set of spin orbitals which minimize the energy and thus generate the "best single determinant".

The spin orbitals satisfy the HF equations:

$$\hat{F}_i(r_i)\phi_i(r_i) = e_i\phi_i(r_i), \tag{3.5}$$

where $\hat{F}_i(r_i)$ is the Fock operator:

$$\hat{F}_i(r_i) = \hat{h}_i(r_i) + \sum_j (\hat{J}_j(r_i) - \hat{K}_j(r_i)), \tag{3.6}$$

$$\hat{h}_i(r_i) = -\frac{1}{2}\nabla_i^2 + \frac{Z_A}{r_{Ai}}, \tag{3.7}$$

$$\hat{J}_j(r_i) = \int dr_j \frac{|\phi_j(r_j)|^2}{r_{ij}}, \tag{3.8}$$

$$\hat{K}_j(r_i) = \int dr_j \frac{\phi_i(r_j)^* \phi_j(r_j)}{r_{ij}} \tag{3.9}$$

where $\hat{h}_i(r_i)$ is the one-lectronic Hamiltonian. The operator $\hat{J}_j$ represents the Coulomb interaction between electron i and j, which corresponds to the average potential acting on electron i at position r_i due to the Coulomb interaction with electron j in orbital $\phi_j(r_j)$. The exchange term $\hat{K}_j$ arises from the antisymmetry requirement of the electronic wavefunction due to the Pauli principle. In other words, the motion of electron i is not only dependent on the single-particle

Hamiltonian $\hat{h}_i$ but is also determined by the average potential field formed by the other electrons.

The HF energy is given by:

$$\begin{aligned} E_{HF} = \sum_i & \int dr_i \phi_i^*(r_i) h_i(r_i) \phi_i(r_i) \\ + \frac{1}{2} \sum_{i,j} & [\int dr_i dr_j \frac{\phi_i^*(r_i)\phi_j^*(r_j)\phi_i(r_i)\phi_j(r_j)}{r_{ij}} \\ & - \int dr_i dr_j \frac{\phi_i^*(r_j)\phi_j^*(r_i)\phi_i(r_i)\phi_j(r_j)}{r_{ij}}] \end{aligned} \tag{3.10}$$

For a molecular system with many electrons, the HF equations cannot be solved directly. Thus the atomic orbitals $\{\varphi_k\}$ of every atom can be used as a set of basis functions to expand the molecular orbitals

$$\phi_i = \sum_k c_{ki} \varphi_k \tag{3.11}$$

as the linear combinations of atomic orbitals (LCAO). The HF equations then become the Hartree-Fock-Roothaan equations:

$$\sum_k F_{lk} c_{ki} = e_i \sum S_{lk} c_{ki}, \tag{3.12}$$

$$F_{lk} = \int dr_i \varphi_l^*(r_i) F_i(r_i) \varphi_k(r_i), \tag{3.13}$$

$$S_{lk} = \int dr_i \varphi_l^*(r_i) \varphi_k(r_i), \tag{3.14}$$

or in a matrix form:

$$\mathbf{FC} = \mathbf{SCE}, \tag{3.15}$$

where $\mathbf{E}$ is the diagonal matrix of the orbital energies e_i. Since $\mathbf{F}$ depends on $\mathbf{C}$, we have to solve these equations by an iterative procedure, the self-consistent-field (SCF) procedure.

3.2 Multi-configuration self-consistent-field method

As a "mean field"theory, the HF equations cannot describe electron correlations. When two electrons come close to each other, an increased repulsion exists be-

tween them. The difference between the HF energy in the basis-limit and the real ground-state energy is called the correlation energy [207].

If two electronic states of the same symmetry are close to each other, their wavefunctions can be highly mixed. This reflects the so-called non-dynamical or near-degeneracy correlations [207]. In such cases, a single Slater determinant cannot describe the electronic wavefunctions properly. The appropriate way to include the near-degeneracy electronic correlation is the multi-configuration self-consistent field (MCSCF) method.

The starting point of this approach is configuration-interaction (CI) ansatz, which employ more than one Slater determinant to construct the so-called CI wavefunction:

$$\Phi_{ci} = \sum_i C_i \Phi_i. \tag{3.16}$$

Here Φ_0 is the single-determinant wavefunction obtained by a HF calculation and contains the information of the reference orbitals. $\Phi_i\,(i > 0)$ denote different determinants which are obtained by exciting electrons from the occupied spin orbitals to the virtual orbitals in Φ_0. The coefficient vector $\{C_i\}$ can be determined by the variational theorem.

In the traditional single-reference CI approach, the CI expansion is constructed based on the single-reference HF orbitals. To take the near-degeneracy correlation effects into account, both the orbitals and the CI vector are simultaneously optmized. This is the multi-configuration self-consistent field (MCSCF) method [205, 207].

3.3 Complete-active-space self-consistent-field method

The inclusion of all possible excitations from Φ_0 leads a computational method called "full CI". The molecular energy obtained in the full CI limit is a benchmark because it is the most complete treatment for a given one-electronic basis set. Full CI is not a practical method due to large computational costs, even for small

molecules.

The CI expansion can be truncated by restricting the types of electronic excitations to reduce the number of determinants. For example, the inclusion of single excitations, double excitations, or both of them are approximations which are known as "CIS", "CID" and "CISD".

a useful way to reduce the computational cost is to restrict the excitations within a particular orbital space, the so called "active space". This approximation is quite reasonable, because usually only a few active orbitals are involved in chemical reactions. For a given active space, the inclusion of all possible excitations leads to the so-called complete-active-space (CAS) treatment. The combination of CAS and MCSCF is the complete-active-space self-consistent field (CASSCF) approach [205, 207, 208].

The advantage of the above methods is that they are variational. This means that the calculated energies are always upper bounds to the true energy. However, most of these calculations apply a truncated CI expansion. They are therefore not size-consistent, because only the correlation energy in the active space is included in calculations.

3.4 Multi-reference configuration-interaction method

Although the MCSCF wavefunction accounts for the near-degeneracy correlations, its energy usually is not sufficient accurate, since many of the valence electrons have been treated as filled closed-shell orbitals with no recovery of correlation energy. The remaining correlations which cannot be described by MCSCF are the so-called dynamical correlations [207].

To recover the dynamical correlation energy, it is necessary to consider the excitation of the active electrons or inert valence electrons to the external (or virtual) orbitals of the MCSCF wavefunction. The most obvious approach to improve the MCSCF approach is the multi-reference configuration-interaction (MRCI) method [207]. This method takes the MCSCF results as the reference

wavefunction and consider the excitation of electrons from the MCSCF configurations into the external orbital space. In general, only single and double excitations are considered, which leads to first-order CI (FOCI) and second-order CI (SOCI), respectively. Previous studies showed that FOCI is not a systematic improvement over MCSCF, while SOCI generally provides accurate results [207]. Unfortunately, MRCI is expensive except in the case of small molecules.

Chapter 4

Quantum wave-packet dynamics

4.1 Kinetic-energy operator

The nuclear kinetic energy of a polyatomic molecule is composed of three parts: translational energy, rotational energy and vibrational energy [209]. Among them, only the vibrational part is of interest here because it describes the changes of the internal nuclear degrees of freedom in photo-induced dynamics. The separation of vibrations and rotation is performed in a curvilinear coordinate system and leads to complex expressions for the vibrational kinetic-energy operator.

The derivation of the exact kinetic-energy operator for the vibrational motion of a polyatomic system is straightforward in principle but cumbersome in practice. There are two equivalent approaches to perform this task. We consider a nonlinear polyatomic molecule with N atoms as a typical example to derive the kinetic-energy operator through these two methods.

In the first approach, the total kinetic energy is expressed as a function of classical velocities. There are a total of $3N$ degrees of freedom. The motion of the center of mass of this molecule, as well as its rotational motion, should be separated from the total kinetic-energy Hamiltonian. After the separation, $3N$-6 degrees of freedom are left to describe the vibrational motion. In a curvilinear internal coordinate system, the classical kinetic energy of the vibrational motion

is obtained as:

$$T = \frac{1}{2}\mathbf{P^T G(R) P}, \tag{4.1}$$

where $\mathbf{P}$ is a column vector and its element P_i is the momentum conjugate to the curvilinear coordinate R_i. $\mathbf{G(R)}$ is the well-known $\mathbf{G}$ matrix [209]. The Podolsky transformation [210] finally yields the corresponding quantum-mechanical kinetic-energy operator:

$$\hat{T} = \frac{1}{2} g^{\frac{1}{4}} \sum_{i,j=1}^{3N-6} \hat{P}_i g^{-\frac{1}{2}} G_{ij} \hat{P}_j g^{\frac{1}{4}} \tag{4.2}$$

$$\hat{P}_i = i\frac{\partial}{\partial R_i} \tag{4.3}$$

where G_{ij} is the element of the matrix $\mathbf{G}$ and $g = \det(\mathbf{G})$.

The second approach starts from the quantum kinetic-energy operator in a Cartesian-coordinate system. It is possible to define a new set of coordinates $\{X_i\}$. The first three coordinates X_1, X_2, X_3 describe the translational motion of the center of mass and the second three coordinates X_4, X_5, X_6 describe the rotation. Then a set of proper curvilinear coordinates from X_7 to X_{3N} can be selected to describe the vibrational motions. The transformation between the Cartesian coordinates and the $\{X_i\}$ can be constructed explicitly. By successive application of the chain rule, the final kinetic-energy operator can be obtained [211–215]. This method was used to construct the kinetic-energy operator of tri-atomic and tetra-atomic molecules and has been extended to larger systems with the help of computer algebra [211–215].

For polyatomic systems, both methods demand cumbersome calculations. Thus some approximations should be introduced to simplify the derivation of the kinetic-energy operators, such as the reduction of the dimensionality and the selection of the appropriate coordinates, which simply the kinetic-energy expression.

In general, the photoinduced chemical dynamics in excited states of molecules, especially for the short-time (sub-picosecond) dynamics, involve only a few nuclear degrees of freedom. Thus, to simplify the treatment of the dynamics, it may

be appropriate to build a reduced dimensional model, by including the most important degrees of freedom, while freezing the other (inactive) vibrational modes. In this case, the approximate kinetic-energy operator can be derived based on the first approach [216]. The classical kinetic energy can be obtained with constraints that are introduced in the form of the constant bond distances or constant bond angles. The Podolsky transformation, in Eq. 4.2, gives the corresponding quantum mechanical operator of the kinetic energy for such constrained systems.

The selection of proper coordinates plays a key role in simplifying the expression of the kinetic-energy operator [215]. In the present thesis, three sets of coordinates are used: internal coordinates, Jacobi coordinates and normal coordinates. The internal coordinates, such as bond distances and bond angles, are optimal for the description of the PE surfaces, but often lead to complex expressions for the kinetic-energy operator. The Jacobi coordinates are suitable to derive a simple expression for the kinetic-energy operator for a reduced system with two or three degrees of freedom, but the constraints (*e.g.* fixed bond distances or bond angles) cannot be introduced easily. The normal coordinates yield the simplest expression for the kinetic operator, but are unsuitable for the description of large-amplitude motion. Since these three sets of the coordinates each have advantages and limitations, the selection of the suitable coordinates depends on the system under study.

4.2 Time-independent Schrödinger equation

4.2.1 General solution

The fundamental problem in chemical physics is the solution of the time-independent Schrödinger equation:

$$\hat{H} \left|\Psi(t)\right\rangle = E \left|\Psi(t)\right\rangle \tag{4.4}$$

where $\hat{H}$ is the Hamiltonian. To solve this equation, a suitable orthogonal basis set $\{|\psi_i\rangle\}$ is selected to construct the matrix representation of the Hamiltonian:

$$H_{ij} = \left\langle \psi_i \right| \hat{H} \left| \psi_j \right\rangle . \tag{4.5}$$

The diagonalization of this matrix by a unitary matrix **S** generates a series of eigenvalues ($\{E_i\}$), as well as the corresponding eigenstates ($\{|\alpha_k\rangle\}$), of the Hamiltonian:

$$\begin{aligned} \mathbf{SHS}^{+} &= \mathbf{E}, && (4.6)\\ S_{ik} &= \langle \alpha_i |\, \psi_k \rangle\,, && (4.7)\\ E_{ij} &= \delta_{ij} E_i. && (4.8) \end{aligned}$$

The transformation between the eigenstates $|\alpha_k\rangle$ and the original basis states $|\psi_i\rangle$ is given by the elements of the matrix **S**.

4.2.2 Partitioning of the Hamiltonian

If the Hamiltonian cannot be diagonalized directly in a single basis set, it can be divided into a sum of different terms, *i.e.*:

$$\hat{H} = \hat{H}_1 + \hat{H}_2. \quad (4.9)$$

Let us consider two basis sets $\{|\alpha_i\rangle\}$ and $\{|\beta_i\rangle\}$, which are eigenstates of $\hat{H}_1$ and $\hat{H}_2$ respectively:

$$\begin{aligned} \hat{H}_1 |\alpha_i\rangle &= E_i^{(1)} |\alpha_i\rangle\,, && (4.10)\\ \hat{H}_2 |\beta_i\rangle &= E_i^{(2)} |\beta_i\rangle\,, && (4.11) \end{aligned}$$

where $E_i^{(1)}$ and $E^{(2)}$ are the corresponding eigenvalues. The Hamiltonian can be represented in one basis set (*e.g.* $\{|\alpha_i\rangle\}$) as follows:

$$\begin{aligned} H_{ij} &= \langle \alpha_i | \hat{H}_1 |\alpha_j\rangle + \sum_{k,l} \langle \alpha_i |\, \beta_k\rangle \langle \beta_k | \hat{H}_2 |\beta_l\rangle \langle \beta_l |\, \alpha_j\rangle \\ &= E_i^{(1)}\delta_{ij} + \sum_k \langle \alpha_i |\, \beta_k\rangle\, E_k^{(2)} \langle \beta_k |\, \alpha_j\rangle\,, && (4.12) \end{aligned}$$

or in the more compact form:

$$\begin{aligned} \mathbf{H} &= \mathbf{E^{(1)}} + \mathbf{L}^{+}\mathbf{E^{(2)}}\mathbf{L}, && (4.13)\\ E_{ij}^{(1)} &= \delta_{ij} E_i^{(1)}, && (4.14)\\ E_{ij}^{(2)} &= \delta_{ij} E_i^{(2)}, && (4.15)\\ L_{ij} &= \langle \beta_i |\, \alpha_j\rangle\,, && (4.16) \end{aligned}$$

where $\mathbf{E^{(1)}}$ and $\mathbf{E^{(2)}}$ are the diagonal matrices containing the eigenvalues of $\hat{H}_1$ and $\hat{H}_2$, respectively. $\mathbf{L}$ is the transformation matrix between these two basis sets. The diagonalization of the matrix $\mathbf{H}$ generates the eigenenergies and the eigenstates of $\hat{H}$.

The choice of a suitable basis set can reduce the effort to evaluate the matrix representation of Hamiltonian. Some widely-used basis sets include the eigenstates of the harmonic oscillator, the eigenstates of the Morse oscillator, the Legendre functions, *etc.* Instead of discrete basis sets, continuum basis sets can also be used to represent the Hamiltonian. For example, $|x\rangle$ is a natural choice when the Hamiltonian only contains a function of the position operator $\hat{x}$. This is equivalent to the projection of the state vector on position space to get the wavefunction. If the Hamiltonian is a function of the momentum operator (*e.g.*, the free particle), the natural basis set is $|p\rangle$, the eigenstates of the momentum operator.

4.3 Time-dependent Schrödinger equation

4.3.1 General solution

The time evolution of a wave vector $|\Psi(t)\rangle$ is described by the time-dependent Schrödinger equation:

$$i\frac{\partial}{\partial t}|\Psi(t)\rangle = \hat{H}|\Psi(t)\rangle, \tag{4.17}$$

where $\hat{H}$ is the Hamiltonian. If $\hat{H}$ is independent of time, the formal solution is:

$$|\Psi(t)\rangle = \hat{U}(t-t_0)|\Psi(0)\rangle, \tag{4.18}$$

$$\hat{U}(t-t_0) = \exp[-i\hat{H}t], \tag{4.19}$$

where $\hat{U}(t-t_0)$ is called "propagator".

Let us expand $|\Psi(t)\rangle$ in a complete set of time-independent basis state $\{|\alpha_n\rangle\}$, which are chosen as the eigenstates of $\hat{H}$ $[\hat{H}|\alpha_n\rangle = E_n|\alpha_n\rangle]$:

$$\begin{aligned} |\Psi(t)\rangle &= \exp[-i\hat{H}t]\sum_n |\alpha_n\rangle\langle\alpha_n||\Psi(0)\rangle \\ &= \sum_n c_n \exp[-iE_nt]|\alpha_n\rangle, \end{aligned} \tag{4.20}$$

where c_n are the expansion coefficients of $|\Psi(0)\rangle$ in the chosen basis. This equation shows that the time-dependent Schrödinger equation can be directly solved in the eigenstate representation. The wave vector is a superposition of the eigenstates of the Hamiltonian, which is called "wavepecket"(WP).

Similar to the time-independent cases, discrete or continuum basis sets can be employed. The first type of basis set leads to Eq. 4.20. The second type gives a similar expression, except that the sum is replaced by an integral.

4.3.2 Split-operator method

The direct use of Eq. 4.20 is not practical for many realistic systems, due to the difficulty to obtain the eigenstates of the Hamiltonian. An alternative way to solve the time-dependent Schrödinger equation is the split-operator technique [217], which is based on the symmetric second-order disentangling of the time-evolution operator for the short-time interval Δt:

$$\hat{H} = \hat{H}_1 + \hat{H}_2, \tag{4.21}$$

$$\exp[-i\hat{H}\Delta t] = \exp\left[-i\hat{H}_1\frac{\Delta t}{2}\right]\exp\left[-i\hat{H}_2\Delta t\right]\exp\left[-i\hat{H}_1\frac{\Delta t}{2}\right]. \tag{4.22}$$

Two basis sets $\{|\alpha_i\rangle\}$ and $\{|\beta_i\rangle\}$, which are eigenstates of $\hat{H}_1$ and $\hat{H}_2$ respectively, can be chosen to evaluate the corresponding short-time propagators.

There are also several other ways to construct the approximate short-time propagators, such as the Chebysheff, Lanczos, Runge-Kutta methods, *etc.* The details of these algorithms have been described elsewhere [218–224].

4.4 Discrete variable representation

4.4.1 Definition of the discrete variable representation

The partitioning of the Hamiltonian is a common way to solve the Schrödinger equation, both in the time-dependent and time-independent pictures. One typical way to perform this partition is:

$$\hat{H} = \hat{H}_1 + \hat{H}_2(x), \tag{4.23}$$

where $\hat{H}_2$ only depends on the position operator $\hat{x}$. As discussed before, we apply two basis sets, $\{|\psi_i\rangle\}$ $[\hat{H}_1 |\psi_i\rangle = E_i^{(0)} |\psi_i\rangle]$ and $\{|x\rangle\}$ $[\hat{x} |x\rangle = x |x\rangle]$ to solve the Schrödinger equation.

The matrix representation of the Hamiltonian in the basis set $\{|\psi_i\rangle\}$ is given by:

$$\begin{aligned} \mathbf{H} &= \mathbf{E^{(1)}} + \mathbf{H^{VBR}}, && (4.24)\\ E_{ij}^{(1)} &= E_i^{(1)}\delta_{ij}, && (4.25)\\ H_{ij}^{VBR} &= \int dx \langle\psi_i|\, x\rangle \hat{H}_2(x) \langle x|\, \psi_j\rangle , \\ &= \int dx \psi_i^*(x)\hat{H}_2(x)\psi_j(x). && (4.26) \end{aligned}$$

We have to keep in mind that it is impossible to include the complete basis set of $\{|\psi_i\rangle\}$. The use of the truncated basis $\{|\psi_i\rangle\ i = 1, ...N\}$ to represent the Hamiltonian always yields energies which are upper bounds to the true eigenvalues. Thus, $\mathbf{H^{VBR}}$ is defined as the "variational basis representation" (VBR) of $\hat{H}_2$ in the truncated basis set $\{|\psi_i\rangle , i = 1, ...N\}$.

The numerical calculation of the integrals over x in the VBR requires the use of a large number of grid points. At the same time, the truncated basis set $\{|\psi_i\rangle\ i = 1, ...N\}$ does not satisfy the completeness relation and thus leads to unavoidable errors. These limitations can be mitigated by the so-called "discrete variable representation"(DVR) method [225–230].

The starting point of the DVR approach is the definition of a set of N grid points $\{|x_i\rangle\ , i = 1, ..., N\}$, which are the eigenvalues of the position operator $\hat{x}$ in the $\{|\psi_i\rangle\ i = 1, ...N\}$ representation, *i.e.*:

$$\begin{aligned} \mathbf{TXT}^+ &= \mathbf{x}, && (4.27)\\ X_{ij} &= \langle\psi_i|\, \hat{x}\, |\psi_j\rangle , && (4.28)\\ x_{ij} &= x_i\delta_{ij}, && (4.29)\\ T_{ij} &= \langle x_i|\, \psi_j\rangle . && (4.30) \end{aligned}$$

This treatment discretizes the x space, yielding a set of discrete basis functions which are localized on a set of points x_i, the so-called the DVR points. The

transformation between $\{|\psi_i\rangle\ i = 1, ...N\}$ and $\{|x_i\rangle\ , i = 1, ..., N\}$ is given by the matrix $\mathbf{T}$. Thus, the definition of the DVR requires both the N basis functions $\{|\psi_i\rangle\ i = 1, ...N\}$ and the N DVR points $\{|x_i\rangle\ , i = 1, ..., N\}$. The elements of $\mathbf{T}$, although written as $\langle x_i|\ \psi_j\rangle$, do not correspond to the value of the wavefunction $\psi_j(x)$ at the point x_i. The meaning of these elements will be discussed in the next subsection.

When the DVR points $\{|x\rangle_i\ , i = 1, ...N\}$, rather than the continuum basis $\{|x\rangle\}$, are used to represent the Hamiltonian, $\hat{H}_2$ becomes a diagonal matrix because it only contains the position operator $\hat{x}$. Thus, the matrix form of $\hat{H}_2$ in the $\{|\psi_i\rangle\ i = 1, ...N\}$ representation, the so-called "finite basis representation"(FBR), is given by:

$$\mathbf{H^{FBR}} = \mathbf{T}^{+}\mathbf{H^{DVR}}\mathbf{T}, \tag{4.31}$$

$$H_{ij}^{FBR} = \langle\psi_i|\ \hat{H}_2\ |\psi_j\rangle\ , \tag{4.32}$$

$$H_{ij}^{DVR} = H_2(x_i)\delta_{ij}. \tag{4.33}$$

These relations imply that the DVR is isomorphic with its corresponding FBR which is a good approximation of the VBR.

The DVR approach ensures that both the $\{|\psi_i\rangle\ i = 1, ...N\}$ and the $\{|x_i\rangle\ i = 1, ...N\}$ are orthonormal and complete in the truncated space. Thus even a small number of basis functions and the same number of grid points can yield an accurate result.

The DVR technique can also be used to solve the time-dependent Schrödinger equation. For example, if we divide the Hamiltonian according to Eq. 4.23, the split-operator method can be applied to perform the WP propagation. This procedure requires the evaluation of $\exp(-i\hat{H}_1\Delta t)$ in the grid representation:

$$\langle x_i|\exp(-i\hat{H}_1\Delta t)\ |x_j\rangle = \sum_k \langle x_i|\ \psi_k\rangle \exp(-iE_k\Delta t)\ \langle\psi_k|\ x_j\rangle\ , \tag{4.34}$$

and $\exp(-i\hat{H}_2\Delta t)$ in basis set representation:

$$\langle\psi_m|\exp(-i\hat{H}_2\Delta t)\ |\psi_n\rangle = \sum_i \langle\psi_m|\ x_i\rangle \exp(-iH_2(x_i)\Delta t)\ \langle x_i|\ \psi_n\rangle\ , \tag{4.35}$$

where the $\{x_i\}$ are selected as the DVR points for the basis functions $\{\psi_i\}$. The numerical evaluations of Eqs. 4.34 and 4.35 can be performed using the DVR-FBR transformation.

4.4.2 Construction of the discrete variational representation

There are two ways to obtain the DVR points.

For certain sets of basis functions, the matrix elements of the coordinate operator $\hat{x}$, *i.e.* $\mathbf{X}$, can be constructed analytically. The diagonalization of the matrix $\mathbf{X}$ can generate its eigenvalues and eigenvectors. The eigenvalues are a set of points corresponding to the DVR points and the eigenvectors define the DVR-FBR transformation matrix.

When particular functions are selected to form the basis, such as Gaussian, Legendre, Hermite polynomials, *etc.*, the DVR points are their corresponding Gaussian-quadrature points [225–227, 230]. For these basis functions with the degree N, the orthonormal relations are given exactly by the Gaussian quadrature:

$$\begin{aligned} \delta_{ij} &= \int dx \psi_i^*(x)\psi_j(x) \\ &= \sum_{k=1}^{N} \omega_k \psi_i^*(x_k)\psi_j(x_k), \end{aligned} \tag{4.36}$$

where the x_k are the Gaussian-quadrature points and the ω_k are the weights at the points x_k. The matrix element of the coordinate operator $\hat{x}$ in the $\{|\psi_i\rangle\}$ representation is also given exactly by:

$$\begin{aligned} X_{ij} &= \int dx \psi_i^*(x)\hat{x}\psi_j(x) \\ &= \sum_{k=1}^{N} \omega_k \psi_i^*(x_k)x_k\psi_j(x_k). \end{aligned} \tag{4.37}$$

The comparison of this equation with the DVR definition confirms that the DVR points are essential the Gaussian-quadrature points for these polynomials. The transformation matrix between the DVR points and the basis functions is given by:

$$T_{ij} = \sqrt{\omega_i}\psi_j(x_i). \tag{4.38}$$

The elements of the transformation matrix **T** are thus defined as the products of the values of the basis functions $\psi_j(x)$ at the Gaussian quadrature points x_i and the square root of the corresponding weights ω_i.

4.4.3 Grid representation

The Hamiltonian $\hat{H}$ consists of the kinetic-energy part $\hat{T}$ and the PE part $\hat{V}$:

$$\hat{H} = \hat{T} + \hat{V}. \tag{4.39}$$

This fact implies that two basis sets, the eigenstates of the operator $\hat{x}$ and $\hat{p}$, should be used to represent the Hamiltonian.

In the Colbert-Miller DVR method [231], the basis functions are "particle-in-a-box" eigenfunctions:

$$\psi_n(x) = \sqrt{\frac{2}{b-a}} \sin\left[\frac{n\pi(x-a)}{b-a}\right], \quad n = 1, ...N-1, \tag{4.40}$$

where the interval (a,b) is the area of the box. As expected, they are the eigenstates of the momentum operator $\hat{p}$. The DVR grid points $\{x_i\}$ for this basis set are equally spaced at:

$$x_i = a + (b-a)i/N, \quad i = 1, ...N-1. \tag{4.41}$$

Note that $\psi_n(x_0 = a) = \psi_n(x_N = b) = 0$, thus there are N-1 functions and N-1 DVR points. The matrix representation of the kinetic-energy operator in the DVR points is given by:

$$T_{ij} = \begin{cases} \frac{1}{2m}\frac{(-1)^{i-j}}{(b-a)^2}\frac{\pi^2}{2}\left\{\frac{1}{\sin^2[\pi(i-j)/(2N)]} - \frac{1}{\sin^2[\pi(i+j)/(2N)]}\right\} & (i \neq j), \\ \frac{1}{2m}\frac{1}{(b-a)^2}\frac{\pi^2}{2}\left\{\frac{2N^2+1}{3} - \frac{1}{\sin^2[\pi i/N]}\right\} & (i = j). \end{cases} \tag{4.42}$$

In the time-dependent picture, the Colbert-Miller DVR can be used to evaluate the transformation between $|x\rangle$ and $|p\rangle$. Alternatively, this transformation can be performed by the Fourier-transformation method [221,223]. This approach also takes the eigenstates of the momentum operator p as the basis functions and applies a set of equally-spaced points in the coordinate space. However, instead of real functions of x, complex plane-wave basis functions are chosen in this case.

The Fourier-transformation method discretizes the position and momentum space simultaneously. This is equivalent to the division of phase space into many small rectangular regions. The volume of the sampling region in phase space is

$$\mathcal{V} = P \cdot X, \tag{4.43}$$

$$X = N_g \triangle x, \tag{4.44}$$

$$P = N_g \triangle p, \tag{4.45}$$

where X and P are the sampling lengths in the coordinate and the momentum spaces, respectively. $\triangle x$ and $\triangle p$ are sampling spacings in the corresponding spaces. Note the number of the points (N_g) in both of two spaces should be same. At the same time, the volume in phase space is also determined by:

$$\mathcal{V} = N_g 2\pi. \tag{4.46}$$

Therefore, the discretization of the grid and momentum spaces should satisfy:

$$N_g \triangle x \triangle p = 2\pi. \tag{4.47}$$

Thus, the spacing $\triangle x$, as well as the range X, in coordinate space automatically determine the resolution $\triangle p$ and the area P in momentum space.

The Colbert-Miller DVR and the Fourier method are essentially same, because both of them apply a set of basis functions which are eigenstates of the momentum operator. They differ in the choice of the boundary conditions of the basis functions. The Fourier method is not convenient for the time-independent calculations, because the Hamiltonian matrix in the Fourier basis functions (e^{ipx}) is not a real-valued matrix. It is very suitable, on the other hand, for time-dependent calculations due to the highly efficient fast-Fourier-transformation (FFT) algorithm. The scaling of the computational effort of this FFT algorithm is $\mathcal{O}(N_g \log N_g)$ for N_g grid points.

4.5 Photo-induced quantum dynamics via conical intersections

The description of the photoinduced dynamics involves (i) the initial preparation of the system by photoexcitation and (ii) the time-evolution of the wavefunctions.

To define the initial preparation of the system, we first generate the vibrational eigenstates of the electronic ground-state PE surfaces with time-dependent or time-independent methods. The initial WP is then prepared by vertical excitation of a vibrational level in the electronic ground state to the excited electronic state.

The nuclear WP is propagated on coupled surfaces by solving the time-dependent Schröndinger equation. The diabatic representation is used to propagate the WP. Finally, the WP is transformed to the adiabatic representation, which is more suitable for the quantitative interpretation of the photochemical dynamics.

4.5.1 Representation of wave vector

The state vector $\Psi(t)$ is expanded in a complete orthogonal set of time-independent basis functions. This basis set is constructed as the direct product of the diabatic electronic basis $\{|\Phi_n\rangle\}$ and suitable discrete basis $\{|\chi_{\nu i}\rangle\}$ for each nuclear degree of freedom:

$$|\Psi(t)\rangle = \sum_n \sum_{\nu 1,\nu 2...} C_{n,\nu 1,\nu 2}(t) \, |\Phi_n\rangle \, |\chi_{\nu 1}\rangle \, |\chi_{\nu 2}\rangle \, ..., \tag{4.48}$$

where $C_{n,\nu 1,\nu 2}(t)$ is the nuclear WP in the nth diabatic electronic state:

$$\begin{aligned} \chi_{n,\nu 1,\nu 2...}(t) &= C_{n,\nu 1,\nu 2}(t) \\ &= \langle \Phi_n | \, \langle \chi_{\nu 1} | \, \langle \chi_{\nu 2} | \, ... \, | \Psi(t) \rangle \, . \end{aligned} \tag{4.49}$$

A similar relation is obtained in a set of continuum basis states, *e.g.*:

$$|\Psi(t)\rangle = \sum_n \int dR_1 dR_2 ... C_n(t, R_1, R_2 ...) \, |\Phi_n\rangle \, |R_1\rangle \, |R_2\rangle \, ..., \tag{4.50}$$

where $C_n(t, R_1, R_2...)$ is the nuclear WP in the grid representation in the nth diabatic electronic state:

$$\begin{aligned} \chi_n(t, R_1, R_2...) &= C_n(t, R_1, R_2...) \\ &= \langle \Phi_n | \langle R_1 | \langle R_2 | ... | \Psi(t) \rangle . \end{aligned} \tag{4.51}$$

Alternatively, the state vector can also be expanded in a mixed basis of discrete states and coordinate grids, called the "mix-grid-basis-representation" (MGBR). This means that the WP is evaluated in the grid representation for some degrees of freedom and expanded in a discrete basis for the other degrees of freedom:

$$\begin{aligned} |\Psi(t)\rangle = \quad & \sum_n \int dR_1 dR_2 ... dR_k \sum_{\nu(k+1),\nu(k+2)...} C_{n,\nu(k+1),\nu(k+2)...}(t, R_1, R_2, ..., R_k) \\ & |\Phi_n\rangle |R_1\rangle |R_2\rangle .... |R_k\rangle |\nu(k+1)\rangle |\nu(k+2)\rangle ... \end{aligned} \tag{4.52}$$

The nuclear WP in the nth diabatic electronic state in this MGBR is:

$$\begin{aligned} & \chi_{n,\nu(k+1),\nu(k+2)...}(t, R_1, R_2, ...R_k) \\ = \quad & C_{n,\nu(k+1),\nu(k+2)...}(t, R_1, R_2, ..., R_k) \\ = \quad & \langle \Phi_n | \langle R_1 | \langle R_2 | ... \langle R_k | \langle \nu(k+1) | \langle \nu(k+2) | ... | \Psi(t) \rangle . \end{aligned} \tag{4.53}$$

Both expansions convert the time-dependent Schrödinger equation into a set of coupled first-order differential equations:

$$i\dot{\mathbf{C}}(\mathbf{t}) = \mathbf{HC}(t), \tag{4.54}$$

where $\mathbf{H}$ is the matrix representation of the Hamiltonian. This equation can be solved by the methods discussed earlier in this chapter.

4.5.2 Construction of the adiabatic-to-diabatic transformation

As discussed in Chapter 2, the adiabatic-to-diabatic transformation matrix $\mathbf{U}$ is a function of the nuclear geometry $\mathbf{R}$ (see Chapter 2):

$$\left|\Phi_n^d\right\rangle = \sum_i |\Phi_i^a\rangle \, \mathbf{U}_{in}(R_1, R_2, R_3...). \tag{4.55}$$

This equation defines the transformation of the nuclear WP between these two representations. In the grid representation, the evaluation of this transformation is straightforward. Otherwise, one needs to evaluate the matrix **U** in the direct-product basis representation or MGBR, *e.g.*:

$$\begin{aligned} & \langle \nu 1| \langle \nu 2| \mathbf{U} |\nu 2'\rangle |\nu 1'\rangle \\ = & \int dR_1 \int dR_2 \langle \nu 1| R_1\rangle \langle \nu 2| R_2\rangle \mathbf{U}(R_1, R_2) \langle R_2| \nu 2'\rangle \langle R_1| \nu 1'\rangle . \end{aligned} \quad (4.56)$$

The integrals can be evaluated by using the DVR-FBR technique.

4.5.3 Vibrational eigenfunctions of the electronic ground state

The Hamiltonian for the nuclear motion in the electronic ground state is:

$$\hat{H}_g = \hat{T} + \hat{V}_1^a, \quad (4.57)$$

where $\hat{V}_1^a$ is the adiabatic PE function of the ground electronic state.

In the time-independent approach, we use the standard method described in Section 4.2 to obtain the eigenstates of the Hamiltonian. A orthogonal basis set is constructed by the direct product of the suitable basis functions for different degrees of freedom (see Subsection 4.5.1). The matrix representation of the Hamiltonian in this basis set is obtained with the DVR technique. The diagonalization of this matrix gives the vibrational eigenenergies and eigenstates of the ground electronic state.

In the time-dependent picture, the vibrational levels of the ground-state surface are determined by the so-called pseudo-spectral method described in Ref. [232]. A suitable Gaussian wavefunction is chosen as initial condition and is propagated on the adiabatic PE surface of the electronic ground state. The propagation of the WP is performed by the split-operator method discussed in Section 4.3. In the grid representation, we apply Fourier transformation to evaluate the propagator associated with the kinetic operator. For the other basis functions, the DVR technique is used to evaluate the transformation between the basis functions and the DVR grid points.

The propagation of the wavefunction gives us the time-dependent autocorrelation function

$$C(t) = \langle \chi(t_0) |\, \chi(t) \rangle \,. \tag{4.58}$$

The pseudospectral intensity is given by:

$$I(E) = \int_0^\infty C(t) e^{iEt/\hbar} dt. \tag{4.59}$$

The positions of the peak maxima in the spectrum are the eigenenergies of the bound states. The corresponding eigenfunctions are calculated by filtering the desired eigenstate with energy E_n,

$$\chi_n(E) = \int_0^\infty \chi(t) e^{iE_n t/\hbar} dt. \tag{4.60}$$

In order to improve the energy resolution, we use the relation [233]:

$$C(2t) = \langle \chi^*(t) | \chi(t) \rangle. \tag{4.61}$$

This way, one gains a factor of 2 in the energy resolution of the spectrum.

4.5.4 Preparation of initial states

The initial WP for the excited-state propagation is obtained by vertical excitation of the vibrational states $\chi^a_{1,(k)}$ of the electronic ground state to the adiabatic excited state. For a particular $\chi^a_{1,(k)}$, the ground-state wavefunction in the adiabatic representation can be written as

$$|\mathbf{\Psi}_0\rangle = \chi^a_{1,(k)} \, |\Phi^a_1\rangle \,. \tag{4.62}$$

Here, the vibrational eigenstates of the ground electronic state are generated in the adiabatic representation, while the diabatic representation is much more suitable for the WP propagation. Therefore, we employ the unitary transformation matrix $\mathbf{U}$ to obtain $|\mathbf{\Psi}_0\rangle$ in the diabatic representation:

$$|\mathbf{\Psi}_0\rangle = \sum_i \chi^d_i \left|\Phi^d_i\right\rangle \tag{4.63}$$

via the method described in Subsection 4.5.2. The vertical excitation of $|\mathbf{\Psi}_0\rangle$ to to the excited state provides the initial wave packet $|\mathbf{\Psi}(t=0)\rangle$.

4.5.5 Quantum dynamics for coupled electronic states

The coupled equations for the nuclear motion in the diabatic basis are:

$$i\frac{\partial}{\partial t}\chi^{\mathbf{d}}(t) = (\mathbf{T} + \mathbf{V}^{\mathbf{d}}(\mathbf{R}))\chi^{\mathbf{d}}(t), \tag{4.64}$$

where $\chi^{\mathbf{d}}(t)$ is a column vector and its elements correspond to the nuclear WP in different electronic states. $\mathbf{T}$ is the kinetic-energy matrix. $\mathbf{V}^{\mathbf{d}}$ is the diabatic potential matrix. The diagonal elements of $\mathbf{V}^{\mathbf{d}}$ denote the diabatic PE functions, while the off-diagonal elements are potential couplings between diabatic states.

The short-time propagator is expressed as:

$$\exp[-i\mathbf{H}\Delta t] = \exp\left[-i\mathbf{T}\frac{\Delta t}{2}\right]\exp\left[-i\mathbf{V}^{\mathbf{d}}(\mathbf{R})\Delta t\right]\exp\left[-i\mathbf{T}\frac{\Delta t}{2}\right]. \tag{4.65}$$

The propagator related to the kinetic part is evaluated by the Fourier-transformation method. The propagator related to the potential part is given by,

$$\exp\left[-i\mathbf{V}^{\mathbf{d}}(\mathbf{R})\Delta t\right] = \mathbf{U}^{+}(\mathbf{R})\mathbf{\Gamma}(\mathbf{R})\mathbf{U}(\mathbf{R}), \tag{4.66}$$

$$\mathbf{\Gamma}(\mathbf{R})_{jk} = \delta_{jk}\exp(-iV_j^a(R)), \tag{4.67}$$

where $\mathbf{U}$ is the adiabatic-to-diabatic transformation matrix.

4.5.6 Absorbing potential

If the WP is propagated in the grid representation, it is necessary to eliminate spurious events which are generated by the boundaries of the numerical grid. These events arise because the numerical mesh only covers a finite region of space and the Fourier-transformation method implies periodic boundary condition. In the treatment of dissociating systems, we thus observe the reflection of the WP from the boundaries of the finite grid. Since these boundary effects are not real physical events, they have to be eliminated by suitable measures.

One possible way to get rid of these boundary effects is to apply a so-called "absorbing potential" near the end of the grid mesh [234, 235]. If the grid mesh extends from R_{min} to R_{max} in the coordinate R_1 and the potential energy is $V_0(R_1)$, we add a negative imaginary potential V_1 into V_0:

$$V(R_1) = V_0(R_1) + V_1(R_1), \tag{4.68}$$

where $V_1(R_1)$ is chosen as a smooth function of R_1 and is localized in the vicinity of the boundary R_{max} (or R_{min}), *e.g.*

$$V_1(R_1) = \begin{cases} -i\xi(R_1 - R_a)^n & (R_a \leq x < R_{max}), \\ 0 & (R_{min} < x < R_a), \end{cases} \tag{4.69}$$

where n is an integer and R_a is the point that initializes the absorbing potential. The choice of V_1 is based on three criteria: it should be large enough to remove the spurious reflections of the WP; it should be localized close to the boundary, and it should be a slowly-varying function of R. However, for most simulations of chemical dynamics, the selection of the absorbing potential is not unique and its average magnitude can vary considerably [235].

An alternative way to remove the boundary problem is to multiply the WP by a damping function [236],

$$f(R_1) = \sin\left[\frac{\pi}{2}\frac{R_{max} - R_1}{R_{max} - R_a}\right], \quad R_{max} \geq R_1 \geq R_a \tag{4.70}$$

which is activated near the grid edge. R_a is the point where the damping function is initiated and $\Delta R_a = R_m - R_a$ is the width over which the function decays from 1 to 0.

4.5.7 Physical observables

4.5.7.1 Flux operator

The quantum flux operator $\hat{F}$ measures the probability of the current density penetrating a dividing surface. This dividing surface Θ is placed at R_f to separate the reactants and the products:

$$\hat{F} = i[\hat{H}, \hat{\Theta}], \tag{4.71}$$

$$\hat{\Theta} = h(R - R_f), \quad = \begin{cases} 0 & R < R_f \\ 1 & R > R_f \end{cases} \tag{4.72}$$

where h is a Heaviside step function of the coordinate R. Since $\hat{\Theta}$ is a function of R, the potential operator part commutes with it. If we assume that the kinetic-energy operator is $\hat{T} = -\frac{1}{2m}\frac{\partial^2}{\partial R^2}$, the flux operator can be expressed as [237]:

$$\begin{aligned} \hat{F} &= i[\hat{T}, \hat{\Theta}] \\ &= \frac{-i}{2m}[\frac{\partial}{\partial R}\delta(R - R_f) + \delta(R - R_f)\frac{\partial}{\partial R}]. \end{aligned} \tag{4.73}$$

If the reaction coordinate is R_1 (one of the tuning coordinates), the reaction probability in the ith electronic state is defined as the time-accumulated flux through a divided surface at R_1=R_f in the asymptotic region:

$$\begin{aligned} F_i^D(t) &= \int dt \, \langle \chi_i(R_1, R_2, ..., t)| \, \hat{F} \, |\chi_i(R_1, R_2, ..., t)\rangle \Big|_{R_1=R_f} \\ &= \int dt Im \left[\left\langle \chi_i(R_1, R_2, ..., t) \, | \, \frac{\partial \chi_i(R_1, R_2, ..., t)}{\partial R_1} \right\rangle \Big|_{R_1=R_f} \right]. \end{aligned} \tag{4.74}$$

Note the bra-ket product implies the integral over the other coordinates, while R_1=R_f.

For a dissociative system, the dissociation probability in a particular channel can be measured by the quantum flux. The flux has to be determined in the dissociation limit ($R_f = R_d$) to avoid the contamination by inter-state couplings and finite-grid effects.

4.5.7.2 Electronic population probability

The quantity of primary interest in the dynamics at conical intersections is the time-dependent electronic population probability.

The diabatic population is defined as the expectation value of the projector $\left|\Phi_i^d\right\rangle \left\langle\Phi_i^d\right|$ with the time-dependent wave function:

$$P_i^d(t) = \langle \Psi(t)| \, \Phi_i^d \rangle \left\langle \Phi_i^d \right| \, \Psi(t) \rangle \, . \tag{4.75}$$

This expression is equivalent to integral of the probability density over all nuclear degrees of freedom:

$$P_i^d(t) = \int dR_1 \int dR_2 ... |\chi_i^d(t, R_1, R_2, ...)|^2. \tag{4.76}$$

The diabatic population can also be calculated in the product-basis representation:

$$P_i^d(t) = \sum_{\nu 1}\sum_{\nu 2}...|\chi^d_{i,\nu_1,\nu_2,...}(t)|^2, \tag{4.77}$$

or in the MGBR representation:

$$P_i^d(t) = \int dR_1 \int dR_2 ... \int dR_k \sum_{\nu(k+1)}\sum_{\nu(k+2)}... \\ |\chi^d_{i,\nu(k+1),\nu(k+2),...}(t,R_1,R_2,...R_k)|^2. \tag{4.78}$$

The adiabatic population is defined as the expectation value of the projector $|\Phi_i^a\rangle\langle\Phi_i^a|$:

$$P_i^a(t) = \langle\Psi(t)|\,\Phi_i^a\rangle\langle\Phi_i^a|\,\Psi(t)\rangle\,. \tag{4.79}$$

As discussed in Subsection 4.5.2, the diabatic-to-adiabatic transformation can be performed in the grid representation, the basis set representation, or the MGBR. The resulting adiabatic nuclear WP finally gives the adiabatic population, e.g. in the grid representation:

$$P_i^a(t) = \int dR_1 \int dR_2 ... |\chi_i^a(t,R_1,R_2,...)|^2. \tag{4.80}$$

Let us consider a system with a single dissociative coordinate R_1 and many non-dissociative coordinates $\{R_i, i = 2, ...N\}$. To avoid the need of a large grid mesh for R_1, a trick is employed to calculate the adiabatic and diabatic electronic population probabilities as follows: the time-accumulated dissociative flux is measured at R_d, in the asymptotic region of the potential surface; then the diabatic electronic population probability is the sum of this flux and the probability of the nuclear WP remaining in the region $[0, R_d]$:

$$P_i^d(t) = \int_0^{R_D} dR_1 \int dR_2 \int dR_3\,|\psi_i^d(t,R_1,R_2,R_3...)|^2 + F_i^D(t). \tag{4.81}$$

This expression if correct, because neither reflections nor nonadiabatic transitions take place in the asymptotic region. To estimate the adiabatic population, we use the corresponding expression:

$$P_i^a(t) = \int_0^{R_D} dR_1 \int dR_2 \int dR_3\,|\psi_i^a(t,R_1,R_2,R_3...)|^2 + F_i^D(t). \tag{4.82}$$

4.5.7.3 Probability density

For one-dimensional or two-dimensional models, it is straightforward to show the probability density of the nuclear WP in the ith diabatic (or adiabatic) electronic state, ϱ_i^d (or ϱ_i^a). The probability density is the absolute square of the nuclear WP in the ith diabatic (or adiabatic) state, *i.e.*:

$$\varrho_i^d(t, R_1, R_2) = |\chi_i^d(t, R_1, R_2)|^2, \tag{4.83}$$

$$\varrho_i^a(t, R_1, R_2) = |\chi_i^a(t, R_1, R_2)|^2. \tag{4.84}$$

To view the WP motion for a multi-dimensional system, we define reduced (or compact) probability densities for one or two modes by the integral of the absolute square of the nuclear WP over the remaining vibrational degrees of freedom, *i.e.*:

$$\varrho_i^d(t, R_1, R_2) = \int dR_3 \int dR_4 ... |\chi_i^d(t, R_1, R_2, R_3, R_4 ...)|^2, \tag{4.85}$$

$$\varrho_i^a(t, R_1, R_2) = \int dR_3 \int dR_4 ... |\chi_i^a(t, R_1, R_2, R_3, R_4 ...)|^2. \tag{4.86}$$

It should be kept in mind that the reduced probability densities are not true WPs.

Chapter 5

Quantum dissipative dynamics

5.1 Density operator

5.1.1 Definition of density operator

If a system can be described by a wave vector $|\psi\rangle$ in Hilbert space, it is in a "pure"state. In this case, the density operator is given by:

$$\hat{\rho}_{pure} = |\psi\rangle \langle\psi| , \tag{5.1}$$

with the normalization condition $\langle\psi| \psi\rangle = 1$.

If a system cannot be described by a single state vector, but by an ensemble of quantum states, it is in a "mixed state". If the probability to observe the wave vector $|\psi_\varphi\rangle$ is w_φ, the density operator for the mixed state is defined as

$$\hat{\rho}_{mixed} = \sum_\varphi w_\varphi |\psi_\varphi\rangle \langle\psi_\varphi| , \tag{5.2}$$

$$\sum_\varphi w_\varphi = 1,\ w_\varphi \leq 1. \tag{5.3}$$

5.1.1.1 Density matrix

In a set of complete orthonormal basis states $\{|\phi_i\rangle\}$, the density operator is written as

$$\hat{\rho} = \sum_{i,j} \rho_{ij} |\phi_i\rangle \langle\phi_j| \tag{5.4}$$

where $\rho_{ij} = \langle\phi_i|\,\hat{\rho}\,|\phi_j\rangle$ are the elements of the "density matrix", which is the matrix representation of the density operator. This density matrix is Hermitian, *i.e*:

$$\rho_{ij} = \rho^*_{ji}. \tag{5.5}$$

According to the definition of the density matrix,

$$\mathrm{tr}\left\{\rho_{pure}\right\} = \sum_i \rho_{ii} = 1. \tag{5.6}$$

The difference between a pure state and a mixed state is indicated by the trace of $\hat{\rho}^2$:

$$\mathrm{tr}\left\{\hat{\rho}^2_{pure}\right\} = 1, \tag{5.7}$$

$$\mathrm{tr}\left\{\hat{\rho}^2_{m}\right\} < 1. \tag{5.8}$$

The density operator completely characterizes a system. The expectation value of a physical observable is given by

$$\langle\hat{A}\rangle = \mathrm{tr}\left\{\hat{A}\hat{\rho}\right\}. \tag{5.9}$$

The physical meaning of the density operator is reflected by the following equation:

$$\rho_{ij} = \mathrm{tr}\left\{\hat{\rho}\,|\phi_j\rangle\,\langle\phi_i|\right\}. \tag{5.10}$$

The diagonal elements ρ_{ii} are the probabilities of the system in the states $|\phi_i\rangle$. The off-diagonal elements ρ_{ij} describe the coherence of $|\phi_i\rangle$ and $|\phi_j\rangle$.

In the grid representation, density matrix is defined as

$$\rho(x, x') = \langle x|\,\hat{\rho}\,|x'\rangle. \tag{5.11}$$

The diagonal elements $\rho(x, x)$ represent the probability density of the system as a function of the coordinate x.

5.1.2 Liouville Von Neumann equation

The equation of motion for the density operator (*i.e.*, the quantum master equation) is given by the Liouville-von Neumann equation:

$$\dot{\hat{\rho}}(t) = -i[\hat{H}, \hat{\rho}(t)], \tag{5.12}$$

where $\hat{H}$ is the Hamiltonian. This equation can be expressed in a more compact form:

$$\dot{\hat{\rho}}(t) = -i\hat{L}\hat{\rho}(t), \tag{5.13}$$

where the Liouville superoperator $\hat{L}$ is the abbreviation of the commutator $[\hat{H}, \bullet]$.

If $\hat{H}$ is independent of time t, the solution of quantum master equation is:

$$\begin{aligned} \hat{\rho}(t) &= \exp[-i\hat{L}(t-t_0)]\hat{\rho}(t_0) \\ &= \hat{U}(t-t_0)\hat{\rho}(t_0)\hat{U}^{+}(t-t_0). \end{aligned} \tag{5.14}$$

5.2 Reduced density operator

5.2.1 Open quantum systems

In the treatment of complex many-body systems, it is often impossible to take all degrees of freedom into account. However, in most cases, we are only interested in a rather small part of the total system. Thus, we can define this small relevant part as an open system and treat the large residual part as an environment. The dynamics of the open system is governed by the system Hamiltonian, as well as the system-environment coupling. If the environment is large enough such that the effect of the system on the environment can be neglected, it is reasonable to treat the environment as a reservoir, which is in thermal equilibrium with a fixed temperature. These assumptions result in the "system-plus-reservoir" model for the exploration of the dissipative dynamics of the open system.

The whole Hamiltonian is divided into three parts, a system part $\hat{H}_s$, a reservoir (or bath) part $\hat{H}_b$ and the system-reservoir interaction $\hat{H}_{sb}$

$$\hat{H} = \hat{H}_s + \hat{H}_b + \hat{H}_{sb}. \tag{5.15}$$

Here we define the "reduced density operator" by tracing the total density operator over the bath coordinates, *i.e.*:

$$\hat{\rho}_s = \mathrm{tr}_b\{\hat{\rho}\}. \tag{5.16}$$

Since the measurement of a physical observable of the system is fully determined by

$$\langle A \rangle = \mathrm{tr}_s\{\hat{A}\hat{\rho}_s\}, \tag{5.17}$$

the dissipative dynamics of the system is completely characterized by this reduced density operator.

The equation of motion for the reduced density operator can be obtained by different methods, such as perturbative approaches [238, 239, 239–241], path integral approaches [240], stochastic approaches [239–242], phenomenological semigroup approaches [243–246] *etc.* In this thesis, we combine the projection operator technique and perturbation theory to obtain the equation of motion for the reduced density operator.

5.2.2 Projection-operator method

As discussed in the preceding section, the Liouville-von Neumann equation describes the motion of the total density operator according to Eq. 5.12 with the Liouville operator $\hat{L} = \hat{L}_s + \hat{L}_b + \hat{L}_{sb}$. All Liouville operators are assumed to be time-independent in the Schrödinger picture.

The equation of motion for the reduced density operator $\hat{\rho}_s$ can be formally obtained by the projection technique proposed by Nakajima and Zwanzig [239–241, 247, 248]. Let us consider an operator $\hat{P}$, which projects the total density operator $\hat{\rho}(t)$ onto the direct product of $\hat{\rho}_s(t)$ and $\hat{\rho}_b$:

$$\hat{P}\hat{\rho}(t) = \hat{\rho}_b\hat{\rho}_s(t), \tag{5.18}$$

where $\hat{\rho}_b$, the density operator of the bath, is defined as:

$$\hat{\rho}_b = \frac{\exp(-\hat{H}_b/(kT))}{\mathrm{tr}\left\{\exp(-\hat{H}_b)/(kT)\right\}}, \tag{5.19}$$

describing the reservoir in equilibrium of temperature T. We furthermore define:

$$\hat{Q} = 1 - \hat{P}. \tag{5.20}$$

Since both $\hat{P}$ and $\hat{Q}$ are time-independent linear operators, the Liouville-von Neumann equation can be written as a pair of coupled equations:

$$\frac{\partial}{\partial t}\hat{P}\hat{\rho}(t) = -i\hat{P}\hat{L}(\hat{P}\hat{\rho}(t) + \hat{Q}\hat{\rho}(t)), \tag{5.21}$$

$$\frac{\partial}{\partial t}\hat{Q}\hat{\rho}(t) = -i\hat{Q}\hat{L}(\hat{P}\hat{\rho}(t) + \hat{Q}\hat{\rho}(t)). \tag{5.22}$$

The solution of Eq. 5.22 is:

$$\begin{aligned}\hat{Q}\hat{\rho}(t) = \quad & \exp[-i\hat{Q}\hat{L}(t)]\hat{Q}\hat{\rho}(0) \\ & -i\int_0^t d\tau \exp[-i\hat{Q}\hat{L}(t-\tau)]\hat{Q}\hat{L}\hat{P}\hat{\rho}(\tau).\end{aligned} \tag{5.23}$$

By inserting Eq. 5.23 into Eq. 5.21, a closed equation for $\hat{P}\hat{\rho}(t)$ is obtained:

$$\begin{aligned}\frac{\partial}{\partial t}\hat{P}\hat{\rho}(t) = \quad & -i\hat{P}\hat{L}\hat{P}\hat{\rho}(t) \\ & -i\hat{P}\hat{L}\exp[-i(1-\hat{P})\hat{L}t](1-\hat{P})\rho(0) \\ & -\int_0^t d\tau \hat{P}\hat{L}\exp[-i(1-\hat{P})\hat{L}\tau](1-\hat{P})\hat{L}\hat{P}\hat{\rho}(t-\tau).\end{aligned} \tag{5.24}$$

This generalized master equation is an inhomogeneous integro-differential equation in time, which completely describes the quantum dissipative dynamics of the open system under the influence of the reservoir. It is formally exact. Note that the inhomogeneous term depends on the initial value of $(1-\hat{P})\rho(0)$. with the factorized initial condition, $\hat{\rho}(0) = \hat{\rho}_b\hat{\rho}_s(0)$, the quantum master equation becomes homogeneous:

$$\begin{aligned}\frac{\partial}{\partial t}\hat{P}\hat{\rho}(t) = \quad & -i\hat{P}(\hat{L}_s + \hat{L}_{sb})\hat{\rho}(t) \\ & -\int_0^t d\tau \hat{P}\hat{L}_{sb}\exp[-i(1-\hat{P})\hat{L}\tau](1-\hat{P})\hat{L}_{sb}\hat{P}\hat{\rho}(t-\tau).\end{aligned} \tag{5.25}$$

Here, the first term describes the reversible motion while the second term gives rise to irreversibility. However, this equation is still too complicated. The kernel contains any power of $\hat{L}_{sb}$ and the system dynamics depends on the whole history of the density operator.

In the weak coupling case, the kernel in Eq. 5.25 can be expanded to the second order of $\hat{L}_{sb}$ within the Born approximation. We introduce the additional assumption that the relaxation of the bath takes place on much shorter timescales than the system dynamics. Neglecting the memory effects of the bath by using the Markov approximation

$$\rho_s(t-\tau) = \exp(i\hat{L}_s\tau)\rho(t), \tag{5.26}$$

one arrives at the Born-Markov approximation for the master equation:

$$\begin{aligned}\frac{\partial}{\partial t}\hat{P}\hat{\rho}(t) = \quad & -i\hat{P}(\hat{L}_s+\hat{L}_{sb})\hat{\rho}(t) \\ & -\int_0^t d\tau \hat{P}\hat{L}_{sb}\exp[-i(1-\hat{P})(\hat{L}_s+\hat{L}_b)\tau](1-\hat{P})\hat{L}_{sb}\hat{P}\hat{\rho}(t).\end{aligned} \tag{5.27}$$

Extending the integral to ∞, the final equation of motion for the reduced density operator is written as:

$$\begin{aligned}\frac{\partial}{\partial t}\rho_s(t) = \quad & -i\left[\hat{H}_s, \rho_s(t)\right] \\ & -i\,\mathrm{tr}_b\left\{\left[\hat{H}_{sb}, \rho_s(t)\rho_b\right]\right\} \\ & -\int_0^\infty d\tau\,\mathrm{tr}_b\left\{\left[\hat{H}_{sb}, (1-\hat{P})\left[\hat{H}_{sb}^{(I)}(-\tau), \rho_s(t)\rho_b\right]\right]\right\},\end{aligned} \tag{5.28}$$

with

$$\hat{H}_{sb}^{(I)}(-\tau) = \exp\left\{-i(\hat{H}_s+\hat{H}_b)\tau\right\}\hat{H}_{sb}\exp\left\{i(\hat{H}_s+\hat{H}_b)\tau\right\}. \tag{5.29}$$

Eq. 5.28 is also called "Redfield equation" [249].

5.2.3 System-bath interaction

We assume that the system-bath interaction Hamiltonian $\hat{H}_{sb}$ can be written as a sum of products of system operators $\hat{K}_i$ and reservoir operators $\hat{F}_i$

$$\hat{H}_{sb} = \sum_i \hat{K}_i\hat{F}_i. \tag{5.30}$$

Inserting Eq. 5.30 into the Redfield equation (Eq. 5.28), one arrives at the following equation

$$\begin{aligned}\frac{\partial}{\partial t}\rho_s(t) = \quad & -i[\hat{H}_s, \rho_s(t)] - i\sum_m \langle \hat{F}_m \rangle [\hat{K}_m, \hat{\rho}_s(t)] \\ & -\sum_{m,n}\int_0^\infty d\tau \\ & (C_{mn}(\tau)[\hat{K}_m, \hat{K}_n^{(I)}(-\tau)\hat{\rho}_s(t)] \\ & -C_{nm}(-\tau)[\hat{K}_m, \hat{\rho}_s(t)\hat{K}_n^{(I)}(-\tau)]) , \end{aligned} \tag{5.31}$$

where $\langle \hat{F}_m \rangle$ is the thermal average of the bath operator $\hat{F}_m$

$$\langle \hat{F}_m \rangle = \mathrm{tr}_b\{\hat{F}_m \hat{\rho}_b\}, \tag{5.32}$$

and $C_{mn}(\tau)$ is the so-called "bath correlation function"

$$C_{mn}(\tau) = \mathrm{tr}_b\{\hat{F}_m^{(I)}(\tau)\hat{F}_n^{(I)}(0)\rho_b\} - \langle \hat{F}_m \rangle \langle \hat{F}_n \rangle. \tag{5.33}$$

The above equations contain the system and bath operators in the interaction picture:

$$\hat{K}_m^{(I)}(\tau) = \exp(i\hat{H}_s\tau)\hat{K}_m \exp(-i\hat{H}_s\tau), \tag{5.34}$$

$$\hat{F}_m^{(I)}(\tau) = \exp(i\hat{H}_b\tau)\hat{F}_m \exp(-i\hat{H}_b\tau). \tag{5.35}$$

The first term in Eq. 5.31 describes the reversible dynamics governed by the system Hamiltonian. The expectation values of the bath operators appearing in the second term describe the mean-field contributions of the bath to the system dynamics. This term does not induce the dissipation of the system. In the third term, the irreversible relaxation of the system is caused by the fluctuations of the bath around the mean-field energies, which are characterized by the bath correlation function $C_{mn}(\tau)$. The properties of the bath correlation functions are discussed in Appendix B.

5.2.4 Harmonic-oscillator reservoir

The explicit calculation of the quantum correlation functions of the bath is not feasible, because it is impossible to calculate all quantum states of a general

macroscopic reservoir. To overcome this difficulty, several models have been proposed to describe the bath and the system-bath interaction.

For many kinds of reservoirs, such as radiation field, crystal lattice, *etc.* we introduce normal modes to describe the microscopic motion of the reservoir. The environment is thus modelled by a collection of many independent harmonic oscillators:

$$\hat{H}_b = \sum_q \frac{\omega_q}{2}(\hat{p}_q^2 + \hat{q}_q^2), \tag{5.36}$$

where $\hat{q}_q$ and $\hat{p}_q$ are dimensionless coordinate and momentum operators, respectively, for the particular mode with the frequency ω_q.

For weak coupling, we employ a Taylor expansion of the system-bath interaction Hamiltonian $\hat{H}_{sb}$ with respect to the reservoir coordinates and keep the linear term only

$$\hat{H}_{sb} = \hat{K}\sum_q g_q \hat{q}_q. \tag{5.37}$$

where g_q is the coupling strength. In the following discussion, only one system operator $\hat{K}$ is considered for convenience.

The harmonic-oscillator bath is homogeneous, therefore the expectation values of all $\hat{q}_q$ vanish

$$\langle \hat{q}_q \rangle = 0. \tag{5.38}$$

Thus, the mean-field term in Eq. 5.31 does not exist for the harmonic-oscillator bath.

For the harmonic-oscillator bath, the correlation functions in the time domain take the form:

$$\begin{aligned} C(\tau) &= \mathrm{tr}_b\left\{\hat{q}_q^{(I)}(\tau)\hat{q}_q^{(I)}(0)\hat{\rho}_b\right\} \\ &= \frac{1}{2}\sum_q g_q^2[e^{-i\omega_q\tau} + 2n(\omega_q)\cos(\omega_q\tau)], \end{aligned} \tag{5.39}$$

$$\begin{aligned} C^*(\tau) = C(-\tau) &= \mathrm{tr}_b\left\{\hat{q}_q^{(I)}(-\tau)\hat{q}_q^{(I)}(0)\hat{\rho}_b\right\} \\ &= \frac{1}{2}\sum_q g_q^2[e^{i\omega_q\tau} + 2n(\omega_q)\cos(\omega_q\tau)], \end{aligned} \tag{5.40}$$

where $n(\omega_q)$ is the occupation number for the particular Harmonic oscillator mode with frequency ω_q. This occupation number is determined by the Bose-Einstein distribution at the temperature T

$$n(\omega_q) = \frac{1}{\exp(-\frac{\hbar\omega_q}{k_B T}) - 1} \tag{5.41}$$

with the Bolzmann constant k_B.

5.2.5 Spectral density

To simplify the description of the bath, we introduce the spectral density

$$J(\omega) = \frac{\pi}{2} \sum_q g_q^2 \delta(\omega - \omega_q). \tag{5.42}$$

Any macroscopic system should have a continuous spectral density due to the infinite number of harmonic oscillators. Therefore Eq. 5.39 is written as:

$$C(\tau) = \int_0^\infty d\omega \, \frac{1}{\pi} J(\omega)[e^{-i\omega\tau} + 2n(\omega)\cos(\omega\tau)]. \tag{5.43}$$

There are different models to describe $J(\omega)$, which are suitable for different system-environment couplings under study. One typical example is the Ohmic form:

$$J(\omega) = \Theta(\omega)\eta\omega e^{-\frac{\omega}{\omega_c}}, \tag{5.44}$$

where η is a dimensionless parameter to characterize the system-bath coupling strength, and ω_c is the bath cut-off frequency. $\Theta(\omega)$ is the Heaviside step function that guarantees that $J(\omega) = 0$ for $\omega < 0$. An alternative model of the spectral density is the Debye form:

$$J(\omega) = \Theta(\omega)\eta\frac{\omega}{\omega^2 + \omega_c^2}, \tag{5.45}$$

which is generally used to characterize the coupling between solute molecules and polar solvent molecules. Both Ohmic and Debye spectral densities increase linearly in small-frequency region and decrease after reaching the cut-off frequencies. More generally, we can introduce $\mathcal{N}(\omega)$, the density of states of the reservoir, to express the spectral density:

$$J(\omega) \;=\; g_\omega^2 \mathcal{N}(\omega). \tag{5.46}$$

5.2.6 Redfield equation

According to Eq. 5.31, the quantum master equation for the reduced density operator within the Born-Markov approximation reads

$$\frac{\partial}{\partial t}\hat{\rho}_s(t) = -i\hat{L}_s\hat{\rho}_s(t) + \hat{D}\hat{\rho}_s(t), \tag{5.47}$$

where the Liouville superoperator $\hat{L}_s$ describes the reversible part of system dynamics, and the dissipative superoperator $\hat{D}$ is:

$$\begin{aligned}\hat{D}\hat{\rho}_s(t) = -\int_0^\infty d\tau \,\big(\, & C(\tau)[\hat{K}, \hat{K}^{(I)}(-\tau)\hat{\rho}_s(t)] \\ & -C(-\tau)[\hat{K}, \hat{\rho}_s(t)\hat{K}^{(I)}(-\tau)] \,\big)\,,\end{aligned} \tag{5.48}$$

where all terms have been defined for the harmonic-oscillator bath.

In the eigenstate representation of the system Hamiltonian ($\hat{H}_s\,|\phi_i\rangle = E_i\,|\phi_i\rangle$), the quantum master equation for the reduced density matrix becomes

$$\begin{aligned}\frac{\partial}{\partial t}\rho_{ij} = \quad & -i\omega_{ij}\rho_{ij}(t) - \sum_{kl}\int_0^\infty d\tau \\ & \big\{K_{ik}K_{kl}\rho_{kj}C(\tau)e^{-i\omega_{kl}\tau} - K_{ik}\rho_{kl}K_{lj}C(\tau)e^{-i\omega_{ik}\tau} \\ & +\rho_{ik}K_{kl}K_{lj}C(-\tau)e^{-i\omega_{kl}\tau} - K_{ik}\rho_{kl}K_{lj}C(-\tau)e^{-i\omega_{lj}\tau}\big\}\end{aligned} \tag{5.49}$$

with

$$K_{ik} = \langle\phi_i|\,\hat{K}\,|\phi_k\rangle\,, \tag{5.50}$$

$$\omega_{ik} = E_i - E_k. \tag{5.51}$$

This Redfield equation can be expressed in the tensor form [237,239,241,250,251]:

$$\frac{\partial}{\partial t}\rho_{ij} = \quad -i\omega_{ij}\rho_{ij}(t) + \sum_{k,l}\Gamma_{ijkl}\rho_{kl}, \tag{5.52}$$

where the Γ_{ijkl} denote the Redfield tensors

$$\Gamma_{ijkl} = \Gamma^+_{ljik} + \Gamma^-_{ljik} - \delta_{jl}\sum_m \Gamma^+_{immk} - \delta_{ik}\sum_m \Gamma^-_{lmmj}, \tag{5.53}$$

with

$$\begin{aligned}\Gamma^{+}_{ljik} &= \int_0^\infty d\tau K_{lj}K_{ik}e^{-\omega_{ik}\tau}C(\tau) \\ &= K_{lj}K_{ik}\int_0^\infty d\tau\int_0^\omega d\omega\frac{1}{\pi}J(\omega)[e^{-i\omega\tau}+2n(\omega)\cos(\omega\tau)]e^{-i\omega_{ik}}, \quad (5.54)\\ \Gamma^{-}_{ljik} &= \int_0^\infty d\tau K_{lj}K_{ik}e^{-\omega_{lj}\tau}C(-\tau) \\ &= K_{lj}K_{ik}\int_0^\infty d\tau\int_0^\omega d\omega\frac{1}{\pi}J(\omega)[e^{i\omega\tau}+2n(\omega)\cos(\omega\tau)]e^{-i\omega_{lj}}. \quad (5.55)\end{aligned}$$

The integrals in Eqs. 5.54 and 5.55 are evaluated according to the following relations:

$$\begin{aligned}\int_0^\infty d\tau\cos\omega\tau e^{-i\Omega\tau} &= \frac{1}{2}\left[\int_0^\infty d\tau e^{-i(\omega+\Omega)\tau}+\int_0^\infty d\tau e^{i(\omega-\Omega)\tau}\right], \quad (5.56)\\ \int_0^\infty d\tau e^{\pm i(\omega\mp\Omega)\tau} &= \pi\delta(\omega\mp\Omega)\pm i\mathcal{P}\frac{1}{\omega\mp\Omega}, \quad (5.57)\end{aligned}$$

where $\mathcal{P}$ is the Cauchy principal part.

After some algebra, the real parts of the Redfield tensors are given by:

$$\mathrm{Re}(\Gamma^{+}_{ljik}) = K_{lj}K_{ik}\begin{cases} J(\omega_{ki})(1+n(\omega_{ki})) & \text{if } \omega_k > \omega_i \\ J(\omega_{ik})n(\omega_{ik}) & \text{if } \omega_i > \omega_k \\ \lim_{\omega\to 0} J(\omega)(n(\omega)) & \text{if } \omega_k = \omega_i \end{cases} \quad (5.58)$$

$$\mathrm{Re}(\Gamma^{-}_{ljik}) = K_{lj}K_{ik}\begin{cases} J(\omega_{lj})(1+n(\omega_{lj})) & \text{if } \omega_l > \omega_j \\ J(\omega_{jl})n(\omega_{jl}) & \text{if } \omega_j > \omega_l \\ \lim_{\omega\to 0} J(\omega)(n(\omega)) & \text{if } \omega_j = \omega_l \end{cases} \quad (5.59)$$

The real parts of the Redfield tensors describe an irreversible redistribution of the different elements of the reduced density matrix. Γ^{+}_{iijj} and Γ^{-}_{iijj} induce population transfer and relaxation. Γ^{+}_{ijij} and Γ^{-}_{ijij} determine the evolution of the off-diagonal elements of reduced density matrix and describe dephasing processes.

The imaginary parts of the Redfield tensors are given by:

$$\mathrm{Im}(\Gamma^{+}_{ljik}) = K_{lj}K_{ik}\frac{1}{\pi}\left\{\mathcal{P}\int_0^\infty d\omega\frac{J(\omega)n(\omega)}{\omega-\omega_{ik}}-\mathcal{P}\int_0^\infty d\omega\frac{J(\omega)[1+n(\omega)]}{\omega-\omega_{ki}}\right\}, \quad (5.60)$$

$$\mathrm{Im}(\Gamma^{-}_{ljik}) = K_{lj}K_{ik}\frac{1}{\pi}\left\{\mathcal{P}\int_0^\infty d\omega\frac{J(\omega)[1+n(\omega)]}{\omega-\omega_{lj}}-\mathcal{P}\int_0^\infty d\omega\frac{J(\omega)n(\omega)}{\omega-\omega_{jl}}\right\}. \quad (5.61)$$

These terms modify the transition frequencies of the system. These frequency shifts are sometimes called "Lamb shifts".

The Redfield equation was established in the field of nuclear magnetic resonance [249]. For a few-level system (nuclear spin) coupled to a thermal environment (crystal lattic or solvent), the secular approximation to the Redfield equation leads to the Bloch equation, which is essentially the Pauli master equation. Please refer to standard textbooks for details [239, 241, 249].

5.2.7 Solution of the Redfield equation

To solve the Redfield equation, we have to generate the eigenstates of the system Hamiltonian. The methods to perform this task are described in Chapter 4 of this thesis.

The computational cost to solve the Redfield equation is a crucial issue when it is applied to a complex system with many eigenstates. For a N-dimensional density matrix, the computational effort to evaluate the Redfield tensors seems to scale as N^4. However, the explicit construction of the Redfield tensors can be replaced by matrix multiplications, which reduces the scaling of the computational cost to N^3 [250, 251]. If we define two auxiliary matrices, $\mathbf{\Lambda}^+$ and $\mathbf{\Lambda}^-$

$$\Lambda^+_{ik} = K_{ik}\mathrm{Re}\left\{\int_0^\infty d\tau \int_0^\omega d\omega \frac{1}{\pi} J(\omega)[e^{-i\omega\tau} + 2n(\omega)\cos(\omega\tau)]e^{-i\omega_{ik}}\right\}, \quad (5.62)$$

$$\Lambda^-_{lj} = K_{lj}\mathrm{Re}\left\{\int_0^\infty d\tau \int_0^\omega d\omega \frac{1}{\pi} J(\omega)[e^{i\omega\tau} + 2n(\omega)\cos(\omega\tau)]e^{-i\omega_{lj}}\right\}, \quad (5.63)$$

the real parts of the Redfield tensors are rewritten as

$$\mathrm{Re}(\Gamma^+_{ljik}) = K_{lj}\Lambda^+_{ik}, \quad (5.64)$$

$$\mathrm{Re}(\Gamma^-_{ljik}) = \Lambda^-_{lj}K_{ik}. \quad (5.65)$$

In this way, the dissipative part of the Redfield equation is expressed in terms of the products of three matrices: $\mathbf{K}$, $\mathbf{\Lambda}^\pm$ and ρ in the proper ordering.

There are many efficient numerical methods to solve the Redfield equation of motion. Among them, the fourth-order Runger-Kutta scheme is widely used [252].

5.2.8 Advantages and limitations of Redfield theory

The Redfield theory starts from a microscopic model which describes the dissipative quantum dynamics of a system under the influence of en environment. Since both the system and the bath are defined explicitly, the Redfield equation directly displays the physical picture of energy transfer from the system to the environment. This theory is among a limited number of theoretical approaches which can describe dissipative dynamics on the basis of a microscopic model with physical meaning. The Redfield equation also guarantees that the trace of the reduced density matrix is preserved. In addition, the Redfield equation is a time-local quantum master equation. The elimination of memory effects dramatically reduces the numerical cost of the solution of this equation.

Being based on the Born-Markov approximation, Redfield theory cannot describe the dissipative dynamics in the case of strong system-bath coupling. The inclusion of the non-Markovian effects is not trivial and is an open question for the future [242,253–261]. In addition, because the memory kernel is truncated to the second order of $\hat{L}_{sb}$, the positivity of the reduced density operator ($\rho_{ii} \geq 0$) is not strictly preserved. In other words, the Redfield theory generally does not conserve the semi-group property of the density operator [243].

5.3 Quantum dissipative dynamics at conical intersections

5.3.1 Basic model

To describe the quantum dissipative dynamics at conical intersections, we construct a rather simple model. The treatment will be extended to more general systems.

We consider a conical intersection, which is the photo-active center of a large molecule possessing many photo-inactive vibrational degrees of freedom. All of these photo-inactive modes are modelled by harmonic oscillators. The coupling between photo-active modes (tuning and coupling) and photo-inactive modes

leads to dissipation.

In the system-plus-reservoir model, the system is assumed to be a two-state conical intersection with one tuning and one coupling coordinate (R_t, R_c). In the diabatic electronic basis $\{|\phi_k^d\rangle\}$, the system Hamiltonian is given by:

$$\hat{H}_s = \sum_{k=1}^{2} |\phi_k^d\rangle \hat{h}_k \langle\phi_k^d| + \{|\phi_1^d\rangle \hat{h}_{12} \langle\phi_2^d| + c.c.\}, \tag{5.66}$$

where the elements $\hat{h}_k$ are functions of R_t and R_c

$$\hat{h}_k = T + V_k(R_t, R_c), \tag{5.67}$$

and the diabatic coupling is assumed to be a linear function of R_c:

$$\hat{h}_{12} = \sum_c \lambda(R_t) R_c. \tag{5.68}$$

The other photo-inactive vibrational modes are described by a bath composed of many independent harmonic oscillators:

$$\hat{H}_b = \sum_b \frac{\omega_b}{2}(\hat{p}_b^2 + \hat{q}_b^2), \tag{5.69}$$

with the dimensionless coordinates q_b and momenta p_b for a particular harmonic oscillator with frequency ω_b.

The system-bath interaction Hamiltonian is assumed to be:

$$\hat{H}_{sb} = (\hat{H}_{sb}^t + \hat{H}_{sb}^c), \tag{5.70}$$

where $\hat{H}_{sb}^t$ and $\hat{H}_{sb}^c$ denote the system-bath couplings for the tuning and coupling coordinates, respectively.

The system-bath coupling for the tuning coordinate is

$$\hat{H}_{sb}^t = \{|\phi_1^d\rangle \langle\phi_1^d| + |\phi_2^d\rangle \langle\phi_2^d|\} \hat{K}(R_t) \sum_b g_{t,b} \hat{q}_b. \tag{5.71}$$

For the coupling coordinate, the system-bath interaction Hamiltonian contains $\hat{K}(R_c)$, a system operator which is a function of R_c. In most cases, the vibrational motion of the coupling mode is of small amplitude. Thus, it is reasonable to

perform a Taylor expansion of $\hat{K}(R_c)$ with respect to R_c, and keep only the linear term:

$$\hat{K}(\hat{R}_c) = \hat{R}_c. \tag{5.72}$$

When the same ansatz as Eq. 5.71 is used to model the system-bath couplings for the coupling mode, we obtain

$$\hat{H}^c_{sb} = \{|\phi^d_1\rangle\langle\phi^d_1| + |\phi^d_2\rangle\langle\phi^d_2|\}\hat{R}_c \sum_b g_{c,b}\hat{q}_b. \tag{5.73}$$

This system-bath coupling is often used to describe the interactions between solute and solvent molecules. However, it lowers the symmetry of the system Hamiltonian. To describe intramolecular vibrational relaxation of polyatomic molecules, the system-bath coupling for the coupling mode should take the symmetry properties into account. One possible way to model a symmetry-preserving system-bath coupling is

$$\hat{H}^c_{sb} = \{|\phi^d_1\rangle\langle\phi^d_2| + |\phi^d_2\rangle\langle\phi^d_1|\}\hat{R}_c \sum_b g_{c,b}\hat{q}_b. \tag{5.74}$$

5.3.2 Representation of reduced density operator

As discussed in the last section, the eigenstates $\{|\alpha\rangle\}$ of the system Hamiltonian $\hat{H}_s$ can be used to represent the quantum master equation of the reduced density operator. This results in the well-known time-local expression of the Redfield equation, see Eq. 5.49.

Alternatively, the density operator can be expressed in another basis, which is the direct product of the electronic basis $\{\Phi_n\}$ (adiabatic or diabatic) and a suitable basis state $\{\chi_{\nu i}\}$ for each vibrational degree of freedom. The reduced density matrix in this representation has the form:

$$\rho_s(t, \Phi_n, \Phi_{n'}, \nu_t, \nu'_t, \nu_c, \nu'_c) = \langle\Phi_n|\langle\chi_{\nu_t}|\langle\chi_{\nu_c}|\,\hat{\rho}(t)\,|\Phi_{n'}\rangle|\chi_{\nu'_t}\rangle|\chi_{\nu'_c}\rangle. \tag{5.75}$$

A similar expression can also be obtained for a set of grid points:

$$\rho_s(t, \Phi_n, \Phi_{n'}, R_t, R'_t, R_c, R'_c) = \langle\Phi_n|\langle R_t|\langle R_c|\,\hat{\rho}(t)\,|\Phi_{n'}\rangle|R'_t\rangle|R'_c\rangle \tag{5.76}$$

or in the MGBR:

$$\rho_s(t, \Phi_n, \Phi_{n'}, R_t, R'_t, \nu_c, \nu'_c) = \langle\Phi_n|\langle R_t|\langle\chi_{\nu_c}|\,\hat{\rho}(t)\,|\Phi_{n'}\rangle|R'_t\rangle|\chi_{\nu'_c}\rangle. \tag{5.77}$$

5.3.3 Solution of quantum master equation

Instead of the traditional way to solve the Redfield equation in the eigenstate representation, we discuss a new approach in this subsection.

We use the split-operator method to write the short-time propagation of the reduced density operator as [64, 257, 262]:

$$\hat{\rho}_s(t+dt) = e^{-i\hat{L}_s dt/2} e^{\hat{D}dt} e^{-i\hat{L}_s dt/2} \hat{\rho}_s(t), \tag{5.78}$$

where, the operators, $\hat{L}_s$ and $\hat{D}$ describe the reversible dynamics and the dissipative dynamics, respectively. Next, the propagator $\exp(-i\hat{L}_s dt/2)$ can be evaluated by the successive application of the split-operator method

$$\begin{aligned} e^{-i\hat{L}_s dt} &= e^{-i\hat{L}_1 dt/2} e^{-i\hat{L}_2 dt/2} ... e^{-i\hat{L}_n dt} ... e^{-i\hat{L}_2 dt/2} e^{-i\hat{L}_1 dt/2}, & (5.79) \\ \hat{L}_s &= \hat{L}_1 + \hat{L}_2 + ... \hat{L}_n. & (5.80) \end{aligned}$$

The purpose of this splitting technique is that every single propagator can be calculated conveniently in the product-basis-set representation or the MGBR. For example, if $\hat{L}_1$ describes a normal-mode motion, the eigenstates of the harmonic oscillator are selected to evaluate the corresponding propagator $e^{-i\hat{L}_1 dt}$. If the grid representation is used for a coordinate (for instance R_t), the Fourier-transformation method is used to evaluate the propagator containing the kinetic-energy operator [262–264].

To evaluate the propagation governed by $\hat{D}$, we need to represent the operators $\hat{K}$ and $\hat{K}^{(I)}(-\tau)$ in a suitable representation, see Eq. 5.48. For brevity, I only show the procedure to calculate these two operators related to the tuning coordinate in the MGBR here.

For the operator $\hat{K}$, it is rather easy to obtain:

$$\langle \Phi_1 | \langle R_t | \langle \nu_c | \hat{K}(R_t) | \Phi_{1'} \rangle | R'_t \rangle | \nu'_c \rangle = K(R_t) \delta_{\Phi_1, \Phi'_1} \delta_{R_t, R'_t} \delta_{\nu_c, \nu'_c}. \tag{5.81}$$

This shows that the matrix elements of the operator $\hat{K}$ are easier to calculate in the MGBR than in the eigenstate representation.

A central part of the calculation is the representation of the operator $\hat{K}$ in the interaction picture, *i.e.* the term $\hat{K}^{(I)}(-\tau)$. If the eigenstates $\{|\mu_i\rangle\}$ of the

system Hamiltonian have been obtained, $\hat{K}^{(I)}(-\tau)$ in the MGBR is written as:

$$\begin{aligned}
& \langle\Phi_1|\langle R_t|\langle\nu_c|\hat{K}^{(I)}(-\tau)|\Phi_{1'}\rangle|R_t'\rangle|\nu_c'\rangle \\
= & \sum_{\mu_1,\mu_2}\langle\Phi_1|\langle R_t|\langle\nu_c|\mu_1\rangle\langle\mu_1|\hat{K}_1^{(I)}(-\tau)|\mu_2\rangle\langle\mu_2|\Phi_{1'}\rangle|R_t'\rangle|\nu_c'\rangle \\
= & \sum_{\mu_1,\mu_2}\sum_{\Phi_1'',\Phi_1'''}\sum_{R_t'',R_t'''}\sum_{\nu_c'',\nu_c'''} \\
& \langle\Phi_1|\langle R_t|\langle\nu_c|\mu_1\rangle\, e^{-iE_1t}\,\langle\mu_1|\Phi_1''\rangle|R_t''\rangle|\nu_c''\rangle \\
& K(R_t'')\,\delta_{\Phi_1'',\Phi_1'''}\,\delta_{R_t'',R_t'''}\,\delta_{\nu_c'',\nu_c'''} \\
& \langle\Phi_1'''|\langle R_t'''|\langle\nu_c'''|\mu_2\rangle\, e^{iE_2t}\,\langle\mu_2|\Phi_1'\rangle|R_t'\rangle|\nu_c'\rangle\,. \qquad (5.82)
\end{aligned}$$

Eqs. 5.81 and 5.82 imply that the operator $\hat{D}$ in the MGBR is time-local. Therefore, the short-time propagation governed by $\hat{D}$ leads to a linear differential equation for the reduced density matrix. The fourth-order Runge-Kutta method is used to evaluate the propagator $e^{\hat{D}dt}$ for every time step.

In summary, the propagation of the reduced density matrix is performed by the splite-operator method. The use of the optimal representation largely decreases the efforts to calculate the short-time reversible propagation governed by the system Hamiltonian. For the irreversible part of the dynamics governed by the dissipative operator, we use the fourth-order Runge-Kutta method to calculate the short-time propagation.

5.3.4 Preparation of initial state

With in the FC approximation, the initial state is obtained by the vertical excitation of system from the electronic ground state $|\Phi_1\rangle$ to the excited state $|\Phi_2\rangle$:

$$\rho_s(0) = \sum p_v\,|\Phi_2\rangle|\chi_{1,v}\rangle\langle\chi_{1,v}|\langle\Phi_2|\,, \qquad (5.83)$$

where the $|\chi_{1,v}\rangle$ denote vibrational eigenstates in the ground electronic state $|\Phi_1\rangle$, which can be obtained by the standard methods discussed in Chapter 4. p_v is the Blotzmann distribution factor, reflecting the probability distribution of the system in different vibrational states. For sufficiently low temperature, the contribution of the higher vibrational states can be neglected, *i.e.*,

$$\rho_s(0) = |\Phi_2\rangle|0\rangle\langle 0|\langle\Phi_2|\,, \qquad (5.84)$$

where $|0\rangle$ is the lowest vibrational level in the electronic ground state $|\Phi_1\rangle$.

5.3.5 Physical observables

5.3.5.1 Quantum flux

The quantum flux through a dividing surface at R_d is defined by the expectation value of the flux operator $\hat{F}$:

$$F(t) = \text{tr}\left\{\hat{F}\hat{\rho}_s(t)\right\}\Big|_{R_d}, \tag{5.85}$$

where R_d is selected to divide the reactants and products, see chapter 4.

5.3.5.2 Electronic population probability

The diabatic populations are defined as:

$$P_i^d(t) \;=\; \text{tr}_{s,R_n}\left\{\hat{P}_i^{(d)}\hat{\rho}_s(t)\right\}, \tag{5.86}$$

where $\hat{P}_i^{(d)} = \left|\phi_i^d\right\rangle\left\langle\phi_i^d\right|$ is the projection operator for the ith diabatic electronic state. This expression is equivalent to:

$$P_i^d(t) \;=\; \int dR_1 \int dR_2 ... \rho_{s,i,i}(t, R_1, R_1, R_2, R_2 ...), \tag{5.87}$$

where $\rho_{s,i,i}$ is the nuclear probability density in the ith electronic state.

5.3.5.3 Probability density

For one-dimensional or two-dimensional models, it is rather straightforward to display the probability density in the ith diabatic state $\varrho_i^{(d)}$. This nuclear probability density corresponds the diagonal element of reduced density matrix:

$$\varrho_i^d(t, R_1, R_2) = \rho_{s,i,i}(t, R_1, R_1, R_2, R_2). \tag{5.88}$$

For multi-dimensional models, we define the reduced (or compact) probability density for one or two modes by tracing the reduced density operator over the remaining vibrational degrees of freedom:

$$\varrho_i^d(t, R_1, R_2) = \int dR_3 ... \rho_{s,i,i}(t, R_1, R_1, R_2, R_2, R_3, R_3 ...) \tag{5.89}$$

5.3.6 Quantum dissipative dynamics of dissociative systems

We consider here photodissociation processes which take place in excited electronic states of polyatomic molecules. For a polyatomic molecule with a large number of atoms, it is common that conical intersections are located in the dissociation pathway. We therefore consider the system-plus-environment model to explore the quantum dissipative dynamics through a conical intersection for a dissociative system.

In a first approximation, the dissociative system is described by a 2D model, which includes two intersected electronic states and one conical intesection. This model takes the dominant tuning and coupling modes of the conical intersection into account. As discussed in Chapter 2, the tuning coordinate R_t is the reaction coordinate. This means that, along R_t, the reaction pathway goes through the conical intersection towards the dissociative limit. In most cases, the coupling mode can be described in the normal-mode approximation. With these assumptions, the system Hamiltonian has been constructed explicitly according to Eq. 5.66. The photo-inactive modes are treated as harmonic-oscillator bath, see Eq. 5.69.

Since the gradient of the PE surface along R_t provides a large driving force inducing a large-amplitude nuclear motion, considerable excess energy is accumulated in the tuning mode. In the absence of dissipation, the PE gradient pushes the system towards the dissociation limit and a chemical bond is broken. The excess energy in the tuning mode is thus converted into translational energy of the fragments. In competition with dissociation, the system-bath coupling induces vibrational relaxation of the tuning mode. Here we use the standard ansatz in Eq. 5.70 and 5.82 to describe the system-bath coupling for the tuning coordinate. It is reasonable to assume $\hat{K}_t(R_t)$ to be a decreasing function of R_t, for instance

$$K(R_t) = K_0 \exp[-a(R_t - R_0)]. \tag{5.90}$$

This leads to the fact that the system-bath coupling approaches zero in the dissociation limit.

Since the large excess energy exists in the tuning coordinate, rather than in the coupling coordinate, for the dissociative system, the the coupling mode will not be highly excited. This implies that the damping of the coupling mode has relatively little impact on the overall reaction probability. Therefore, we neglect the damping for the coupling coordinate.

The MGBR is used to represent the density operator. For the dissociative coordinate R_t, the grid representation is used. For the coupling coordinate R_c ,the harmonic-oscillator basis representation is used to reduce the computational efforts.

The procedure for the solution of the Redfield equation in the MGBR has been discussed in Subsection 5.3.3. Since we only consider the damping of the tuning coordinate, two operators, $\hat{K}$ and $\hat{K}^{(I)}(-\tau)$ have to be represented in the MGBR. The operator $\hat{K}$ can be directly evaluated according to Eq. 5.81.

For the dissociative system, Eq. 5.82 can not be used directly because of the difficulty to define the eigenstates of the system Hamiltonian. In the present model, the system-bath coupling vanishes in the asymptotic region. Therefore, we define a box enclosing the region in which system-bath coupling is significant. Then a matrix representation of the Hamiltonian inside this box is constructed. The diagonalization of the Hamiltonian matrix in an appropriate representation generates the eigenstates ($|\mu\rangle$) and their energies (E_μ). Since these states are not true eigenstates of the system Hamiltonian, we call them pseudo-eigenstates. The replacement of the true eigenstates in Eq. 5.82 by these pseudo-eigenstates gives the matrix representation of the operator $\hat{K}^{(I)}(-\tau)$. The dynamics governed by Redfield tensors is treated by the fourth-order Runge-Kutta method.

The dissociation probability of the ith electronic state is defined as the time-accumulated flux through a dividing surface at R_D in the asymptotic region, see Eq. 5.85. To calculate electronic population probability, a similar technique as proposed in Chapter 4 is used:

$$P_i^d(t) = \int_0^{R_D} dR_t \sum_{\nu_c} \rho_s(t, R_t, R_t, \nu_c, \nu_c) + F_i^D(t). \tag{5.91}$$

Chapter 6

Quantum dynamics of pyrrole

In this chapter, we describe the photoinduced dynamics of pyrrole at the $^1A_2(\pi\sigma^*)$–S_0 and $^1B_1(\pi\sigma^*)$–S_0 intersections. We treat these two conical intersections separately. Multi-reference electronic-structure methods have been employed to characterize the possible coupling modes. As a first step towards the unravelling of the mechanistic details of the $^1\pi\sigma^*$ driven photochemistry of pyrrole, 2D models are constructed which include the tuning coordinate (the NH stretching coordinate), and the dominant coupling modes for the $^1A_2(\pi\sigma^*)$–S_0 and $^1B_1(\pi\sigma^*)$–S_0 conical intersections, respectively [93]. These calculations reveal the key features of the photoinduced dynamics of pyrrole at the $^1\pi\sigma^*$–S_0 conical intersections. To explore the influence of weak coupling modes on the dynamics, we have extended the 2D WP calculations [89, 93] by including all symmetry-allowed coupling for both $^1\pi\sigma^*$–S_0 conical intersections in pyrrole modes [41].

In the present rather simplified model calculations, all other internal coordinates are kept frozen at their ground-state equilibrium values. This means that we ignore the energy transfer between the active modes and the many other vibrational modes. The effects of the coupling of the active modes with the many inactive modes will be explored in Chapter 8.

It should be mentioned that we also ignore here the possible coupling between the $^1B_1(\pi\sigma^*)$ and $^1A_2(\pi\sigma^*)$ states via in-plane vibrational modes of B_2 symmetry [265, 266]. Moreover, we do not consider the vibronic interaction of the $^1\pi\sigma^*$ states with the optically allowed $^1\pi\pi^*$ states via out-of-plane modes [86], as well

as the $\pi\pi^*$-S_0 couplings [267].

6.1 Identification of coupling modes

6.2 Symmetry selection rules

The selection of the relevant modes of the conical intersections can be performed with the help of symmetry selection rule. Pyrrole possesses C_{2v} symmetry and its 24 internal degrees of freedom correspond to nine A_1, three A_2, eight B_1 and four B_2 vibrational modes:

$$\Gamma = 9\Gamma_{A_1} + 3\Gamma_{A_2} + 8\Gamma_{B_1} + 4\Gamma_{B_2}. \tag{6.1}$$

The NH stretching coordinate r_{NH} of A_1 symmetry is the reaction coordinate for the hydrogen abstraction reaction. For the $^1A_2$–S_0 conical intersection, the coupling coordinates are the three normal coordinates of A_2 symmetry [41]. For the $^1B_1$–S_0 conical intersection, the coupling coordinates are the four normal coordinates of B_1 symmetry [41]. According to the discussions in Chapter 2, the vibronic coupling strengths of these coupling modes at the corresponding conical intersections can be determined according to the PE data obtained from the electronic-structure calculations.

6.2.1 *Ab initio* calculations

The $^1\pi\sigma^*$ states have 3s Rydberg character at the equilibrium geometry of the electronic ground state, but rapidly acquire H1s character along the dissociation path [83]. To account for the diffuseness of the σ^* orbitals, it is necessary to use rather extended basis sets, in particular on the NH group. Throughout our calculations, the augmented correlation-consistent polarised-valence-double-zeta (aug-cc-pVDZ) basis set [268] has been employed. One additional diffuse s function and one additional set of p functions were added at the nitrogen and two additional diffuse s and two additional sets of diffuse p functions to the dissociative hydrogen atom. Their exponents were derived in an even-tempered manner

from the most diffuse s and p functions already present in the aug-cc-pVDZ basis by dividing the exponents successively by a factor of 3.0.

The ground-state equilibrium geometry, the normal modes and the harmonic vibrational frequencies of pyrrole have been obtained with the second-order Møller-Plesset (MP2) method using the GAUSSIAN 98 package [31].

To characterise the $^1B_1$–S_0 and $^1A_2$–S_0 conical intersections, we have performed two independent *ab initio* CASSCF calculations by averaging the CASSCF functional over the $^1B_1$ and S_0, and the $^1A_2$ and S_0 states, respectively. The CASSCF method represents a good compromise between computational cost and accuracy. These calculations were performed with with the MOLPRO package [193].

For the calculation of the $^1A_2$–S_0 conical intersection, the active space consists of three π orbitals and two π^* orbitals, as well as one occupied σ orbital ($9a_1$) and the corresponding σ^* orbital ($10a_1$) of Rydberg character. This active space corresponds to a distribution of 8 electrons in 7 orbitals. For the calculation of the $^1B_1$–S_0 conical intersection, besides the orbitals included in the $^1A_2$–S_0 calculation, it was found to be necessary to include two additional occupied orbitals of σ character ($8a_1$, $6b_2$), and three additional virtual orbitals of σ^* character ($11a_1 - 12a_1$, $7b_2$) to obtain smooth PE surfaces in the region of the barrier of the $^1B_1(\pi\sigma^*)$ surface, where the $^1\pi\sigma^*$ state changes character from $3s$ towards H$1s$. As pointed out in a recent study by Celani and Werner [84], this active space yields the correct ordering of the low-lying valence and Rydberg states under interest.

The internally-contracted MRCI method has been used to calculate the one-dimensional PE functions of the five lowest singlet electronic states along the OH stretching coordinate. All the configuration state functions (CSF) obtained from the CASSCF calculations have been included in the reference space of the MRCI calculations.

6.2.2 *Ab initio* results

The calculated equilibrium geometry of the ground state of pyrrole is in good agreement with previous results [78–82, 84, 85].

Figure 6.1: Potential energy of the five lowest singlet electronic states, S_0, $\pi\sigma^*(A_2)$, $\pi\sigma^*(^1B_1)$, $\pi\pi^*(B_2)$ and $\pi\pi^*(A_1)$ of pyrrole as functions of r_{NH}.

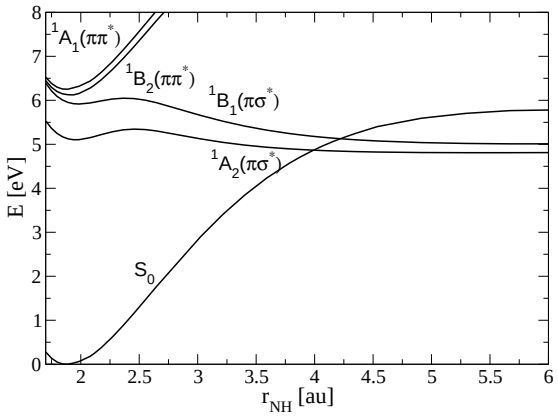

Fig. 6.1 gives an overview of the energies of the five lowest electronic states of pyrrole as a function of the NH stretching coordinate, obtained by CASSCF/MRCI calculations. It is seen that the H atom is strongly bound (by several electron volts) in the electronic ground state, as well as in the $^1\pi\pi^*$ valence states, while the PE functions of the two $^1\pi\sigma^*$ states are essentially repulsive. The low barriers of the $^1\pi\sigma^*$ PE functions near $r_{NH} = 2.5$ au are associated with the Rydberg-to-valence transformation of the σ^* orbital [83]. The $^1\pi\sigma^*$ vertical excitation energies are lower than those of the $^1\pi\pi^*$ valence states. Because of the vibronic couplings between the $^1\pi\pi^*$ and $^1\pi\sigma^*$ states, the $^1\pi\sigma^*$ states can thus be populated by internal conversion after optical excitation of the $^1\pi\pi^*$ states. Both $^1\pi\sigma^*$ PE functions intersect the ground-state PE function in the vicinity of $r_{NH} = 4.2$ au, forming two conical intersections. In the present work, we have characterized the PE surfaces of these conical intersections, considering the NH stretching coordinate and the symmetry-allowed coupling coordinates.

The normal modes, their symmetry labels and the harmonic vibrational frequencies are given in Table 6.1. The vibrational frequencies are in good agreement with previous theoretical data, see Ref. [91] and references therein. The atomic displacement vectors associated with the normal modes of A_2 and B_1 symmetry are shown in Fig. 6.2.

For the $^1A_2$–S_0 conical intersection, the vibronic coupling constants λ of the three A_2 modes at the conical intersection are given in Table 6.2. The mode ν_{11} is found to be the strongest coupling mode with a dimensionless coupling parameter $\lambda/\omega = 1.34$. The other two modes, ν_{10} and ν_{12}, are rather weak coupling modes, with dimensionless coupling parameters in the range 0.42–0.46, three times smaller than that of mode ν_{11}.

For the $^1B_1$–S_0 conical intersection, the coupling constants of the four B_1 modes at the conical intersection are given in Table 6.3. Among them, the strongest coupling mode is ν_{24} with the dimensionless coupling parameter 5.53. This mode possesses the lowest frequency and mainly represents the out-of-plane motion of the H atom of the azine group (see Fig. 6.2). The mode ν_{22} is also a relevant coupling mode, with $\lambda/\omega \sim 0.8$. It corresponds to a combination of the out-of-plane motion of the H atom of the azine group and similar motions of the H atoms of the ring (see Fig. 6.2). The modes ν_{21} and ν_{23}, representing the out-of-plane motions of the N atom or H atoms of the ring, are essentially inactive, see Table 6.3.

6.3 Two-dimensional quantum dynamics of pyrrole

In this section, we construct 2D models to explore the photoinduced dynamics of pyrrole via the two conical intersections ($^1A_2$–S_0 and $^1B_1$–S_0). The models includes the NH stretching as the tuning coordinate and the strongest coupling mode of each conical intersection.

Table 6.1: Harmonic vibrational frequencies of the ground state of pyrrole obtained with the MP2 methods. The frequencies obtained with the DFT method and the B3LYP functional (Ref [91]) are given for comparison.

Mode	Symmetry	ω [cm^{-1}]	
		MP2	DFT
ν_1	A_1	3672.8	3674.7
ν_2	A_1	3304.8	3262.2
ν_3	A_1	3283.2	3240.0
ν_4	A_1	1494.7	1500.5
ν_5	A_1	1430.7	1417.1
ν_6	A_1	1167.5	1173.8
ν_7	A_1	1096.0	1092.2
ν_8	A_1	1035.9	1033.8
ν_9	A_1	882.0	901.9
ν_{10}	A_2	824.3	878.2
ν_{11}	A_2	664.9	686.9
ν_{12}	A_2	608.8	631.0
ν_{13}	B_2	3298.5	3256.3
ν_{14}	B_2	3271.9	3228.7
ν_{15}	B_2	1544.9	1576.5
ν_{16}	B_2	1480.7	1455.8
ν_{17}	B_2	1291.3	1309.0
ν_{18}	B_2	1156.7	1159.0
ν_{19}	B_2	1056.0	1066.6
ν_{20}	B_2	858.9	881.3
ν_{21}	B_1	792.6	830.9
ν_{22}	B_1	716.2	727.8
ν_{23}	B_1	637.1	641.0
ν_{24}	B_1	515.9	474.9

Table 6.2: Harmonic vibrational frequencies ω, $^1A_2$–S_0 coupling parameter λ and dimensionless coupling parameter λ/ω of three A_2 modes at the $^1A_2$–S_0 conical intersection.

Mode	ω [eV]	λ [eV]	λ/ω
ν_{10}	0.102	0.043	0.422
ν_{11}	0.083	0.111	1.337
ν_{12}	0.075	0.035	0.467

Table 6.3: Harmonic vibrational frequencies ω, $^1B_1$–S_0 coupling parameter λ and dimensionless coupling parameter λ/ω of the four B_2 modes at the $^1B_1$–S_0 conical intersection.

Mode	ω [eV]	λ [eV]	λ/ω
ν_{21}	0.098	0.0	0.0
ν_{22}	0.089	0.072	0.809
ν_{23}	0.079	0.0	0.0
ν_{24}	0.064	0.354	5.531

Figure 6.2: Nuclear displacement vectors of the A_2 and B_1 normal modes of pyrrole.

A_2 mode	B_1 mode
ν_{10} 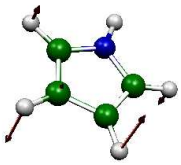	ν_{21} 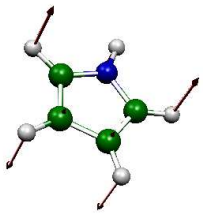
ν_{11} 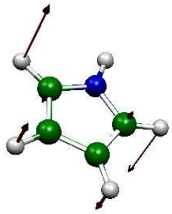	ν_{22} 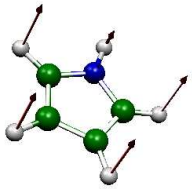
ν_{12} 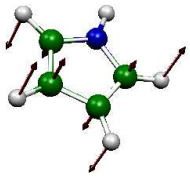	ν_{23} 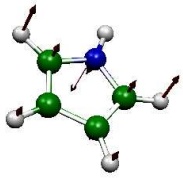
	ν_{24} 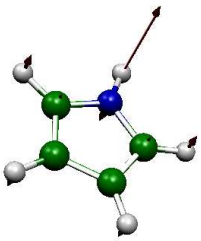

6.3.1 Basic models

6.3.1.1 Molecular Hamiltonian

The Hamiltonian for nuclear motion is expressed in the two-state diabatic basis as

$$\hat{H} = \hat{T}_N \begin{pmatrix} 1 & 0 \\ 0 & 1 \end{pmatrix} + \begin{pmatrix} V_{11} & V_{12} \\ V_{21} & V_{22} \end{pmatrix}. \tag{6.2}$$

where $\hat{T}_N$ is the nuclear kinetic-energy operator. V_{11} and V_{22} describe the PE surfaces of the diabatic electronic states, correlating with the ground diabatic S_0 state and the $^1\pi\sigma^*$ state, respectively. The off-diagonal elements describe the electronic coupling between the respective diabatic states.

6.3.1.2 Diabatic potential surfaces

The diabatic potentials can be constructed by the adiabatic-to-diabatic transformation based on the *ab initio* adiabatic PE surfaces of the $^1\pi\sigma^*$ and S_0 states. In the present rather transparent case of a single conical intersection, we can achieve the diabatization via the *ansatz* of a 2×2 diabatic PE matrix as an analytic function of the nuclear coordinates. The parameters of the *ansatz* are determined by a least-squares fit of the eigenvalues of the PE matrix to the *ab initio* PE data.

The diabatic S_0 PE surface is modelled by a Morse function for the r_{NH} part and a harmonic function along the coupling coordinate Q_c:

$$V_{11}(r_{NH}, Q_c) = v_{11}(r_{NH}) + \frac{1}{2}\omega_c^{(1)}(r_{NH})Q_c^2, \tag{6.3}$$

with

$$v_{11}(r_{NH}) = D_e^1 \left[1 - \exp\left(-a_1(r_{NH} - r_1)\right)\right]^2. \tag{6.4}$$

r_1 corresponds to the equilibrium NH distance of the diabatic S_0 state and D_e^1 is the dissociation energy.

The PE function of the $^1\pi\sigma^*$ state displays a barrier along the NH stretch coordinate. This barrier is reproduced by considering an avoided crossing between a bound $3s$ Rydberg-state [modelled by a Morse potential $v_{21}(r_{NH})$], and a

repulsive valence state [modelled by a repulsive exponential potential $v_{22}(r_{NH})$]. The potential function of the coupling mode is modelled, as in the ground state, by a harmonic oscillator function:

$$V_{22}(r_{NH}, Q_c) = v_{20}(r_{NH}) + \frac{1}{2}\omega_c^{(2)}(r_{NH})Q_c^2, \tag{6.5}$$

where

$$\begin{aligned} v_{20}(r_{NH}) = \quad & \frac{1}{2}(v_{21}(r_{NH}) + v_{22}(r_{NH})) \\ & -\frac{1}{2}\sqrt{\left[(v_{21}(r_{NH}) - v_{22}(r_{NH})\right]^2 + 4\lambda_{22}^2} \end{aligned} \tag{6.6}$$

with

$$v_{21}(r_{NH}) = D_e^{21}\left[1 - \exp\left(-a_{21}(r_{NH} - r_{21})\right)\right]^2 + E_0^2, \tag{6.7}$$

$$v_{22}(r_{NH}) = A_{22}\exp\left(-a_{22}(r_{NH} - r_{22})\right) + D_e^{22}. \tag{6.8}$$

with D_e^{22} corresponding to the dissociation energy of the diabatic $^1\pi\sigma^*$ state.

The coupling element in the diabatic representation is approximately by a linear function:

$$V_{12} = \lambda_{12}(r_{NH})Q_c. \tag{6.9}$$

where λ_{12} is a function of r_{NH}, but is independent of Q_c. All parameters in the definition of V_{11} and V_{22} are determined from one-dimensional cuts of the adiabatic PE surfaces along the NH coordinate. We have calculated one-dimensional cuts along Q_c to determine the values of $\omega_c^{(1)}$, $\omega_c^{(2)}$ and λ_{12} at different values of r_{NH}. We have then chosen appropriate analytic functions to fit the r_{NH} dependence of these parameters.

We choose the following expression for the dependence of the diabatic coupling strength on r_{NH}:

$$\lambda_{12}(r_{NH}) = \frac{1}{2}\lambda_{12}^{max}\left[1 - \tanh\left(\frac{r_{NH} - d_{12}}{\beta_{12}}\right)\right]. \tag{6.10}$$

It is constant for small r_{NH} and approaches zero for $r_{NH} \to \infty$.

6.3.1.3 Preparation of initial vibrational states and WP propagation

The vibrational eigenfunctions of the adiabatic ground surface of pyrrole have been determined by the pseudospectral method detailed in Chapter 4. In this calculation, the initial WP is chosen as the following product of Gaussian functions:

$$\Psi(t=0) = \mathcal{N} \exp\left[-\frac{(r-r_0)^2}{2\sigma_r^2}\right] \times \exp\left[-\frac{(Q_c - Q_{c,0})^2}{2\sigma_c^2}\right] \tag{6.11}$$

which is centered at (r_0, $Q_{c,0}$). We propagate it on the adiabatic ground-state surface to obtain the time-dependent autocorrelation function $C(t)$ and the vibrational eigenstates of the ground electronic state.

The initial WPs for the time-dependent propagation are prepared by vertical electronic excitation, that is, by placing a given vibrational state of electronic ground state into one of the $\pi\sigma^*$ states (see Chapter 4).

The photoinduced dynamics of pyrrole is treated in the time-dependent picture by solving the time-dependent Schrödinger equation for the nuclear motion on the coupled surfaces in diabatic representation. The time-dependent expectation value of adiabatic and diabatic electronic population probabilities, as well as the WP evolution, are calculated to understand the nonadiabatic dynamics at the conical intersections (see Chapter 4).

6.3.2 $^1A_2$–S_0 conical intersection

6.3.2.1 Coupling modes

According to the results in the last section, we know that the mode ν_{11} is the dominant coupling mode for the $^1A_2$–S_0 conical intersection. This coupling mode corresponds to a screwing deformation of hydrogen atoms of the five-membered ring of pyrrole. The calculations show that the diabatic frequencies $\omega_c^{(1)}$ and $\omega_c^{(2)}$ do not depend on r_{NH}.

Tables 6.4- 6.5 give the values of the parameters of the diabatic model for the S_0 and $^1A_2$ states. The average deviation between the fit and the *ab initio* data is 0.01 eV, reaching a maximum of 0.05 eV in the region of the barrier in the $^1\pi\sigma^*$ state.

Table 6.4: Values of the parameters for v_{11}, v_{21} and v_{22} for the $^1A_2$–S_0 model.

V_{11}	V_{22}	
v_{11}	v_{21}	v_{22}
$D_e^1 = 4.979$ eV	$E_0^2 = 4.805$ eV	$A_{22} = 2.644$ eV
$r_1 = 1.927$ au	$D_e^{21} = 4.979$ eV	$D_e^{22} = 3.956$ eV
$a_1 = 1.137$ au	$r_{21} = 1.882$ au	$r_{22} = 2.216$ au
	$a_{21} = 1.293$ au	$a_{22} = 1.325$ au
	$\lambda_{22} = 1.248$ eV	

Table 6.5: Values of the parameters for the strongest coupling mode ν_{11} for the $^1A_2$–S_0 model.

	ω	λ_{12}
Q_{11}	$\omega_c = 0.0825$ eV	$\lambda_{12}^{max} = 0.237$ eV
	$\omega_c^{(1)} = 0.1096$ eV	$d_{12} = 3.679$ au
	$\omega_c^{(2)} = 0.1096$ eV	$\beta_{12} = 1.369$ au
		$\lambda_0 = 0$ au

6.3.2.2 Kinetic-energy operator

For the $^1A_2$–S_0 conical intersection, the kinetic-energy operator in a two-dimensional space, which is spanned by the stretching coordinate r (the distance between the H atom and the center of the mass of the ring) and the dimensionless normal coordinate of the coupling mode Q_{11}, takes the following form:

$$T_N = -\frac{\hbar^2}{2\mu}\frac{\partial^2}{\partial r^2} - \frac{1}{2}\omega_{11}\frac{\partial^2}{\partial Q_{11}^2}, \tag{6.12}$$

where μ is the reduced mass of the NH stretching coordinate of pyrrole and ω_{11} is the frequency of the coupling mode ν_{11} of A_2 symmetry.

6.3.2.3 Adiabatic and diabatic PE surfaces

Our calculation yields a $^1A_2(\pi\sigma^*)$ vertical excitation energy of 4.45 eV, which is in reasonable agreement with the values reported in previous theoretical studies [74, 79–82, 84, 85]. The $^1A_2$ and S_0 dissociation limits of the present CASSCF calculation are 3.96 eV and 4.98 eV, respectively. The former is in excellent agreement with the value of 3.84 eV deduced from the measurement of the kinetic energy release [88].

The two-dimensional diabatic model PE surfaces are displayed as functions of the coordinates r_{NH} and Q_{11} in Fig. 6.3(a). The diabatic coupling matrix element is shown in Fig. 6.3(b). It is a linear function of Q_{11} and approaches zero with increasing NH distance. It is seen that the three diabatic energy surfaces are smooth functions of the nuclear coordinates. Fig. 6.3(c) shows the adiabatic PE surfaces. The conical intersection as well as the shallow well of the $^1\pi\sigma^*$ surface are clearly visible. The diabatic PE surfaces, as well as the coupling elements, are non-separable functions of r and Q_{11}. The adiabatic PE functions acquire an additional pronounced non-separability of the two coordinates through the conical intersection. The height of the barrier for hydrogen detachment in the $^1\pi\sigma^*$ state is 0.4 eV.

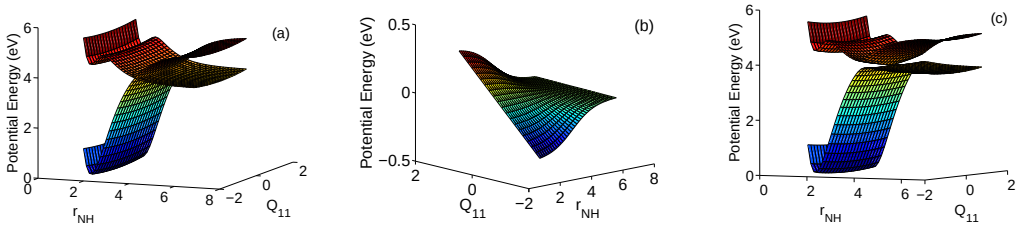

Figure 6.3: V_{11} and V_{22} (a), V_{12} (b) and adiabatic (c) PE surfaces of the S_0 and $^1A_2(\pi\sigma^*)$ states, as functions of the NH stretching coordinate r_{NH} and the dimensionless coupling coordinate Q_{11}.

6.3.2.4 Vibrational eigenstates of the electronic ground-state surface

The center of the initial Gaussian function is located at $r_0 = 4.55$ au and $Q_{c,0} = 2.0$. The width parameters of the Gaussian WP were set to 0.3 au and 1.0 au, for σ_r and σ_c, respectively. This WP is propagated for 4.0 ps with a time-step $\Delta t = 0.05$ fs on a grid which is composed of 128×128 points, ranging from 3.0 au to 6.0 au along the tuning coordinate r, and -15 to 15 along Q_c, respectively. This grid is large enough to ensure that the WP does not reach the grid boundaries during the propagation. No damping function was employed in this calculation.

The lowest vibrational levels of the two-dimensional electronic ground-state surface of the $^1A_2$–S_0 conical intersection model are given in Table 6.6, together with their assignment. n_r and n_c are the occupation numbers of the NH stretching mode and the coupling mode, respectively. The fundamental frequencies of the NH stretching mode and the coupling mode are 3396 cm^{-1} and 689 cm^{-1}, respectively, in acceptable agreement with the experimental values (see [85, 92] and references therein).

6.3.2.5 Electronic population dynamics

When the NH stretching mode is prepared in its ground state, i.e., for the (0,0), (0,1) and (0,2) initial conditions, no fast dynamics takes place. If we put one quantum of energy into the NH stretching mode [the (1,0), (1,1) and (1,2) initial conditions], the adiabatic population probabilities exhibit extensive population

Table 6.6: Eigenvalues (E_n) and assignments (n_r, n_c) of the pseudospectral peaks of the adiabatic ground state of pyrrole for the $^1A_2$-S_0 conical intersection model.

Pyrrole-H					
E_n [cm^{-1}]	(n_r, n_c)	E_n [cm^{-1}]	(n_r, n_c)	E_n [cm^{-1}]	(n_r, n_c)
2095	(0,0)	5492	(1,0)	8728	(2,0)
2785	(0,1)	6176	(1,1)	9412	(2,1)
3469	(0,2)	6865	(1,2)	10101	(2,2)

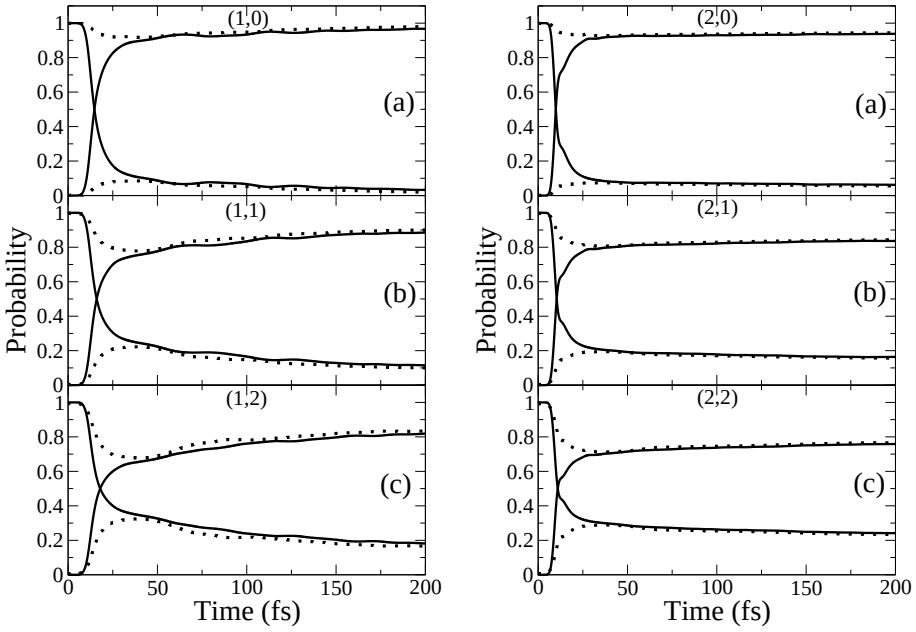

(I) (II)

Figure 6.4: Diabatic (dashed lines) and adiabatic (full line) population probabilities of the $^1A_2(\pi\sigma^*)$ and S_0 states, for the initial conditions $n_r = 1$ (I) [(1,0) (a), (1,1) (b), and (1,2) (c)] and $n_r = 2$ (II) [(2,0) (a), (2,1) (b), and (2,2) (c)] .

transfer within 20 fs. Fig. 6.4 (I) shows that in all cases the diabatic population probability of the $^1A_2$ state (P_1^d, dashed line) decreases in the early stage of the dynamics. After about 30 fs, it rises and finally reaches a plateau. We observe a recovery of the diabatic population P_1^d after 50 fs. If we put two quanta into

the NH stretching mode [the (2,0), (2,1) and (2,2) initial conditions], we also observe very fast decays of the P_1^a populations, see Fig. 6.4 (II). However, the enhancement of the decay time relative to $n_r = 1$ is not significant. The recovery of the diabatic population P_1^d disappears.

The branching ratio of the reaction channels is strongly dependent on the initial vibrational level of the coupling mode ν_{11}. The excitation of this mode enhances the population transfer between the diabatic $^1A_2$ and S_0 states (see full lines in Figs. 6.4), as well as increases the dissociation probability to the upper dissociation channel (see branching ratio in Fig. 6.5). For both the $(1, n_c)$ and $(2, n_c)$ situations, the dissociation probability towards the upper limit increases from about 5% ($n_c = 0$) to more than 20% ($n_c = 3$).

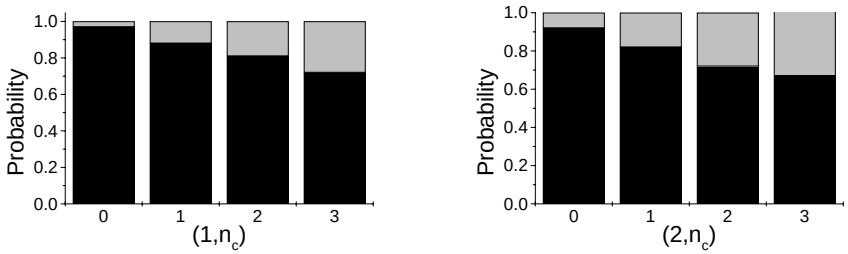

(a) (b)

Figure 6.5: Dissociation probabilities of pyrrole to the lower $^2\pi$-$^2A_2$ (black) and upper $^2\sigma$ (grey) adiabatic limits, for (1,n_c) (a), and (2,n_c) initial conditions (b).

6.3.2.6 Time-dependent wave packets

The lack of ultrafast dynamics for the $n_r = 0$ cases can be understood in terms of the existence of a barrier in the $^1A_2$ state along the NH stretching coordinate (0.40 eV). This barrier induces a well in the $^1A_2$ state, which has a similar shape as the ground state in the bound region, implying that there are no FC factors for transitions to higher vibrational levels of the $^1A_2$ state. The energies of the (0,0), (0,1) and (0,2) initial states are significantly lower than this barrier. Therefore, the WP is trapped in the well of the $^1A_2$ state and it can escape only by quantum

tunnelling. We also note that the barrier on the $^1A_2$ ($\pi\sigma^*$) surface is lower than the upper adiabatic dissociation limit (see Fig. 6.1). Thus, the WP escaping by quantum tunnelling does not have enough energy to dissociate to the upper limit. The upper channel is thus closed and the WP dissociates quantitatively towards the lower limit ($^2\pi$).

The energies of the initial WPs prepared from the (1,0), (1,1) and (1,2) vibrational levels of the electronic ground state are higher in energy than the barrier on the $^1A_2$ state. Therefore, the WPs can overcome the barrier in the $^1A_2$ state and reach the conical intersection very quickly due to the strongly repulsive character of the $^1A_2$ surface. At the conical intersection, the WP splits and moves towards two different dissociation channels, $^2\pi$ and $^2\sigma$.

For sake of illustration, we consider the WPs which evolve after the preparation of the (1,1) initial condition. Figs. 6.6 and 6.7 show the absolute square of the projection of the nuclear WP in the $^1A_2$ and S_0 states, respectively. The time step for the presentation of the WPs is 12 fs.

After the initial WP has been prepared by the vertical excitation, we observe the motion of the WP in the $^1A_2$ state towards the conical intersection within the first 12 fs, see Fig. 6.6(a). The two nodal lines are clearly visible. The central part of the WP follows the diabatic path, while the lateral wings follow an adiabatic path. This explains the pronounced drop of the adiabatic $^1A_2$ population after 12 fs, see Fig. 6.4 (I). In the S_0 state, the nodal line with respect to the coupling coordinate has disappeared, see Fig. 6.7(b). The $^1A_2$ component of the WP rapidly extends to large NH distances owing to the strongly repulsive PE surface of the $^1A_2$ state, see Fig. 6.6(c).

We should keep in mind that the barrier in the $^1A_2$ state is slightly lower than the upper ($^2\sigma$) dissociation limit. The high-energy part of the WP can dissociate towards the upper dissociation limit directly, see Fig. 6.7 (d). The low-energy part of the wave packet, on the other hand, with an energy between the barrier of the $^1A_2$ state and the upper dissociation limit, is reflected by the attractive upper adiabatic potential and re-enters the conical intersection. This process results in pronounced interference patterns in the NH stretching direction, see

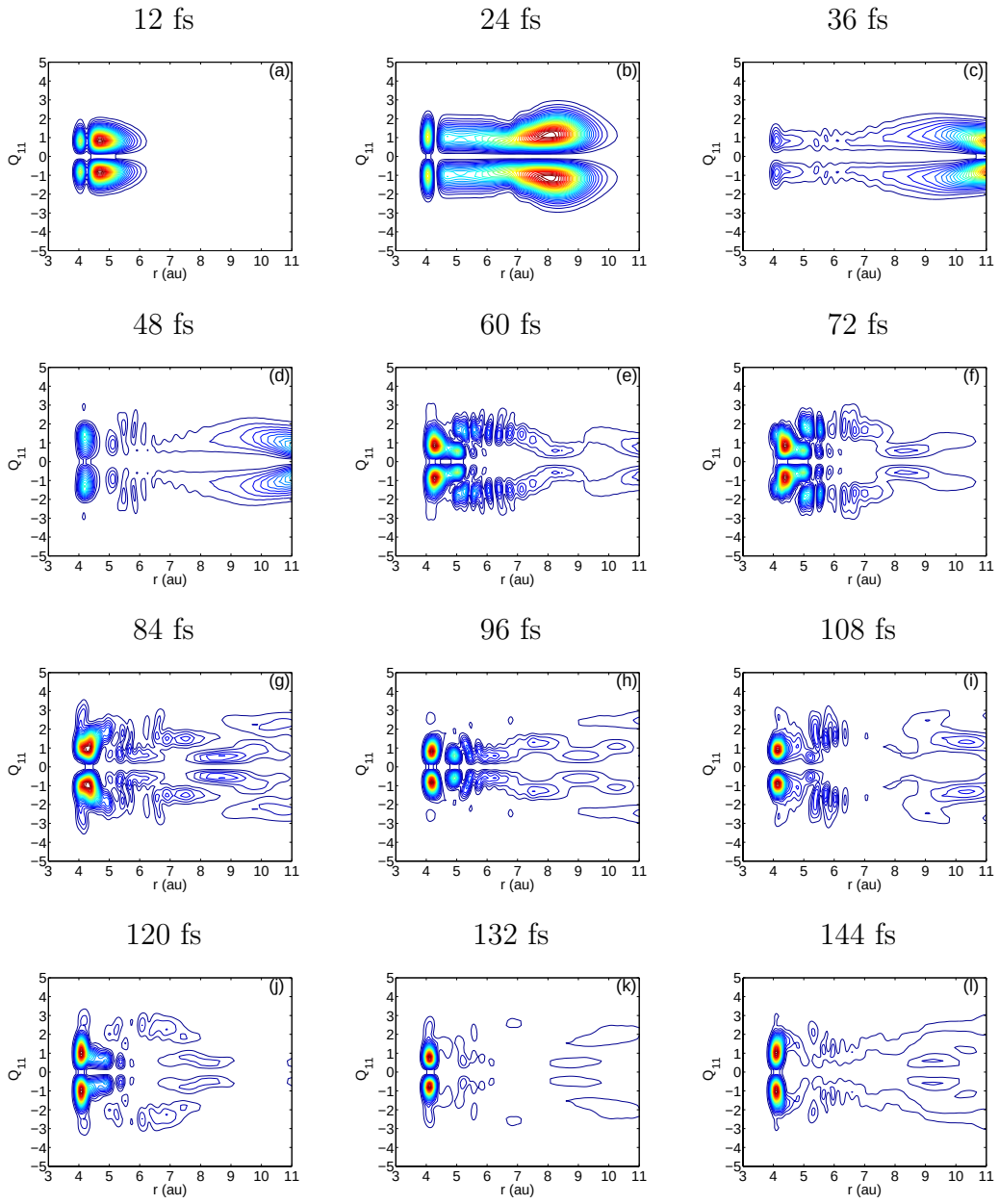

Figure 6.6: Snapshots of the probability density in the diabatic $^1A_2$ state for the (1,1) initial condition. The WP is displayed at every 12 fs.

Figs. 6.6 (d)–(j) and 6.7 (d)–(j). From 48 fs to 120 fs, a component of the WP oscillates in the upper cone of the conical intersection, see Fig. 6.6 (d)–(j) and 6.7 (d)–(j). Each time it passes the region of the conical intersection, a fraction switches to the lower adiabatic surface and dissociates to the ground state of the

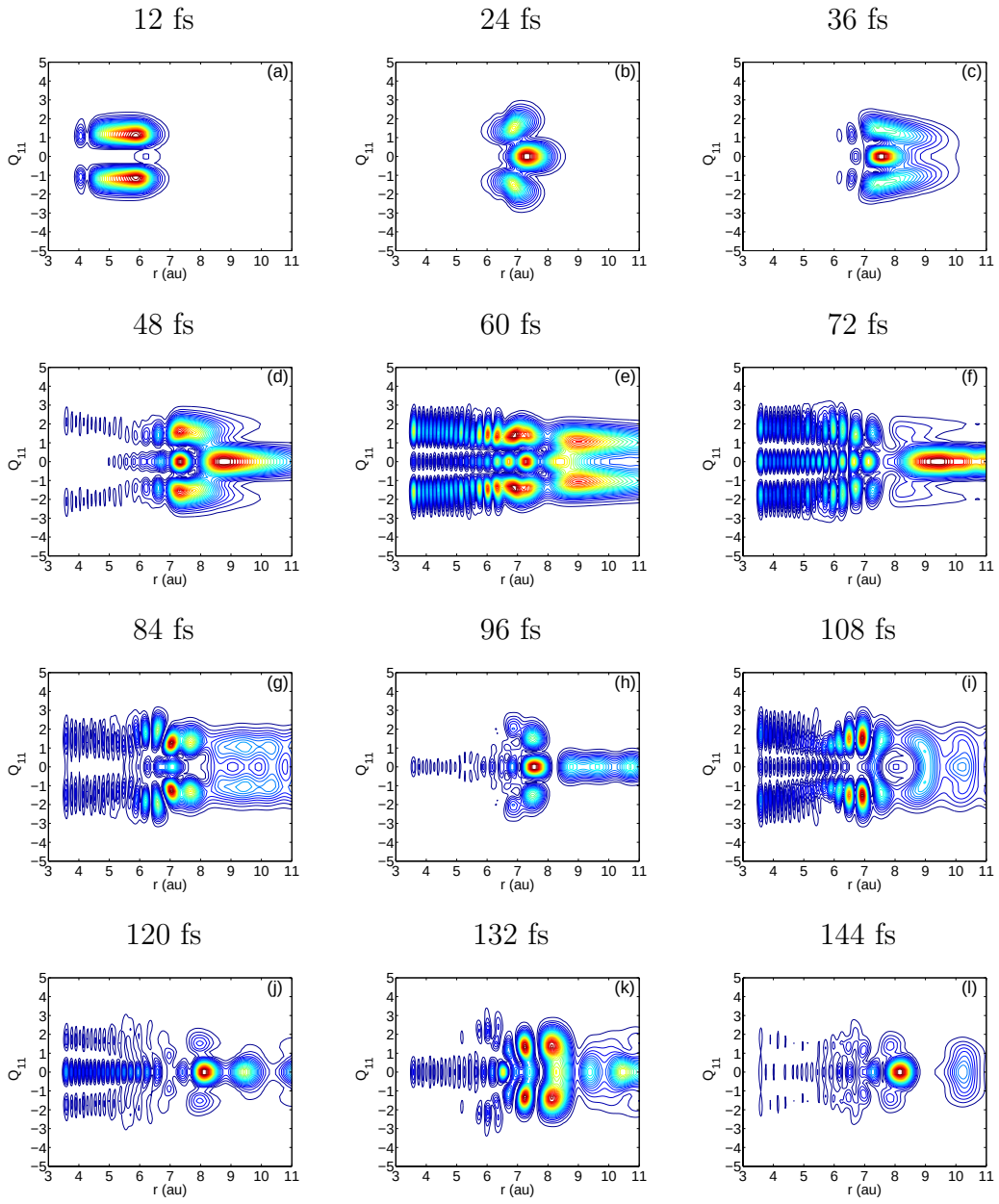

Figure 6.7: Snapshots of the probability density in the diabatic ground S_0 state for the (1,1) initial condition. The WP is displayed at every 12 fs.

pyrrolyl radical. This explains the recovery of P_1^d after 50 fs, see Fig. 6.4 (l).

In the above process, only a tiny part of the WP in the S_0 state enters the region of small NH distances. This part of the WP exhibits a multi-node structure, reflecting the large excess energy in the NH stretching motion. In other

words, the molecule is in a highly vibrationally excited quasi-stationary state. In the absence of energy transfer to other vibrational modes, this hot molecule will eventually dissociate. This implies the absence of internal conversion to the ground state in the two-mode model.

6.3.3 $^1B_1$–S_0 conical intersection

6.3.3.1 Coupling modes

For the $^1B_1$–S_0 conical intersection, we have shown that the strongest coupling mode is ν_{24}. This mode is essentially the out-of-plane bending motion of the hydrogen atom of the azine group. We treat the dynamics of pyrrole in a two-dimensional space which is spanned by the NH stretching coordinate and the hydrogen out-of-plane bending coordinate θ, see Fig. 6.8 (a).

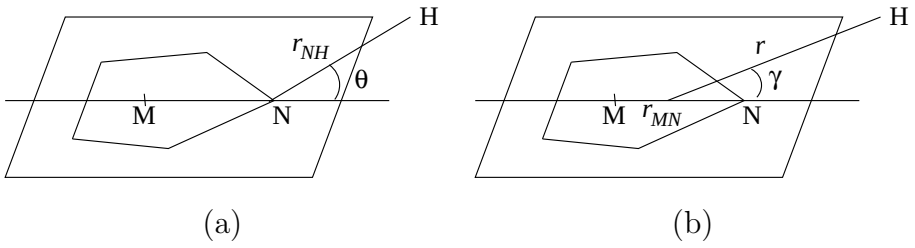

Figure 6.8: Definition of the tuning coordinate and the coupling coordinate in the internal (a) and Jacobi (b) coordinate for the $^1B_1$-S_0 conical intersection in pyrrole.

For the $^1B_1$–S_0 conical intersection, the harmonic frequency corresponding to the coupling mode θ for the diabatic S_0 potential was fitted by a linear function in the inner region, an exponentially decaying function in the outer region, and a switching function connecting the two:

$$\begin{aligned} \omega_c^{(1)}(r_{NH}) = \quad & (B_{11} + B_{12}r)(1 - f_1(r_{NH})) \\ & + B_{13} \exp\left(-B_{14}(r_{NH} - d_1)\right) f_1(r_{NH}), \qquad (6.13) \\ f_1(r_{NH}) \;=\; & \frac{1}{2}\left[1 + \tanh\left(\frac{r_{NH} - d_2}{\alpha_1}\right)\right]. \qquad (6.14) \end{aligned}$$

The harmonic frequency of the $^1\pi\sigma^*$ state is represented by an avoided-crossing

Table 6.7: Values of the parameters for the tuning mode of the $^1B_1$–S_0 model.

V_{11}	V_{22}	
v_{11}	v_{21}	v_{22}
$D_e^1 = 5.117$ eV	$E_0^2 = 5.584$ eV	$A_{22} = 0.091$ eV
$r_1 = 1.959$ au	$D_e^{21} = 8.070$ eV	$D_e^{22} = 4.092$ eV
$a_1 = 1.196$ au	$r_{21} = 1.922$ au	$r_{22} = 5.203$ au
	$a_{21} = 0.822$ au	$a_{22} = 1.290$ au
	$\lambda_{22} = 1.669$ eV	

Table 6.8: Numerical values of the parameters for the coupling mode of the $^1B_1$–S_0 diabatic model.

V_{11} $\omega_c^{(1)}$	V_{22} $\omega_c^{(2)}$	V_{12} λ_{12}
$B_{11} = 5.147$ eV	$B_{21} = 3.819$ eV	$\lambda_{12}^{max} = 2.4$ eV
$B_{12} =$ -1.344 eV	$B_{22} =$ -1.219 eV/au	$d_{12} = 3.454$ au
$B_{13} = 0.884$ eV	$B_{23} = 2.335$ eV$^{1/2}$	$\beta_{12} = 1.942$ au
$B_{14} = 1.2910$ au	$B_{24} = 0.226$ eV$^{1/2}$	
$d_1 = 3.100$ au		
$d_2 = 2.696$ au		

like function:

$$\omega_c^{(2)}(r_{NH}) = \frac{1}{2}(B_{21} + B_{22}r_{NH}) - \frac{1}{2}\sqrt{(B_{23} + B_{22}r_{NH})^2 + 4B_{24}^2}. \quad (6.15)$$

$\omega_c^{(2)}(r_{NH})$ was set to zero when r_{NH} is larger than 2.55 au.

Tables 6.7 and 6.8 give the values of the parameters appearing in the diabatic model for the $^1B_1$–S_0 conical intersection. The average deviation between the fit and the *ab initio* data is 0.01 eV, reaching a maximum of 0.05 eV in the region of the barrier in the $^1\pi\sigma^*$ state.

6.3.3.2 Kinetic-energy operator

The system is considered to be an effective three-body system, composed of hydrogen, nitrogen and M, the center of mass of the rest of the rigid pyrrole ring. To construct the kinetic-energy operator, we employ Jacobi coordinates (see Fig. 6.8 (b)). r_{MN} is the distance between M and the nitrogen atom. This distance is kept fixed in the dynamics calculation. r is the distance between the active hydrogen and the centre of mass of the M-N unit, and γ is the angle between $\vec{r}_{MN}$ and $\vec{r}$. In this set of coordinates, the kinetic-energy operator takes the following form

$$\hat{T}_N = -\frac{\hbar^2}{2\mu}\frac{\partial^2}{\partial r^2} - \frac{\hbar^2}{2I}\frac{\partial^2}{\partial \gamma^2}, \tag{6.16}$$

with

$$\begin{aligned} \mu &= \frac{m_H(m_M + m_N)}{(m_H + m_M + m_N)}, \\ \mu_{MN} &= \frac{m_M m_N}{(m_M + m_N)}, \\ m_M &= 4(m_C + m_H), \\ \frac{1}{I} &= \frac{1}{\mu r^2} + \frac{1}{\mu_{MN} r_{MN}^2}. \end{aligned} \tag{6.17}$$

The quantities m_H, m_N and m_M denote the masses of hydrogen, nitrogen, and the four C-H pairs, respectively, and I is the moment of inertia of the total system.

6.3.3.3 Adiabatic and diabatic PE surfaces

The CASSCF calculations yield a $^1B_1(\pi\sigma^*)$ vertical excitation energy of 5.3 eV. This value is in good agreement with the values reported in previous theoretical studies at different computational levels [79–82, 84, 85]. The dissociation limits, corresponding to the $^2\pi$ and $^2\sigma$ states of the pyrrolyl radical, are 4.09 eV and 5.12 eV, respectively, at the CASSCF level.

The two-dimensional diabatic model PE surfaces (diagonal elements of $\mathbf{V}^d$) are displayed as functions of the coordinates r_{NH} and θ in Fig. 6.9(a). It is seen that the three diabatic energy surfaces are smooth functions of the nuclear coordinates. The diabatic coupling matrix element is shown in Fig. 6.9(b). It is a linear function of θ and approaches zero with increasing NH distance. The

adiabatic PE functions acquire an additional pronounced non-separability of the two coordinates through the conical intersection. Fig. 6.9(c) shows the adiabatic PE surfaces in the two-dimensional space. The conical intersection as well as the shallow well of the $^1\pi\sigma^*$ surface are clearly visible. The height of the barrier for hydrogen detachment in the $^1\pi\sigma^*$ state is 0.26 eV.

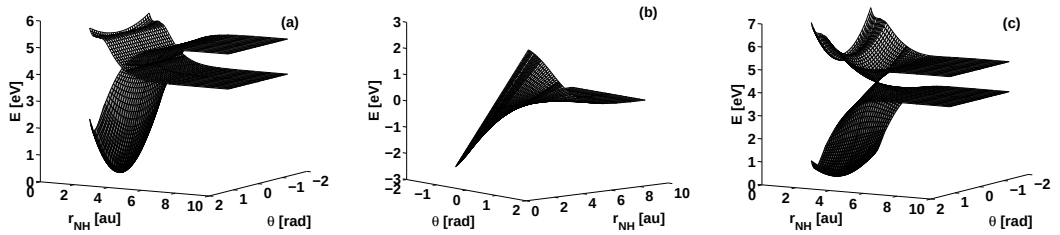

Figure 6.9: Diabatic (V_{11} and V_{22}) (a), V_{12} (b) and adiabatic (c) PE surfaces of the S_0 and $^1B_1(\pi\sigma^*)$ states, as a function of the NH stretching coordinate r_{NH} and the H out-of-plane coupling coordinate θ.

6.3.3.4 Vibrational eigenstates of the electronic ground-state surface

In the pseudo-spectral calculation, the center of the Gaussian wavefunction has been located at $r_0 = 4.55$ au and $\gamma_0 = 0.25$ rad. The width parameters of the Gaussian WP were set to 0.3 au and 0.25 au, for σ_r and σ_c, respectively. This WP is propagated for 4.0 ps with a time-step $\Delta t = 0.05$ fs on a grid which is composed of 128×128 points, ranging from 3.0 au to 6.0 au along the tuning coordinate r, and -2.0 rad to 2.0 rad along γ, respectively.

The energy eigenvalues of the lowest vibrational states of the adiabatic ground-state surface and their assignments in terms of quantum numbers are given in Table 6.9. The quantities n_r and n_γ in this table denote the quantum numbers of the tuning mode and the coupling mode, respectively. The fundamental frequencies of the NH stretching mode and the coupling mode (out-of-plane NH bending) are 3598 cm^{-1} and 523 cm^{-1}, respectively. The corresponding experimental values (see [85,92] and references therein) are 3531 cm^{-1} and 475 cm^{-1}, respectively. Our two-dimensional model reproduces these values with reasonable accuracy.

Table 6.9: Eigenvalues (E_n) and assignments (n_r, n_γ) of the pseudospectral peaks of the adiabatic ground state for pyrrole-H and pyrrole-D for the $^1B_1$–S_0 conical intersection model.

Pyrrole-H					
E_n [cm^{-1}]	(n_r, n_γ)	E_n [cm^{-1}]	(n_r, n_γ)	E_n [cm^{-1}]	(n_r, n_γ)
2131	(0,0)	5729	(1,0)	9150	(2,0)
2654	(0,1)	6225	(1,1)	9617	(2,1)
3168	(0,2)	6713	(1,2)	10072	(2,2)

6.3.3.5 Electronic population dynamics

When the NH stretching mode is prepared in its ground state, that is, for the initial conditions (0,n_γ), we observe two processes with distinctly different timescales. Both the diabatic and adiabatic pictures indicate a rapid population transfer from the excited state to the ground state during the early stage of the dynamics (about 10 fs), followed by a slow and monotonic decay (see Fig. 6.10 (I)). The latter time scale has recently been confirmed by the femtosecond time-resolved detection of the fast hydrogen atoms after photoexcitation of pyrrole [90]. When the NH stretching mode is initially excited, that is for the (1,n_γ) (Fig. 6.10 (II)) and (2,n_γ) (not shown here) initial conditions, the WP reaches the conical intersection within 10 fs and the population transfer is essentially completed after 20 fs. The dissociation probabilities, $P_0^d(t \to \infty)$ and $P_1^d(t \to \infty)$, on the S_0 and $^1B_1$ surfaces, respectively, are shown in Figure 6.11. It is noteworthy that the branching ratio does not depend on the excitation of the NH stretching mode.

The branching ratio depends, however, strongly on the excitation level of the coupling mode, as shown by Fig. 6.11. For the (0,0) initial state, most of the WP (75 %) dissociates to the lower adiabatic limit, while 25 % of the wave packet arrives at the upper adiabatic limit. When one quantum of the coupling mode is excited, the flux splits approximately equally between the two channels. When more energy is put into the coupling mode, the WP dissociates primarily to the higher adiabatic limit. The branching ratio saturates at 25 %/75 % at $n_\gamma = 3$. Similar observations can be made for the series $(1, n_\gamma)$ and $(2, n_\gamma)$, $n_\gamma = 0 - 4$.

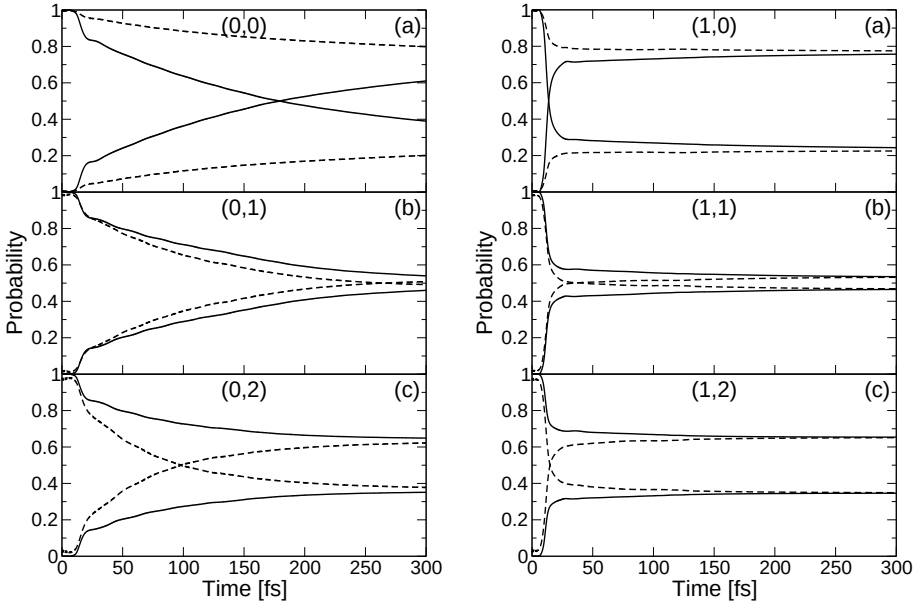

Figure 6.10: Diabatic (dashed lines) and adiabatic (full line) population probabilities of the $^1B_1(\pi\sigma^*)$ and S_0 states, for the initial conditions $n_r = 0$ (I) [(0,0) (a), (0,1) (b), and (0,2) (c)] and $n_r = 1$ (II) [(1,0) (a), (1,1) (b), and (1,2) (c)] .

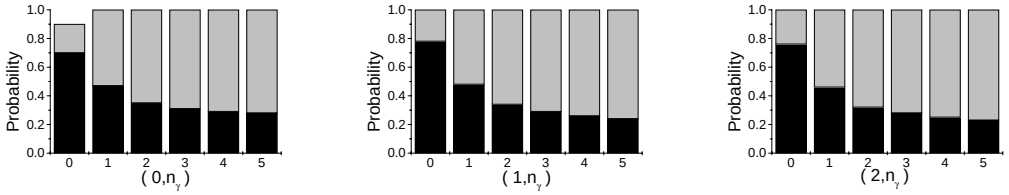

Figure 6.11: Dissociation probabilities of pyrrole to the lower $^2\pi$-$^2B_1$ (black) and upper $^2\sigma$ (grey) adiabatic limits, for (0,n_γ) (a), (1,n_γ) (b), and (2,n_γ) initial conditions (c).

In summary, the higher the excitation of the coupling mode, the larger is the probability for dissociation to the upper adiabatic channel. This feature of the $^1B_1$–S_0 conical intersection can be used to tune the branching ratio of the two

dissociation channels.

6.3.3.6 Time-dependent wave packets

The different timescales of the population transfer dynamics for the $n_r = 0$ situation at two conical intersections, [$^1B_1$–S_0 and $^2A_1$–S_0] reflect the influence of the different barrier heights on the dynamics. Because the $^1B_1$ state has a lower barrier than the $^2A_2$ state, the dynamics is different. While the high-energy component of the WP can overcome the barrier of the $^1B_1$ state and reaches the conical intersection within 10 fs, the low-energy part is captured in the well of the $^1B_1$ state and can reach the conical intersection only by quantum tunnelling, which happens on a rather long time-scale, about a few hundred femtoseconds.

When one quantum of the NH stretching mode is excited, most of the initial WP has enough energy to overcome the barrier in the $^1B_1$ state and reach the conical intersection directly. This explains the single ultrafast decay of the population of the $^1B_1$ state (Fig. 6.10 (II)).

For the sake of illustration, we analyze the evolution of wave packets which have been prepared in the (1,0) and (1,1) vibrational states, respectively. The probability densities (i.e., the absolute squares of the projection of the nuclear WPs on the diabatic $^1B_1$ and S_0 states) at different times are shown in Fig. 6.12 [(1,0) initial condition] and 6.13 [(1,1) initial condition].

As displayed in Fig. 6.12, the shape of the initial (1,0) WP in the $^1B_1$ state does not change during the first 10 fs. The node in the NH-stretching direction is clearly visible. After about 10 fs, the major part of WP has reached the conical intersection and is partly transferred to the S_0 state. In the S_0 state, a nodal line at $\gamma = 0$ has been generated by the $^1B_1$–S_0 conical intersection. This node results from the fact that the diabatic coupling operator is an odd function of the coupling coordinate γ. The two parts of the wave function move around the conical intersection following two different adiabatic paths (clockwise and anticlockwise), and interfere destructively for $\gamma = 0$. After the transition through the conical intersection, both components of the WPs dissociate directly, see Fig. 6.12(c) and (f). We do not observe any probability density for small NH

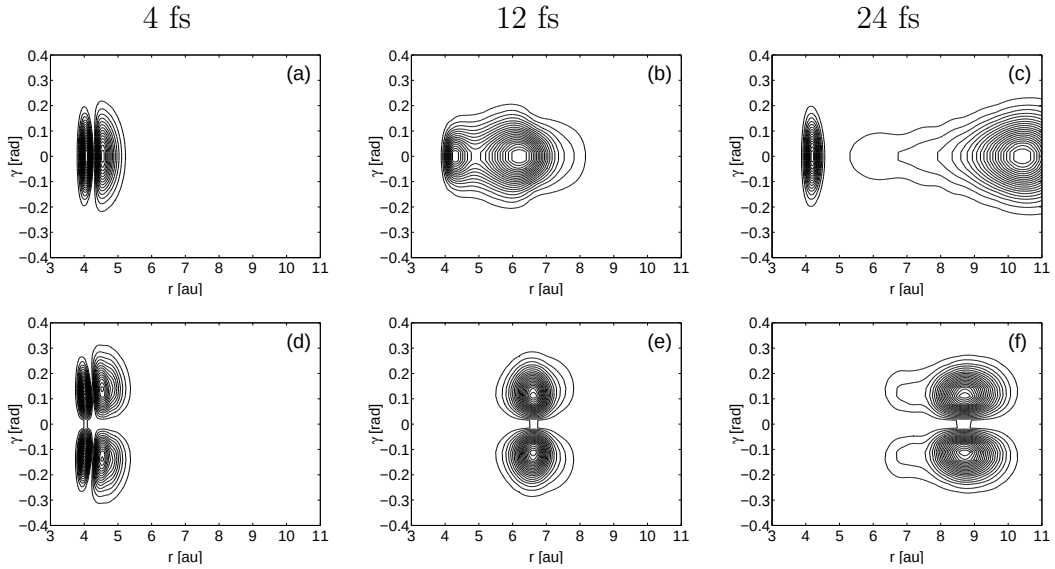

Figure 6.12: Snapshots of the probability density in the diabatic $^1B_1(\pi\sigma^*)$ [(a)-(c)] and ground states [(d)-(f)] for the (1,0) initial condition.

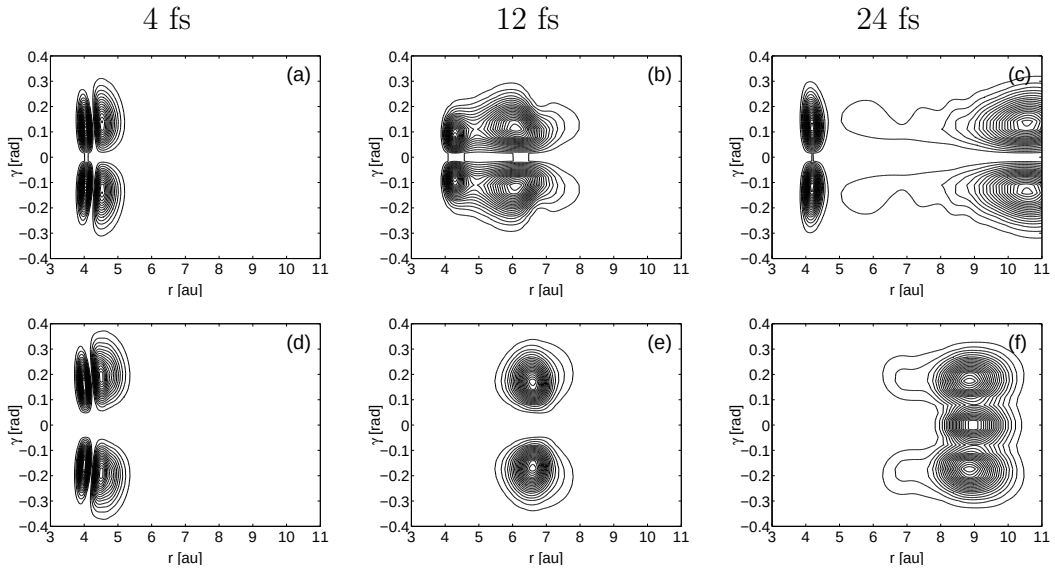

Figure 6.13: Snapshots of the probability density in the diabatic $^1B_1(\pi\sigma^*)$ [(a)-(c)] and ground states [(d)-(f)] for the (1,1) initial condition.

distances in the S_0 state (see Fig. 6.12 (f)). This reflects the absence of internal conversion to the ground state in this two-mode model of the $^1B_1$–S_0 conical intersection.

Let us now discuss the motion of the WP after preparation of the (1,1) initial condition (Fig. 6.13). The initial WP in the $^1B_1(\pi\sigma^*)$ state has two nodal lines after the preparation. While the node with respect to the out-of-plane angle is rigorously preserved by symmetry in the $^1\pi\sigma^*$ state, the node with respect to the NH stretching coordinate disappears during the barrier crossing in $^1B_1$ state (Fig. 6.13(b)). The node with respect to γ is cancelled by the transition to the diabatic S_0 state, i.e. the resulting WP is node-less, (see Fig. 6.13(f)). Figs. 6.13 (d) and (e) reveal the repulsion of the WP on the S_0 surfaces from planarity (γ=0) due to the pronounced cone on the S_0 energy surfaces (see Fig. 6.9 (c))

The projected nuclear probability densities obtained for initial conditions with higher excitation of the coupling mode, $(1, n_\gamma)$ with $n_\gamma \geq 2$, are qualitatively similar and therefore are not shown here. The increasing probability of dissociation to the upper adiabatic channel with increasing excitation of the coupling mode can be rationalized as follows. With increasing excitation of the coupling mode, the density as a function of γ becomes more delocalized. As a consequence, the WP tends to follow the adiabatic rather than the diabatic surfaces. Beyond a certain quantum number n_γ, the density of the wave function in the small γ range, which follows the diabatic path, remains nearly constant. This explains the saturation of the branching ratio which is clearly seen in Fig. 6.11.

In addition, we have analyzed the WP in order to understand why the excitation in the tuning mode has no effect on the branching ratio. The analysis shows that the shape of the wave packet along the coupling coordinate is only weakly dependent on the quantum number in the tuning mode.

6.4 Multi-mode dynamics of pyrrole

To explore the influence of additional weak coupling modes on the dynamics, we have extended the 2D models to include all symmetry-allowed coupling modes for the corresponding conical intersections. This results in 4D and 5D models for the $^1A_2$–S_0 and $^1B_1$–S_0 conical intersections, respectively. Similar to the 2D case, we construct the multidimensional surfaces for both conical intersections using accurate *ab initio* electronic structure calculations. To achieve a reasonable com-

promise between the computational cost and the physical importance, the WP calculations have been performed by taking the two dominant coupling modes of each conical intersection into account. The dependence of the electronic population dynamics on the mode-specific vibrational preparation has been investigated. These calculations provide the insight into the effect of multiple coupling modes on the process of the direct photodissociation through conical intersections.

6.4.1 Basic model

6.4.1.1 Diabatic model

The multi-mode molecular Hamiltonian of the $\pi\sigma^*$–S_0 conical intersection is analogous to the two-mode case, see Section 6.3. Here, we describe all inter-state couplings in terms of normal modes. The kinetic-energy operator therefore takes the simple form:

$$\hat{T}_N = -\frac{\hbar^2}{2\mu}\frac{\partial^2}{\partial r^2} - \sum_c \frac{1}{2}\omega_c \frac{\partial^2}{\partial Q_c^2}, \tag{6.18}$$

where μ is the reduced mass corresponding to the motion of the H atom relative to the ring part of pyrrole. r is defined as the distance between the H atom and the center of mass of the ring. The Q_c are dimensionless normal coordinates with corresponding frequencies ω_c. Here the summation is over all symmetry-allowed coupling modes.

The potential part of the molecular Hamiltonian is constructed according to the same ansaz as the 2D model case. The only difference is that we have to take the contributions of all coupling modes in account. Thus, the extension of the 2D diabatic model results in the multi-mode model:

$$V_{11} = v_{11}(r_{NH}) + \sum_c \frac{1}{2}\omega_c^{(1)}(r_{NH})Q_c^2, \tag{6.19}$$

$$V_{22}(r_{NH}, Q_c) = v_{20} + \sum_c \frac{1}{2}\omega_c^{(2)}(r_{NH})Q_c^2, \tag{6.20}$$

$$V_{12} = \sum_c \lambda_c(r_{NH})Q_c. \tag{6.21}$$

where all parameters are defined in the same way as in the 2D model.

6.4.1.2 Preparation of initial states and wave-packet propagation

The vibrational eigenstates of the adiabatic ground-state PE surface are constructed within the time-independent framework by the diagonalization of the adiabatic ground-state Hamiltonian in a finite-basis representation. The initial WPs are prepared by vertical electronic excitation, that is, by placing a given vibrational state of the electronic ground state into one of the $^1\pi\sigma^*$ excited states. The multi-mode quantum dynamics of pyrrole is explored using time-dependent methods.

For the large-amplitude coordinate r, we adopt the representation of the WP on an equidistant grid. For the coupling modes, it is more economical to employ an expansion of the WP in harmonic-oscillator basis functions. This MGBR is the optimal choice for the representation of the Hamiltonian. The details can be found in Chapter 4.

In the diagnalization of the ground-state Hamiltonian, we have employed 64 DVR points from 3.0 au to 6.2 au for r. We have used 10 harmonic-oscillator basis functions to represent the Hamiltonian for the each of the coupling modes.

The WPs are propagated in the MGBR on the two coupled surfaces using the split-operator method [217]. We employ the FFT method [218] to evaluate the kinetic-energy operator of the NH stretching coordinate. We use the same grid spacing here and extend our grid to 256 points, from 3.0 au to 15.8 au. 10 harmonic-oscillator basis functions are employed for each of the coupling modes. The WPs are propagated for 200 fs with a time step of 0.1 fs. All calculations have been checked to guarantee converged results with respect to grid size and time step.

The time-dependent electronic populations and the motion of the WP are calculated to get the insight into the mechanism of nonadiabatic dynamics governed by multiple coupling modes. In Chapter 4, we have explained the trick to calculate the electronic population for dissociative systems. We determine the dissociation probability by measuring the reactive flux passing through a dividing surface located at $r = 12$ au. To avoid the reflection at the grid boundary in the r direction, we apply a damping function from 13.5 au to 15.8 au.

Table 6.10: Values of the parameters pertaining to the weak coupling modes for the $^1A_2$–S_0 model.

	ω	λ_c
Q_{10}	$\omega_c = 0.1022$ eV	$\lambda_{12}^{max} = 0.066$ eV
	$\omega_c^{(1)} = 0.1077$ eV	$d_{12} = 4.364$ au
	$\omega_c^{(2)} = 0.1155$ eV	$\beta_{12} = 1.478$ au
		$\lambda_0 = 0$ au
Q_{12}	$\omega_c = 0.0756$ eV	$\lambda_{12}^{max} = 0.151$ eV
	$\omega_c^{(1)} = 0.0887$ eV	$d_{12} = 2.643$ au
	$\omega_c^{(2)} = 0.0487$ eV	$\beta_{12} = 0.980$ au
		$\lambda_0 = 0.021767$ au

6.4.2 $^1A_2$–S_0 conical intersection

The coupling strength of ν_{11} is much stronger than that of the other two modes of A_2 symmetry. In the previous discussion, we have taken only this coordinate into account as the coupling coordinate to construct a two-dimensional (2D) model. The coupling modes ν_{10} and ν_{12} have similar coupling strengths at the conical intersection and their coupling strengths are much weaker than that of ν_{11}, see Table 6.10.

To investigate the effect of the weak coupling modes on the dynamics of the $^1A_2$–S_0 conical intersection, we add ν_{10} or ν_{12} to the 2D model to obtain a three-dimensional (3D) model. The WP calculations show that influence of ν_{12} on the dynamics is more prominent than that of ν_{10}. Therefore, we discuss only the results of the 3D model which includes the strong coupling mode ν_{11} and the weak coupling mode ν_{12}.

6.4.2.1 Vibrational eigenstates of the electronic ground-state surface

The lowest vibrational levels of the 3D electronic ground-state surface of the $^1A_2$–S_0 conical intersection model have been calculated by diagonalization of the ground state Hamiltonian. We designate the occupation numbers of the NH

stretching mode, the strong coupling mode (ν_{11}) and the weak coupling mode (ν_{12}) as n_r, $n_{c,1}$ and $n_{c,2}$, respectively. The fundamental frequencies of these three vibrations are 3405 cm^{-1}, 675 cm^{-1} and 613 cm^{-1}, respectively, in the 3D model, in acceptable agreement with the experimental and full-dimensional harmonic frequencies (see [85, 92] and references therein).

6.4.2.2 Electronic population and wave-packet dynamics

Similar to the 2D calculation results, the 3D calculations also show that photoinduced reaction rate is highly dependent on the the initial preparation of the NH stretching motion. When the NH stretching mode is prepared in its ground state [the $(0, n_{c,1}, n_{c,2})$ initial conditions], no fast dynamics takes place due to the existence of the barrier in the $^1A^1$ state. If the NH stretching motion is excited, the ultrafast adiabatic population transfer occurs within 20 fs, see Fig. 6.14. Many details of the electronic population dynamics, *e.g.* the timescale of the population decay, the weak oscillation of the diabatic population and the branching ratio of the reaction, are consistent with the 2D calculations.

The branching ratio of the reaction is sensitive to the preparation of the dominant coupling mode ν_{11}. The diabatic population transfer at the conical intersection is enhanced by the excitation of this mode ν_{11}, see Fig. 6.14. On the other hand, the excitation of the weak coupling mode ν_{12} has almost no effect on the population dynamics, see Fig. 6.14. This result shows that the nonadiabatic transition at the conical intersection is primarily driven by the mode ν_{11}. The inclusion of the additional coupling mode ν_{12} has a minor effect on the electronic population dynamics. This result confirms the validity of the original 2D model for the $^2A_2$–S_0 conical intersection [93].

6.4.2.3 Comparison of 2D and 3D WP dynamics

Although the 2D and 3D calculations predict a similar electronic population dynamics for the $^1A_2$-S_0 conical intersection, the comparison of details of the WP dynamics provides additional insight into the multi-mode dynamics at this conical intersection. For the sake of illustration, we analyze the evolution of the WP for

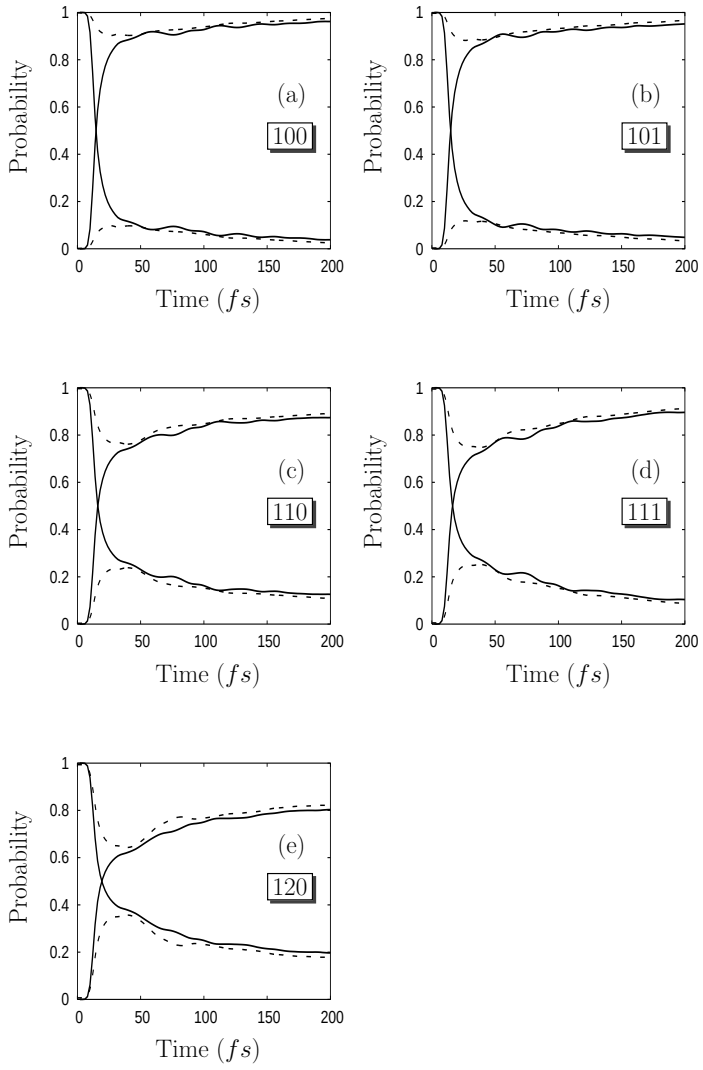

Figure 6.14: Time-dependent diabatic (dashed lines) and adiabatic (full lines) population probabilities of the $^1A_2$ and S_0 states for the initial states (100) (a), (101) (b), (110) (c), (111) (d), (120) (e).

the initial preparation in the (1,0) vibrational state in the 2D model and compare it with the WP dynamics for the (1,0,0) initial preparation in the 3D model. The probability densities of the 2D WPs are displayed as the absolute squares of the

projection of the nuclear WPs on the diabatic $^1A_2$ and S_0 states. For the 3D case, we define reduced probability densities for two vibrational modes by integration of the absolute square of the nuclear WPs over the third vibrational mode. The snapshots are taken at 20 fs after the preparation of the excited state.

Figs. 6.15 (a) and (b) shows the probability densities as functions of r and Q_{11} for the diabatic $^1A_2$ and S_0 states, respectively, for the 2D model. The WP, which has been prepared in the $^1A_2$ state at t=0 fs, has arrived at the conical intersection at 20 fs. The central part of the WP remains in the $^1A_2$ state, while the wing parts have preferentially been transferred to the S_0 state. Since the excitation of the coupling mode increases the extension of the WP along Q_{11}, the WP for $n_{c,1} > 0$ tends to follow the adiabatic surfaces rather than the diabatic surfaces. This explains the influence of the excitation of the coupling mode on the electronic population dynamics, which is clearly seen in Fig. 6.14. When the WP is transferred to the diabatic S_0 state, a nodal line is created at Q_{11}=0 by the $^1A_2$-S_0 conical intersection [see Fig. 6.15 (b)]. This reflects the fact that the diabatic coupling operator is an odd function of the coupling coordinate.

Figs. 6.15 (c) and (d) show the corresponding probability densities for the 3D model, as functions of r and Q_{11}. For the WP in the excited state, there is no obvious difference between the 2D and 3D results [Figs. 6.15 (a) and (c)], except that the 3D calculation yields a somewhat broader distribution of the probability density along the coupling coordinate. The snapshot of the WP in the ground state [Fig. 6.15 (b) and (d)], on the other hand, reveals a remarkable difference between the 2D and 3D calculations. In the 3D calculation, the reduced probability density at $Q_{11} = 0$ is not zero. The inclusion of the weak coupling mode thus modifies the symmetry properties of the WP as a function of the strong coupling mode.

In the adiabatic representation, the nonadiabatic coupling vector, which induces the nonadiabatic transition, is parallel to the direction of effective coupling mode displacement Q_{eff} [202] (see Chapter 2). In the diabatic representation, Q_{eff}, which is a linear combination of all Q_c, determines the population transfer between the two surfaces. This means that the projection of the WP on the

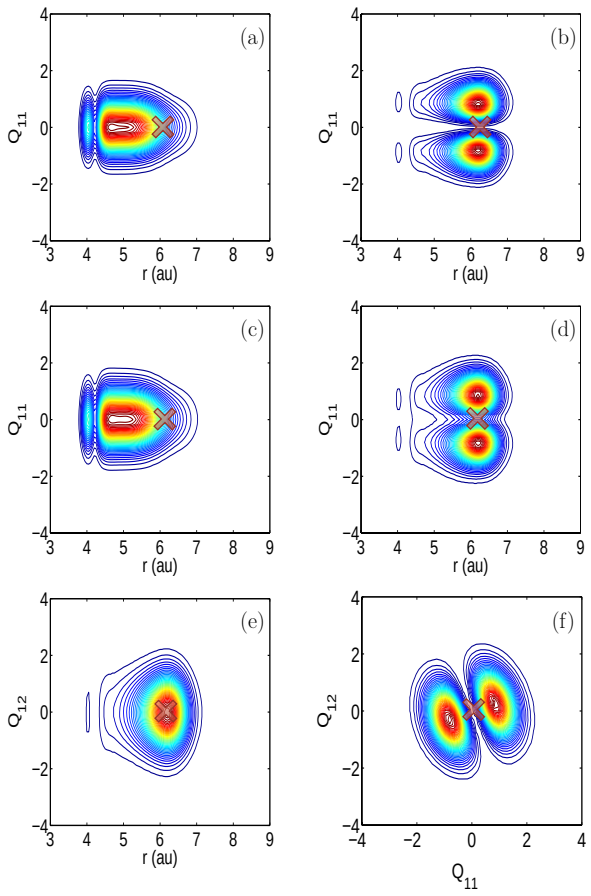

Figure 6.15: Snapshots of the probability density as a function of the NH stretching mode and one of the coupling modes at 20 fs: (a) Probability density as a function of r and Q_{11} of the $^1A_2$ state obtained for the 2D model; (b) Probability density as a function of r and Q_{11} in the S_0 state obtained for the 2D model; (c) Probability density as a function of r and Q_{11} in the diabatic $^1A_2$ state obtained for the 3D model; (d) Probability density as a function of r and Q_{11} for the diabatic S_0 state obtained for the 3D model; (e) Probability density as a function of r and Q_{12} in the diabatic S_0 state obtained for the 3D model; (f) Probability density as a function of Q_{11} and Q_{12} in the diabatic S_0 state obtained for the 3D model.

effective coupling coordinate exhibits a node structure of the WP like in the 2D case. In the present example, Q_{11} is the strong coupling coordinate, while the coupling of Q_{12} is rather weak. Q_{eff} therefore is quite close to Q_{11}, but the small contribution of Q_{12} leads to a deviation of the orientation of Q_{eff} from Q_{11}. This explains the blurring of the nodal structure of the probability density in Fig. 6.15 (d). As a complementary result, we show in Fig. 6.15 (e) the probability density in the diabatic ground state as a function of r and Q_{12} (the weak coupling mode). The density of Fig. 6.15 (e) is totally different from that of Fig. 6.15(d) and exhibits no node at all. Finally, Fig. 6.15 (f) shows the probability density in the diabatic ground state as a function of Q_{11} and Q_{12}. This figure exhibits the nodal line in the WP perpendicular to the effective coupling mode.

6.4.3 $^1B_1$–S_0 conical intersection

Since the coupling strength of ν_{21} and ν_{23} is negligible, it suffices to consider the strong coupling mode ν_{24} and the weak coupling mode ν_{22}, resulting in a 3D model for the $^1B_1$–S_0 conical intersection. Since the 2D calculations were based on a slightly different definition of the coupling mode, it is not useful to compare the present 3D results with these 2D results. We have repeated the 2D calculations, including the NH stretching motion and the strong coupling mode ν_{24}.

For the $^1B_1$–S_0 conical intersection, the diabatic frequencies $\omega_c^{(1)}$ and $\omega_c^{(2)}$ of Q_{22} do not depend on r_{NH}. The diabatic frequencies $\omega_c^{(1)}$ and $\omega_c^{(2)}$ of Q_{24}, on the other hand, decrease with increasing the NH coordinate. We have used the following function to represent the diabatic frequencies of Q_{24} as functions of r_{NH}:

$$\omega_c^{(i)}(r_{NH}) = \frac{1}{2}a_i \left[1 - \tanh\left(\frac{r_{NH} - b_1}{c_i}\right)\right] + d_i. \tag{6.22}$$

The previous calculations have already obtained the parameters for the tuning coordinate r_{NH}, see Table 6.7. Here, Table 6.11 give the values of all parameters related to the coupling modes in the $^1B_1$-S_0 model. Due to the very small contribution of ν_{21} and ν_{23} to the diabatic coupling element, they are not included in the tables. The average deviation between the fit and the *ab initio* data is 0.015 eV.

Table 6.11: Values of the parameters pertaining to the coupling modes for the $^1B_1$–S_0 model.

	ω		λ
Q_{22}	ω_c	$\omega_c = 0.0888$ eV	$\lambda_{12}^{max} = 0.0738$ eV
	$\omega_c^{(1)}$	$\omega_c^{(1)} = 0.0650$ eV	$d_{12} = 4.0728$ au
	$\omega_c^{(2)}$	$\omega_c^{(2)} = 0.1260$ eV	β_{12} =0.0910 au
			λ_0 =0.0 au
Q_{24}	ω_c	$\omega_c = 0.0640$ eV	$\lambda_{12}^{max} = 0.4269$ eV
	$\omega_c^{(1)}$	$a_1 = 0.0718$ eV	$d_{12} = 4.8319$ au
		$b_1 = 2.5805$ au	β_{12} =1.3225 au
		$c_1 = 1.4619$ au	λ_0 =0.0 au
		$d_1 = 0.0753$ au	
	$\omega_c^{(2)}$	$a_2 = 0.0718$ eV	
		$b_2 = 2.5805$ au	
		$c_2 = 1.4619$ au	
		$d_2 = 0.0143$ au	

6.4.3.1 Vibrational eigenstates of the electronic ground-state surface

The lowest vibrational levels of the 3D electronic ground-state surface of the $^1B_2$–S_0 conical intersection model have been calculated in the same way as for the $^1A_2 - S_0$ model. Again, n_r, $n_{c,1}$ and $n_{c,2}$ denote the occupation numbers of the NH stretching mode, the strongest coupling mode (ν_{24}) and the weak coupling mode (ν_{22}), respectively. The fundamental frequencies of these three vibrational motions are 3616 cm^{-1}, 471 cm^{-1} and 623 cm^{-1}, respectively, in the 3D model, in acceptable agreement with the experimental and full-dimensional harmonic values (see [85, 92] and references therein).

6.4.3.2 Electronic population and WP dynamics

The decay rate of the population of the $^1\pi\sigma^*$ state is again strongly dependent on the initial excitation of the NH stretching mode. Other than in the $^1A_2$-S_0 case, we observe two processes with distinctly different time-scales when the NH stretching mode is prepared in its ground state [(0,$n_{c,1}$,$n_{c,2}$) initial condition]. Both the diabatic and adiabatic pictures indicate a rapid population transfer from the excited state to the ground state during the early stage of the dynamics (about 15 fs), followed by a slow and monotonic decay (see Fig. 6.16). This two-timescale dynamics is the result of the existence of the barrier on the B_1 state. The reaction mechanism has been discussed in the previous 2D models. When the NH stretching mode is initially excited, that is for the (1, $n_{c,1}$, $n_{c,2}$) (Fig. 6.17) and (2, $n_{c,1}$, $n_{c,2}$) (not shown here) initial conditions, the WP reaches the conical intersection within 15 fs and the population transfer is essentially completed after 25 fs. In these cases, the initial WP has sufficient energy to overcome the barrier, reach the conical intersection and move towards to the two dissociation limits directly.

Figs. 6.16 and 6.17 show the electronic dynamics of the 3D $^1B_1$–S_0 conical-intersection model for various initial conditions. The initial vibrational state of the strong coupling mode (ν_{24}) has a large effect on the branching ratio of the reaction (see Figs. 6.16 and 6.17). Let us consider the (1, $n_{c,1}$, 0) initial condition as a typical example. The excitation of the strong coupling mode enhances the

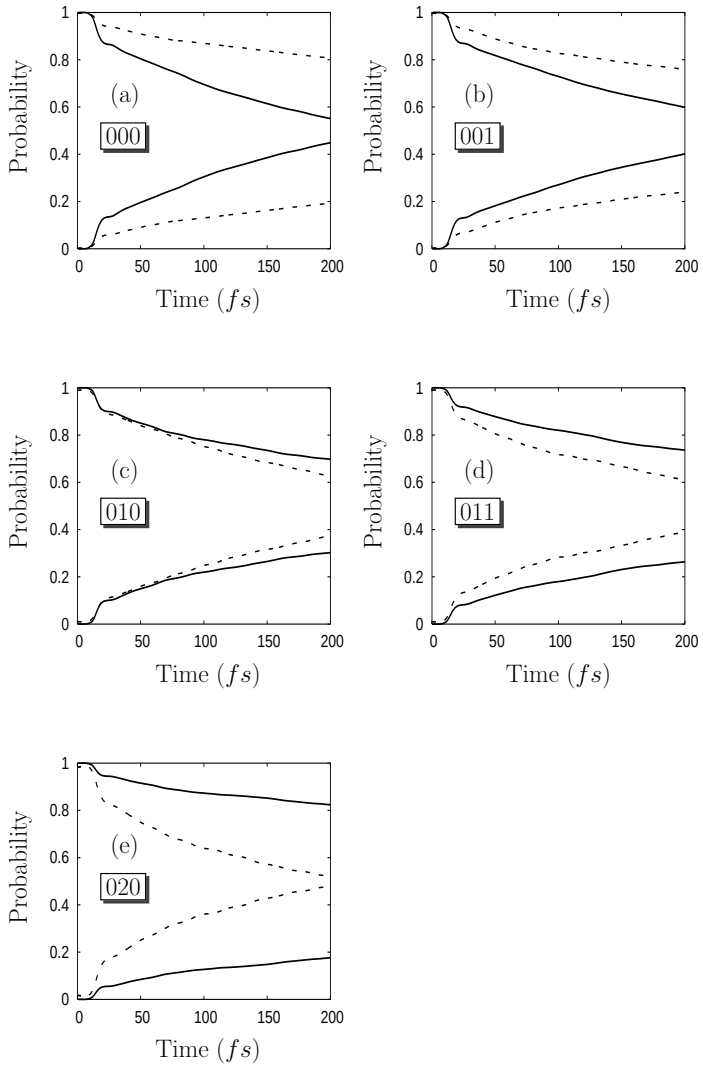

Figure 6.16: Diabatic (dashed lines) and adiabatic (full lines) population probabilities of the $^1B_1$ and S_0 states for the initial states (000), (001), (010), (011), (020).

probability of the adiabatic pathway from 30 % for $n_{c,1} = 0$ to almost 50 % for $n_{c,1} = 1$. The branching ratio saturates at about 70 % for $n_{c,1} = 2$. The excitation of the weak coupling mode, on the other hand, has a rather small effect on the population dynamics. The probability of the adiabatic channel increases by about

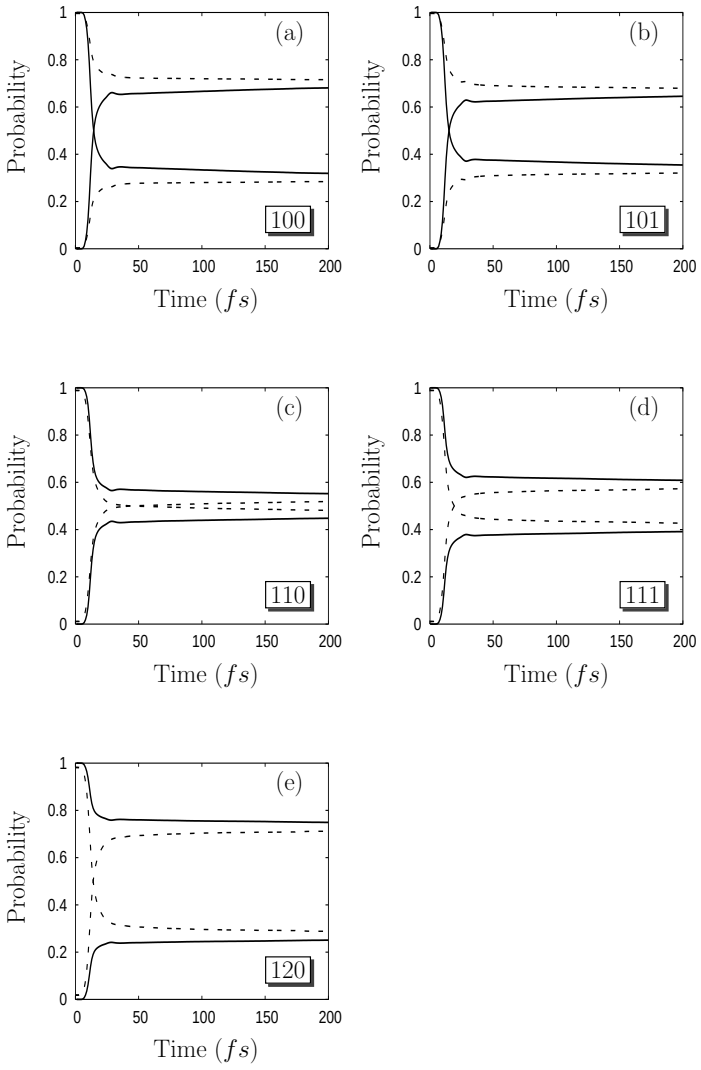

Figure 6.17: Diabatic (dashed lines) and adiabatic (full lines) population probabilities of the $^1B_1$ and S_0 states for the initial states (100), (101), (110), (111), (120).

5 % for the excitation of one quantum of ν_{22}.

As a result of the weak effect of ν_{22} on the nonadiabatic transition at the conical intersection, the calculations based on the 2D, 3D and effective-mode models provide rather similar population dynamics dynamics. These results can can be

analyzed in the same manner as discussed above by considering the orientation of Q_{eff}. Therefore, we do not repeat the detailed discussion of the probability densities here.

6.5 Summary

In order to understand the mechanistic details of the $^1\pi\sigma^*$ driven photochemistry of aromatic biomolecules, we have investigated the quantum WP dynamics of the $^1B_1$–S_0 and $^1A_2$–S_0 conical intersections of pyrrole. To characterize both of these conical intersections, we have performed the electronic structure calculations and determined the coupling strengths of all symmetry-allowed coupling modes. To capture the main feature of the nonadiabatic dynamics, we have constructed two-dimensional models which include the reaction coordinate (the NH stretching motion) and the strongest coupling coordinates. In order to understand the effect of additional vibrational modes on the $^1\pi\sigma^*$ driven photochemistry of pyrrole, we have investigated the nonadiabatic dynamics by using multidimensional models which include the reaction coordinate and two dominant coupling modes.

We have computed the adiabatic PE surfaces with the CASSCF method. A diabatic two-state Hamiltonian has been constructed for each conical intersection, employing an analytic *ansatz* for the diabatic PE matrix and a least-squares fit of the eigenvalues to *ab initio* data. The ultrafast dynamics has been investigated using standard time-dependent quantum WP propagation methods. We have calculated the branching ratio of the two dissociation channels (corresponding to the $^2\pi$ and $^2\sigma$ states of the pyrrolyl radical), for various initial vibrational levels of the electronic ground state.

The timescale of the photochemistry of pyrrole is extremely sensitive to the preparation of the initial state of the NH stretching mode. Photoexcited pyrrole does not exhibit sub-picosecond nonadiabatic dynamics when the NH stretching mode is in its ground vibrational level. However, the decay time of the population in the excited state is reduced to less than 50 fs when the NH stretching mode is excited. This acceleration of the nonradiative decay rate saturates at $n_r = 1$. These phenomena reflect the key role of the barrier of the NH stretching PE

function in the $^1\pi\sigma^*$ state of pyrrole.

The WP splits into two components at the conical intersection. The part of the WP which stays on the repulsive $^1\pi\sigma^*$ surface dissociates directly, while the remaining component is transferred to the S_0 diabatic state. The 2D calculations reveal that the branching ratio of the $^2\pi$ and $^2\sigma$ channels depends strongly on the initial excitation of the strongest coupling mode. With increasing quantum number of the coupling mode, the WP tends to follow the adiabatic path and dissociate towards the upper adiabatic limit.

The 3D calculations confirm that for both conical intersections the nonadiabatic dynamics is governed by the strongest coupling mode. Although the inclusion of the weak coupling mode leads to interesting changes of the nodal pattern of the WP at the conical intersection, it has little effect on the electronic population dynamics. This confirms that the two-mode models of the $^1A_2$–S_0 and $^1B_1$–S_0 conical intersections are quite useful for the qualitative understanding of the mechanisms of the photoinduced dynamics of pyrrole.

Both of the 2D and 3D models predict that the excitation of the strong coupling mode has a pronounced effect on the branching ratio of the photodissociation products. It should therefore be possible to control the photodissociation dynamics of pyrrole via the combination of IR and UV excitations, as has been demonstrated for ammonia recently [269–272].

We have visualized the details of the photodissociation dynamics via the conical intersections by the presentation of snapshots of the time-dependent WP. When the initial energy is high, the WP moves towards the two dissociation limits directly after passing through the conical intersection. If the initial energy is lower than the upper dissociation limit, on the other hand, part of the WP is trapped and has the possibility to enter the bound region of the S_0 surface. A pronounced multi-node structure in the NH stretching mode results. While the large excess energy in the NH stretching mode cannot be absorbed in the present two-mode model, it is known that this highly excited quasi-stationary state will be extremely susceptible to coupling with other vibrational degrees of freedom [64]. Thus, the system can be stabilized by rapid intramolecular energy

transfer from the active modes of the $^1\pi\sigma^*$–S_0 conical intersections to the remaining normal modes, resulting in internal conversion to the electronic ground state in competition with photodissociation. The quantum dissipative dynamics of pyrrole at the $^1\pi\sigma^*$–S_0 conical intersection is the topic of Chapter 8.

Chapter 7

Quantum dynamics of phenol

In this chapter, the time-dependent WP description of the photoinduced hydrogen elimination reaction in phenol *via* the conical intersections of the dissociative $^1\pi\sigma^*$ state with the $^1\pi\pi^*$ state and the electronic ground state is discussed. We have constructed a model including three intersecting electronic potential-energy surfaces (S_0, $^1\pi\sigma^*$, $^1\pi\pi^*$) and two nuclear degrees of freedom (OH stretching and OH torsion) based on the accurate *ab initio* multi-reference electronic-structure data. The nonadiabatic population-transfer dynamics at the conical intersections, the branching ratio between the two dissociation channels and their dependence on the initial preparation of the mode-specific vibrational levels have been investigated.

7.1 Theoretical framework

7.1.1 Reduced dimensional model

We wish to construct a simple model which describes the most essential aspects of the hydrogen-detachment photochemistry driven by the $^1\pi\sigma^*$ state in phenol. Previous studies have shown that the $^1\pi\sigma^*$ state is a dissociative state which crosses the ground state and the $^1\pi\pi^*$ state along the OH stretching coordinate, resulting in two conical intersections, S_0-$^1\pi\sigma^*$ and $^1\pi\sigma^*$-$^1\pi\pi^*$, respectively [83, 116–118]. Daigoku *et al.* [117] have shown that the dominant coupling coordinate

of the $^1\pi\pi^*$-$^1\pi\sigma^*$ conical intersection is the CCOH dihedral angle θ. We have found (see below) that θ also strongly couples the $^1\pi\sigma^*$ and S_0 states. Therefore, our model should include these two vibrational coordinates, the OH stretching coordinate, which tunes the energy gap between the different states, and the internal rotation of the OH group, which couples the three states in a pairwise manner. All other internal coordinates are kept frozen at their ground-state equilibrium values. The coupling of the two reaction coordinates with the many other vibrational modes may play a role in the actual photodissociation dynamics of phenol. It should be kept in mind that these effects are not included in the present model.

The molecular Hamiltonian is expressed in the three-state diabatic basis as

$$\hat{H} = \hat{T}_N \begin{pmatrix} 1 & 0 & 0 \\ 0 & 1 & 0 \\ 0 & 0 & 1 \end{pmatrix} + \begin{pmatrix} V_{11} & V_{12} & V_{13} \\ V_{21} & V_{22} & V_{23} \\ V_{31} & V_{32} & V_{33} \end{pmatrix}. \tag{7.1}$$

$\hat{T}_N$ is the nuclear kinetic-energy operator. V_{11}, V_{22} and V_{33} describe the PE surfaces of the diabatic electronic states, correlating with the ground diabatic S_0 state, the $^1\pi\sigma^*$ state and the $^1\pi\pi^*$ state, respectively. The off-diagonal elements describe the electronic couplings between the respective diabatic states. This PE matrix can be constructed by a diabatization procedure on the basis of the *ab initio* calculations, see below.

Following the method for the construction of the Hamiltonian of constrained systems, we have derived a reduced kinetic-energy operator in the two-dimensional space which is spanned by the OH distance r and the CCOH dihedral angle θ:

$$\hat{T}_N = -\frac{\hbar^2}{2\mu_{OH}}\frac{\partial^2}{\partial r^2} - \frac{\hbar^2}{2I}\frac{\partial^2}{\partial \theta^2}, \tag{7.2}$$

where μ_{OH} is the reduced mass of O and H,

$$\mu_{OH} = \frac{m_H m_O}{m_H + m_O}. \tag{7.3}$$

The moment of inertia I takes the form:

$$\frac{1}{I} = \frac{1}{I_1} + \frac{1}{I_2},$$

with

$$\begin{aligned} I_1 &= \mu_{OH}(r\sin\alpha)^2 \\ I_2 &= 4m_C[r_{CC}\sin(\frac{\pi}{3})]^2 + 4m_H[(r_{CC}+r_{CH})\sin(\frac{\pi}{3})]^2. \end{aligned} \tag{7.4}$$

The quantities m_H, m_O and m_C denote the masses of hydrogen, oxygen and carbon respectively. The CH (r_{CH}) and the CC (r_{CC}) bond distances are fixed at their ground-state equilibrium values. α is the angle between OH bond and OC bond at the ground-state equilibrium geometry.

7.1.2 *Ab initio* calculations

Similar to pyrrole, the $^1\pi\sigma^*$ state of phenol has 3s Rydberg character at the equilibrium geometry of the electronic ground state, but rapidly aquires H1s character along the dissociation path [83, 116, 117]. To account for the diffuseness of the σ^* orbital, it is necessary to use rather extended basis sets, in particular on the OH group. Throughout our calculations, the augmented correlation-consistent polarized valence double zeta (aug-cc-pVDZ) basis set [268] has been employed. One diffuse s function and one set of p functions were added to the oxygen and two diffuse s and two sets of diffuse p functions to the dissociative hydrogen atom. Their exponents were derived in an even-tempered manner from the most diffuse s and p functions already present in the aug-cc-pVDZ basis by dividing the exponents successively by a factor of 3.0.

As a reference for the definition of internal coordinate displacements, the ground-state equilibrium geometry has been optimized at the second-order Møller-Plesset (MP2) level using the GAUSSIAN 98 package [31]. The *ab initio* calculations of the PE surfaces of the S_0, $^1\pi\pi^*$ and $^1\pi\sigma^*$ states have been performed at the CASSCF level using the MOLPRO package [193]. The active space consists of one occupied σ orbital, the corresponding σ^* orbital and another σ^* orbital, as well as four π orbitals and three π^* orbitals. The inclusion of two σ^* orbitals turned out to be neccessary to obtain smooth PE curves of the $^1\pi\sigma^*$ surface in the region where the $^1\pi\sigma^*$ state changes character from 3s towards H1s. This active space corresponds to a distribution of 10 electrons in 10 orbitals.

In addition to the crossing with the $^1\pi\sigma^*$ state, the $^1\pi\pi^*$ state interacts with other higher excited states at large OH distances. This leads to convergence problems in the CASSCF calculations. However, these interactions occur at rather high energies and are not revelant for the reaction dynamics considered in this work. Thus, it is not considered necessary to include more excited states in our model. Since the $^1\pi\pi^*$ state is bound along the H dissociation coordinate, we can disregard it for large OH bond lengths. We thus have divided the computation of the PE surfaces into two parts. In the region of short OH distances (0.80 Å $< r <$ 1.30 Å, where r is the OH distance), which contains the $^1\pi\pi^*$-$^1\pi\sigma^*$ conical intersection, we average the CASSCF functional over three states. In the second region, ranging from $r = 1.60$ Å to $r = 5.0$ Å, we average over the $^1\pi\sigma^*$ and S_0 states only. In order to characterize both conical intersections in detail, we have computed the adiabatic PE surfaces on a very dense grid, varying the OH bond length with a step of 0.1 Å in the vicinity of the conical intersections. The CCOH dihedral angle has been varied from 0° to 90° in steps of 5°.

We also have calculated the DMs of the different adiabatic electronic states and the TDMs between them. When discussing these vectors, we refer to the Cartesian coordinate system shown in Fig. 7.1. The benzene ring is fixed in the

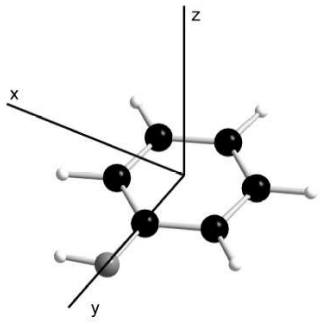

Figure 7.1: Definition of the Cartesian coordinate system.

x-y plane, and the center of this ring is chosen as the origin of the coordinate system. The y axis is oriented along the CO bond.

7.1.3 Diabatic potential surfaces

In this subsection, we construct the diabatic PE matrix based on the diabatization methods descirbed in Chapter 2.

In the present rather transparent case of two conical intersections, arising from the symmetry-allowed crossing of the $^1\pi\sigma^*$ state of A" symmetry with the $^1\pi\pi^*$ and S_0 states of A' symmetry in the C_s point group, we have achieved the diabatization via the ansatz of a 3×3 PE matrix as an analytic function of the nuclear coordinates. The diagonal elements of this diabatic matrix denote the energies of S_0, $^1\pi\sigma^*$ and $^1\pi\pi^*$ states. The offdiagonal elements reflect the diabatic coupling between them. The parameters of the ansatz are determined by a least-squares fit of the eigenvalues of the PE matrix to the *ab initio* PE data. Since only PE data are used for the construction of the diabatic model, the smoothness of DMs and TDMs in the diabatic representation is an independent test of the performance of the diabatization procedure.

The choice of suitable analytic PE functions is inspired by the work on pyrrole (Chapter 6). The diabatic S_0 PE function is approximated by a Morse-type function in the OH stretch direction and a cosine function in the angular coordinate θ:

$$V_{11}(r,\theta) = v_{10}(r) + v_{11}(r)[1-\cos(2\theta)], \tag{7.5}$$

where

$$v_{10}(r) = D_e^1 \left[1-\exp\left(-a_1(r-r_1)\right)\right]^2, \tag{7.6}$$

$$v_{11}(r) = \frac{1}{2}A_1\left[1-\tanh\left(\frac{r-A_2}{A_3}\right)\right]. \tag{7.7}$$

The diabatic PE function of the $^1\pi\sigma^*$ state is approximated as follows:

$$V_{22}(r,\theta) = v_{20}(r) + v_{21}(r)[1-\cos(2\theta)] + v_{22}(r)[1-\cos(2\theta)]^2, \tag{7.8}$$

where

$$v_{20}(r) = \frac{1}{2}(v_{201}(r)+v_{202}(r)) - \frac{1}{2}\sqrt{(v_{201}(r)-v_{v202}(r))^2+\chi_{20}}, \tag{7.9}$$

$$v_{21}(r) = \frac{1}{2}(v_{211}(r)+v_{212}(r)) + \frac{1}{2}\sqrt{(v_{211}(r)-v_{v212}(r))^2+\chi_{21}}, \tag{7.10}$$

$$v_{22}(r) = \frac{1}{2}(v_{221}(r)+v_{v222}(r)) - \frac{1}{2}\sqrt{(v_{221}(r)-v_{222}(r))^2+\chi_{22}}, \tag{7.11}$$

with

$$v_{201}(r) = B_{201}[1-\exp(-B_{202}(r-B_{203}))]^2 + B_{204}, \quad (7.12)$$

$$v_{202}(r) = B_{205}\exp(-B_{206}(r-B_{207})) + B_{208}, \quad (7.13)$$

$$v_{211}(r) = \frac{1}{2}B_{211}[1-\tanh(\frac{r-B_{212}}{B_{213}})], \quad (7.14)$$

$$v_{212}(r) = \frac{1}{2}B_{214}[1-\tanh(\frac{r-B_{215}}{B_{216}})] + B_{217}, \quad (7.15)$$

$$v_{221}(r) = \frac{1}{2}B_{221}[1+\tanh(\frac{r-B_{222}}{B_{223}})], \quad (7.16)$$

$$v_{222}(r) = \frac{1}{2}B_{224}[1-\tanh(\frac{r-B_{225}}{B_{226}})]. \quad (7.17)$$

Similar to the ground diabatic S_0 state, the diabatic PE function of the $^1\pi\pi^*$ state is described by

$$V_{33}(r,\theta) = v_{30}(r) + v_{31}(r)[1-\cos(2\theta)], \quad (7.18)$$

where

$$v_{30}(r) = D_e^3\left[1-\exp\left(-a_3(r-r_3)\right)\right]^2 + a_{30}, \quad (7.19)$$

$$v_{31}(r) = \frac{1}{2}C_1\left[1-\tanh\left(\frac{r-C_2}{C_3}\right)\right]. \quad (7.20)$$

The electronic coupling terms, which have to vanish at $\theta = 0$, are written as sine functions of the angular coordinate θ:

$$V_{12}(r,\theta) = \lambda_{12}(r)\sin\theta, \quad (7.21)$$

$$V_{23}(r,\theta) = \lambda_{23}(r)\sin\theta, \quad (7.22)$$

with

$$\lambda_{12}(r) = \lambda_{21}(r) = \frac{1}{2}\lambda_{12,max}\left[1-\tanh\left(\frac{r-d_{12}}{\beta_{12}}\right)\right], \quad (7.23)$$

$$\lambda_{23}(r) = \lambda_{32}(r) = \frac{1}{2}\lambda_{23,max}\left[1-\tanh\left(\frac{r-d_{23}}{\beta_{23}}\right)\right]. \quad (7.24)$$

There is no coupling between the diabatic ground S_0 state and the $^1\pi\pi^*$ state, therefore $V_{13} = 0$.

Next, the non-square fitting was performed to get all parameters in the diabatic model and this procedure is done in three steps.

Table 7.1: Numerical values of the parameters of V_{11}.

v_{10}	v_{11}
$D_e^1 = 4.26302$ eV	$A_1 = 0.27037$ eV
$r_1 = 0.96994$ Å	$A_2 = 1.96606$ Å
$a_1 = 2.66021$ Å^{-1}	$A_3 = 0.685264$ Å

(1) We have selected the one-dimensional cuts of the PE surfaces for $\theta = 0$, which directly provide the the r-dependent functions $v_{10}(r)$, $v_{20}(r)$ and $v_{30}(r)$, respectively. The parameters related to $v_{10}(r)$, $v_{20}(r)$ and $v_{30}(r)$ have been obtained by three separate fittings.

(2) We have focused our attention on the region $r > 1.65$ Å, where only two electronic states, $^1\pi\sigma^*$ and S_0, are relevant. The potential matrix $\mathbf{V}$ becomes a 2×2 matrix and the eigenvalues are given analytically. At the $^1\pi\sigma^*$-S_0 conical intersection, we fix the bond distance and select one-dimensional PE cuts along θ to derive the values of $v_{11}(r_{CI,2})$, $v_{21}(r_{CI,2})$, $v_{22}(r_{CI,2})$ and $\lambda_{12}(r_{CI,2})$. A series of one-dimensional PE functions for different OH bond distances (r) determine $v_{11}(r)$, $v_{21}(r)$, $v_{22}(r)$ and $\lambda_{12}(r)$. We have found a suitable r-dependent function to fit $\lambda_{12}(r)$ and to obtain the parameters $\lambda_{12,max}$, d_{12} and β_{12} in Eq. 7.23. Afterwards, we extrapolate this function to the small r region, where three states are involved.

(3) For $r < 1.65$ Å, we have performed a nonlinear fitting for three electronic states. Starting from the $^1\pi\pi^*$-$^1\pi\sigma^*$ conical intersection, we have selected one-dimensional three-state PE cuts along θ to determine the values of $v_{11}(r_{CI,1})$, $v_{21}(r_{CI,1})$, $v_{22}(r_{CI,1})$, $v_{31}(r_{CI,1})$ and $\lambda_{23}(r_{CI,1})$. Several cuts of the PE surfaces for different r have been employed to determine the r dependence of $v_{11}(r)$, $v_{21}(r)$, $v_{22}(r)$, $v_{31}(r)$ and $\lambda_{23}(r)$. Finally, it is necessary to combine the results in the two different regions to obtain the parameters appearing in the expressions of $v_{11}(r)$, $v_{21}(r)$ and $v_{22}(r)$.

Tables 7.1–7.4 give the parameters of the diabatic model. The average and maximum deviation between adiabatic model PE surfaces and the *ab initio* data is 0.03 eV and 0.08 eV respectively.

Table 7.2: Numerical values of the parameters of V_{22}.

v_{20}	v_{21}	v_{22}
$B_{201} = 0.192205$ eV	$B_{211} = -0.2902$ eV	$B_{221} = 27.3756$ eV
$B_{202} = 5.67356$ Å^{-1}	$B_{212} = 2.05715$ Å	$B_{222} = 1.66881$ Å
$B_{203} = 1.03171$ Å	$B_{213} = 1.01574$ Å	$B_{223} = 0.20557$ Å
$B_{204} = 5.50696$ eV	$B_{214} = -73.329$ eV	$B_{224} = 0.35567$ Å
$B_{205} = 4.70601$ eV	$B_{215} = 1.48285$ Å	$B_{225} = 1.43492$ eV
$B_{206} = 2.49826$ Å^{-1}	$B_{216} = -0.1111$ Å	$B_{226} = 0.56968$ Å
$B_{207} = 0.988188$ Å	$B_{217} = -0.00055$ eV	$\chi_{22} = 0.00$ eV^2
$B_{208} = 3.3257$ eV	$\chi_{21} = 0.021105$ eV^2	
$\chi_{20} = 0.326432$ eV^2		

Table 7.3: Numerical values of the parameters of V_{33}.

v_{30}	v_{31}
$D_e^3 = 4.47382$ eV	$C_1 = 0.110336$ eV
$r_3 = 0.96304$ Å	$C_2 = 1.21724$ Å
$a_3 = 2.38671$ Å^{-1}	$C_3 = 0.06778$ Å
$a_{30} = 4.85842$ eV	

Table 7.4: Numerical values of the parameters of V_{12} and V_{23}.

V_{12}	V_{23}
$\lambda_{12,max} = 1.47613$ eV	$\lambda_{23,max} = 0.327204$ eV
$d_{12} = 1.96984$ Å	$d_{23} = 1.22594$ Å
$\beta_{12} = 0.494373$ Å	$\beta_{23} = 0.0700604$ Å

7.1.4 Wave-packet propagation

The photoinduced dynamics of phenol is treated in the time-dependent picture by solving the Schödinger equation on a two dimensional grid. The basic principles are given in Chapter 3.

First of all, we generate the vibrational eigenstates of the adiabatic ground-state PE surface by using the pseudo-spectral method. In this calculation, the grid consists of 100×80 points, ranging from 1 au to 8 au along r and $-\pi$ rad to π rad along θ respectively. This grid is large enough to ensure that the wave function does not reach the grid boundaries during the propagation. The total propagation time is 2.0 ps with a time step $\Delta t = 0.1$ fs. No damping function was employed in this calculation. The starting Gaussian WP was defined as:

$$\Psi(t=0) = \mathcal{N} \exp\left[-\frac{(r-r_0)^2}{2\sigma_r^2}\right] \times \exp\left[-\frac{(\theta-\theta_0)^2}{2\sigma_\theta^2}\right], \tag{7.25}$$

where $\mathcal{N}$ is the normalization constant. The parameters are chosen such that this WP is initially shifted ($r_0 = 2.3$ au, $\theta_0 = 0.6$ rad) with respect to the ground-state equilibrium geometry ($r_0 = 1.81$ au, $\theta = 0$) by $\sigma_r = 0.3$ au and $\sigma_\theta = 0.2$ au along r and θ, respectively.

Initial WPs are then prepared by vertical electronic excitation, starting from different vibrational states in the electronic ground state.

The WPs are propagated on the three coupled surfaces using the split-operator method. We employ the FFT method to evaluate the propagator of the nuclear kinetic-energy operator. The grid for the excited-state WP propagation consists of 400 points in the r coordinate from 1.0 au to 27.212 au and 80 points in θ from $-\pi$ rad to π rad. The WPs are propagated for 200 fs with a time step 0.1 fs. The total propagation time is long enough to ensure that the population probabilities of the different dissociation channels are converged. To avoid the reflection at the grid boundary in the r direction, we activate the damping function from $r_{mask} = 25$ au.

The time dependence of the diabatic electronic population probabilities is calculated to exhibit the population transfer between different electronic states. The dissociation probability is defined as the time-accumulated flux through a

dividing surface located at $r_{flux} = 20$ au, which is placed beyond the conical intersections.

7.2 Results and discussion

7.2.1 Potential-energy surfaces and dipole moments

The MP2 ground-state equilibrium structure compares well with that obtained in previous studies at different levels [107, 110–114, 117]. Our CASSCF calculations yield $^1\pi\pi^*$ and $^1\pi\sigma^*$ vertical excitation energies of 4.85 eV and 5.44 eV, respectively. These values are in the range of values reported in previous theoretical studies at different levels [107, 111, 113, 116, 117].

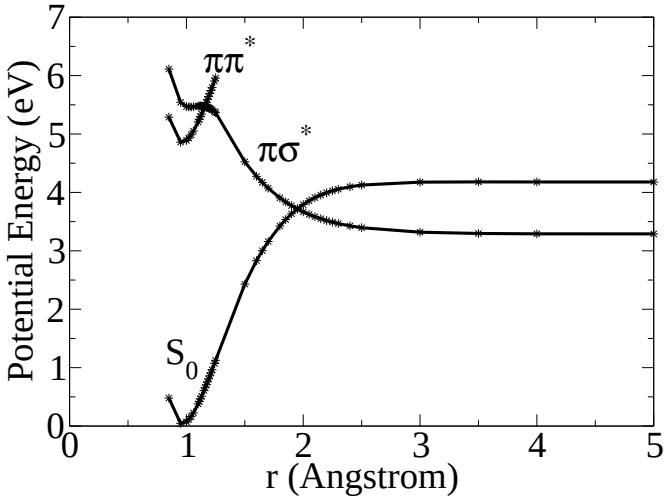

Figure 7.2: PE profiles of the electronic ground state, the $^1\pi\sigma^*$ state and the lowest $^1\pi\pi^*$ state as functions of OH stretching coordinate r for planar phenol.

The PE functions of phenol along the OH stretching coordinate r are displayed in Fig. 7.2. The equilibrium bond length of the $^1\pi\pi^*$ state ($r = 0.96$ Å) essentially coincides with that of the ground state. The PE functions of the ground state and the $^1\pi\pi^*$ state rise in a nearly parallel way with increasing OH distance.

The dissociative $^1\pi\sigma^*$ PE function crosses the $^1\pi\pi^*$ PE function at 1.16 Å and the ground-state function at 1.96 Å, thus creating two conical intersections. The energy function of the $^1\pi\sigma^*$ state is rather flat between 1.0 Å and 1.3 Å, reflecting the change of the character of the σ^* orbital. In contrast to pyrrole [89, 93], the $^1\pi\sigma^*$ PE function of phenol exhibits no barrier.

The two-dimensional diabatic model PE surfaces (diagonal elements of $\mathbf{V}_d$), as well as inter-state couplings (offdiagonal elements of $\mathbf{V}_d$) are displayed as functions of the coordinates r and θ in Figs. 7.3 (a) and (b), respectively. It is

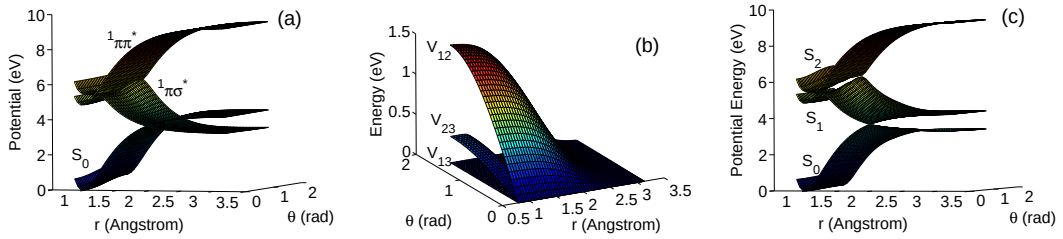

Figure 7.3: Diabatic energy potential surfaces (a), diabatic coupling terms (b) and adiabatic energy surfaces (c) as the functions of the OH stretching coordinate r and the CCOH dihedral angle θ.

seen that the three diabatic energy surfaces are smooth functions of the nuclear coordinates. The coupling elements, which are odd functions of θ, slowly decrease with increasing OH bond distance. Fig. 7.3 (c) shows the adiabatic PE surfaces in the two-dimensional space. The two conical intersections are clearly visible. The diabatic PE surfaces, as well as the coupling elements, are non-separable functions of r and θ. The adiabatic PE functions acquire an additional pronounced non-separability of the two coordinates through the two conical intersections.

The behavior of the DMs and TDMs directly reflects the character of the electronic wavefunctions. We discuss here, for the sake of illustration, the x-components (see Fig. 7.1 for the description of the coordinate system) of the DM and TDM vectors. Fig. 7.4 (a) displays the adiabatic TDMs, μ^x_{12} (for the S_0-S_1 transition) and μ^x_{13} (for the S_0-S_2 transition), in the range of the three-state-averaged CASSCF calculation (0.85 Å $< r <$ 1.25 Å). It is seen that the adiabatic TDM functions are rapidly varying functions of the nuclear geometry in

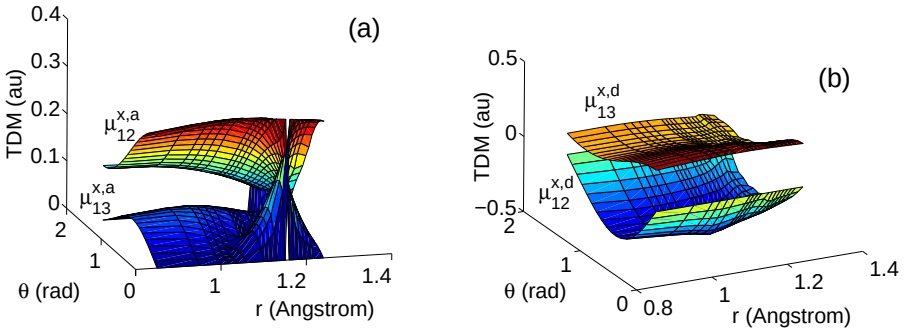

Figure 7.4: Transition dipole moments μ_{12}^x and μ_{13}^x in the adiabatic representation (a) and diabatic representation (b) as functions of the OH stretching coordinate r and the CCOH dihedral angle θ.

the vicinity of the first conical intersection. This reflects the rapid changes of the adiabatic electronic wavefuntions at this conical intersection. On the other hand, as shown in Fig. 7.4 (b), the diabatic TDMs, μ_{12}^x (for the S_0-$^1\pi\sigma^*$ transition) and μ_{13}^x (for the S_0-$^1\pi\pi^*$ transition), are smoothly varying functions of the nuclear coordinates. The rapid jumps at the conical intersection have disappeared in the diabatic TDMs. Fig. 7.4 (b) also shows that $\mu_{12}^x = 0$ when the molecule is in the planar configuration, but becomes nonzero for nonplanar geometries.

Fig. 7.5 (a) and Fig. 7.5 (b) show the DMs of the ground state and the $^1\pi\sigma^*$ state in the adiabatic and diabatic representations, respectively, in the nuclear-coordinate range 1.60 Å $< r <$ 5.0 Å. The rapid changes of the adiabatic DMs

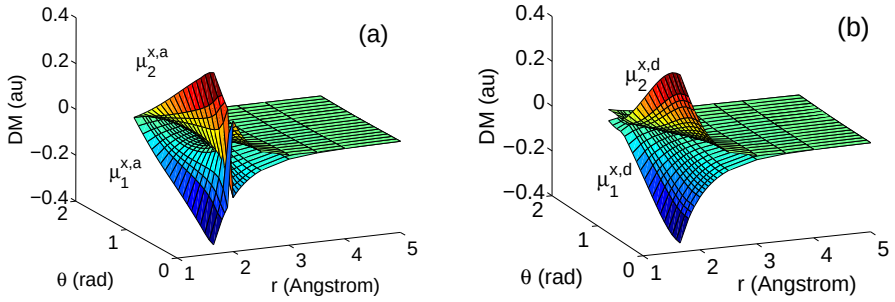

Figure 7.5: Dipole moments of two lowest adiabatic (a) and diabatic (b) states as functions of the OH stretching coordinate r and the CCOH dihedral angle θ.

Table 7.5: Eigenvalues (E_n) and assignments (n_r, n_θ) of the pseudospectral peaks of the adiabatic ground state

$E_n(\mathrm{cm}^{-1})$	(n_r, n_θ)	$E_n(\mathrm{cm}^{-1})$	(n_r, n_θ)	$E_n(\mathrm{cm}^{-1})$	(n_r, n_θ)
2202	(0,0)	6113	(1,0)	9774	(2,0)
2468	(0,1)	6354	(1,1)	9982	(2,1)
2702	(0,2)	6579	(1,2)	10174	(2,2)

reflect the position of the $^1\pi\sigma^*$-S_0 conical intersection. The diabatic DMs are seen to be smoothly varying functions of the nuclear geometry. The adiabatic and diabatic DMs in the x direction of the two-dimensional adiabatic ground-state surface vanish by symmetry for $r \to \infty$ and $\theta = \frac{\pi}{2}$.

Summarizing, the smooth behavior of the diabatic DMs and TDMs, obtained by the adiabatic-to-diabatic transformation, indicates that the diabatization procedure is physically meaningful and that the diabatic model captures the main features the two conical intersections.

7.2.2 Vibrational states of the electronic ground-state surface

The energy eigenvalues of the nine lowest vibrational states of the two-dimensional adiabatic electronic ground-state surface and their assignments in terms of quantum numbers are given in Table 7.5. The eigenstates are assigned by examining the nodal pattern in their eigenfunctions calculated by the spectral quantization technique. The quantities n_r and n_θ in Table 7.5 refer to the number of nodes in the corresponding eigenfunction along the OH stretching coordinate r and torsional coordinate θ, respectively. We choose the wavefunctions of the torsional mode to be localized in the well around $\theta = 0$. The second well at $\theta = \pi$ plays no role for the ultrafast photodissociation dynamics of phenol if the initial excitation of the torsional mode is weak ($n_\theta \leq 3$). The fundamental frequency of the stretching mode is obtained as 3911 cm^{-1}. The fundamental of the coupling mode is 266 cm^{-1}. The experimental values (see [104,110,111,273] and references

therein) of the fundamentals of the OH-stretching and out-of-plane OH bending modes are 3656 cm^{-1} and 309 cm^{-1}, respectively. Our two-dimensional adiabatic model surface reproduces these values with reasonable accuracy.

7.2.3 Electronic population dynamics

To explore the effect of specific initial vibrational excitations on the subsequent photodissociation dynamics, we have propagated different initial wavefunctions, which are generated by placing the 9 lowest vibrational eigenfunctions of the electronic ground state vertically into the $^1\pi\pi^*$ state.

We first discuss the electronic population dynamics to elucidate the population transfer between different electronic state induced by the conical intersections. Here, we focus on the population dynamics of the diabatic electronic states, although both diabatic and adiabatic electronic populations have been calculated. Due to the two successive nonadiabatic transitions through conical intersections, the diabatic electronic population probabilities provide a more transparent picture than the adiabatic populations.

When the OH stretching mode is prepared in its ground state, that is, for the three initial conditions (0,0), (0,1) and (0,2), no visible electronic population dynamics takes place within 200fs (figures not shown). The population of the diabatic $^1\pi\sigma^*$ state is not exactly zero but small (less than 5 %) and no population transfer from the $^1\pi\pi^*$ state to the $^1\pi\sigma^*$ state is observed. This small population of the diabatic $^1\pi\sigma^*$ state results from the nonvanishing mixing of the $^1\pi\pi^*$ and $^1\pi\sigma^*$ states in the Franck-Condon region. The absence of a fast decay of the population of the $^1\pi\pi^*$ state after the preparation of the vibrational ground state of the OH stretching mode can be understood by the inspection of the $^1\pi\pi^*$-$^1\pi\sigma^*$ conical intersection (see Fig. 7.2 and 7.3 (c)). The lower cone of S_1-S_2 conical intersection creates a barrier of 0.8 eV on the S_1 surface in the OH direction. In addition, the well of the $^1\pi\pi^*$ state is very similar to that of the ground state, implying that there are no Franck-Condon transitions to higher vibrational levels of the $^1\pi\pi^*$ state. The energies of the initial states prepared from the (0,0), (0,1) and (0,2) ground-state levels are lower than the barrier on the S_1 surface. There-

fore, the WPs are trapped in the well of the $^1\pi\pi^*$ state and electronic population transfer at the first conical intersection can only be achieved by quantum tunnelling, which takes place on a rather long timescale. This is consistent with the observation that the lifetime of the lowest vibronic level of the S_1 state of phenol (2 ns) is considerably shorter than the corresponding lifetime in deuterated phenol (16 ns) [96, 129, 130].

If we put one quantum of energy into the OH stretching mode, the energies of the initial WPs generated from the (1,0), (1,1) and (1,2) ground-state levels exceed the energy of the S_1-S_2 conical intersection, and a fast population transfer between the $^1\pi\pi^*$ and $^1\pi\sigma^*$ states is observed. As can be seen from

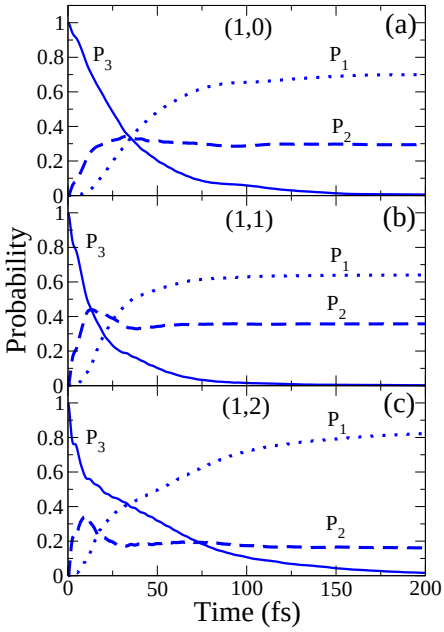

Figure 7.6: Population probabilities of the diabatic states; P_1: the ground state (dotted lines), P_2: the $^1\pi\sigma^*$ state (dashed lines), and P_3: the $^1\pi\pi^*$ state (full lines), for the initial conditions (1,0) (a), (1,1) (b) and (1,2) (c).

Figs. 7.6 (a), (b) and (c), corresponding to the (1,0), (1,1) and (1,2) initial conditions, respectively, we obtain a rapid and essentially monotonic decay of the population of the $^1\pi\pi^*$ diabatic state (P_3). It should be noted that the population

of the diabatic ground state (P_1) begins to rise in the early stage of the dynamics, after $\approx$ 10 fs. This implies that parts of the WPs reach the second conical intersection very quickly, as a consequence of the strongly repulsive character of the $^1\pi\sigma^*$ state. The WPs split at the second intersection, and move towards two different dissociation channels (S_0 and $^1\pi\sigma^*$). After 100 fs, the population dynamics is essentially finished. The asymptotic ($t \to \infty$) dissociation probabilities on the S_0 and $^1\pi\sigma^*$ states are shown in Fig. 7.7. Fig. 7.6 and Fig. 7.7 reveal that initial excitations of the coupling mode have a noticeable effect on the lifetime of the $^1\pi\pi^*$ state and the branching ratio of the two dissociation channels. We observe an interesting odd-even effect with respect to the occupation number of the coupling mode. When an odd number of quanta is put into the coupling mode ((1,1)), the population of the $^1\pi\pi^*$ state decays faster than with an even number of quanta of the coupling mode ((1,0) and (1,2)). In addition, dissociation towards the lower ($^1\pi\sigma^*$) dissociation channel is enhanced when the initial state contains an odd number of quanta in the coupling mode, see Fig. 7.7. We

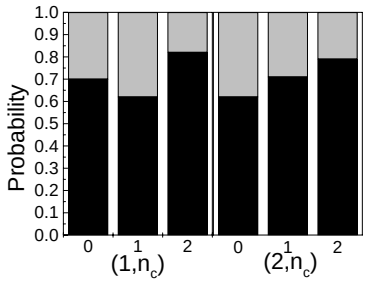

Figure 7.7: Dissociation probabilities of the upper (black) and lower (grey) adiabatic limits.

call this phenomenon the "odd-even" effect. A similar effect was noted before by Baer *et al.* in their discussions of the state-to-state transition probabilities within a quasi-Jahn-Teller model [274].

If we put two quanta into the OH stretching mode, that is, (2,0), (2,1) and (2,2) initial conditions, we observe a similarly fast decay of the population of the $^1\pi\pi^*$ state, see Fig. 7.8. The odd-even effect disappears. Instead, the lifetime of the diabatic $^1\pi\pi^*$ state decreases monotonically with increasing the energy in

the coupling mode (see Fig. 7.8). Likewise, the dissociation probability to the

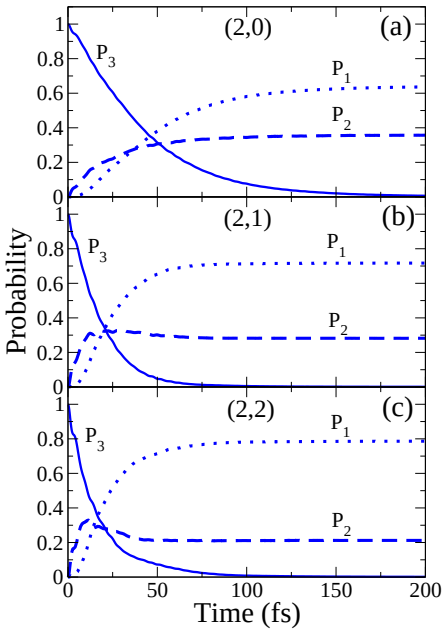

Figure 7.8: Population probabilities of the diabatic states; P_1: the ground state (dotted lines), P_2: the $^1\pi\sigma^*$ state (dashed lines), and the P_3: $^1\pi\pi^*$ state (full lines), for the initial conditions (2,0) (a), (2,1) (b) and (2,2) (c).

lower ($^1\pi\sigma^*$) dissociation limit decreases monotonically with the excitation of the coupling mode, see Fig. 7.7.

The timescale of the photochemistry of phenol is thus extremely sensitive to the initial state of the OH stretching mode. While the $S_1(^1\pi\pi^*)$ excited state exhibit no sub-picosecond nonadiabatic dynamics when the OH stretching mode is in its ground vibrational level, the $^1\pi\pi^*$ state decays in less than 50 fs when one quantum of the OH stretching mode is excited (see Fig. 7.6). The acceleration of the nonradiative decay already saturates at $n_r = 1$; preparation of the $n_r = 2$ level does not lead to a significant enhancement of the decay rate (see Fig. 7.8). This saturation of the decay rate at the energy of the conical intersection has been predicted many years ago by Sobolewski in the framework of the statistical theory of radiationless transitions [275]. The initial excitation of the torsional

mode, on the other hand, has a moderate impact on the decay rates and the branching ratio for dissociation into the $^2\pi$ and $^2\sigma$ states of the phenoxyl radical, see Fig. 7.6 - 7.7. At least within the present model of limited dimensionality, the photodissociation dynamics of OH stretching excited phenol via the repulsive $^1\pi\sigma^*$ state is an ultrafast and highly coherent process which is suitable for efficient control by laser fields.

We also have checked the validity of the Condon approximation by taking the dependence of the diabatic TDMs on the nuclear geometry into account. Among all TDM elements, only μ^x_{13} is nonzero when $\theta = 0$. This means that μ^x_{13} plays the most important role for the laser excitation. Since μ^x_{13} depends only weakly on the nuclear coordinates in the Franck-Condon region, the corrections to the Condon approximation are found to be negligible. The Condon approximation thus is well justified in the present case and we have used it throughout our calculations.

7.2.4 Time-dependent wave packets

In this section, we shall provide a detailed picture of the nuclear WPs in the $^1\pi\pi^*$, $^1\pi\sigma^*$ and S_0 diabatic states which evolve after preparation of the (1,0), (1,1) and (1,2) initial states. Since the initial location of the WP, the $^1\pi\pi^*$-$^1\pi\sigma^*$ and the $^1\pi\sigma^*$-S_0 conical intersections lie in a line (all three correspond to planar configuration of phenol), the system has interesting symmetry properties. These symmetry properties are revealed by snapshots of the WPs in the three electronic states at suitable times.

7.2.4.1 The $^1\pi\pi^*$-$^1\pi\sigma^*$ conical intersection

Let us start with the (1,0) initial condition. Fig. 7.9 shows the absolute square of projection of the WP on the $^1\pi\pi^*$, $^1\pi\sigma^*$ and diabatic S_0 states at 30 fs respectively. The locations of the two conical intersections are indicated by the crosses. After the initial WP has been prepared by the vertical excitation, the shape of its projection on the $^1\pi\pi^*$ state does not change during the first 30 fs, reflecting the absence of a Frank-Condon shift of the $^1\pi\pi^*$ state. Throughout the whole process,

the $^1\pi\pi^*$ component of the density (see Fig. 7.9 (a)) remains spatially localized in the well of the $^1\pi\pi^*$ state. The node of the wavefunction in the OH stretching direction is clearly visible. The $^1\pi\pi^*$ density decays as a result of the the fast population transfer at the first conical intersection. A snapshot of the absolute square of the wavefunction in the $^1\pi\sigma^*$ state at 30 fs is shown in Fig. 7.9 (b). It is seen that the node in the OH stretching direction has disappeared, while a nodal line at $\theta = 0$ has been generated by the $^1\pi\pi^*$-$^1\pi\sigma^*$ conical intersection. The latter node is a necessary consequence of the fact that the diabatic coupling operator is an odd function of θ. In the adiabatic picture, the nodal line at $\theta = 0$ reflects the so-called Berry phase of the nuclear wavefunction. The two parts of the wavefuntion move around the $^1\pi\pi^*$-$^1\pi\sigma^*$ conical intersection along two different adiabatic paths (clockwise or anti-clockwise), and interfere destructively at $\theta = 0$.

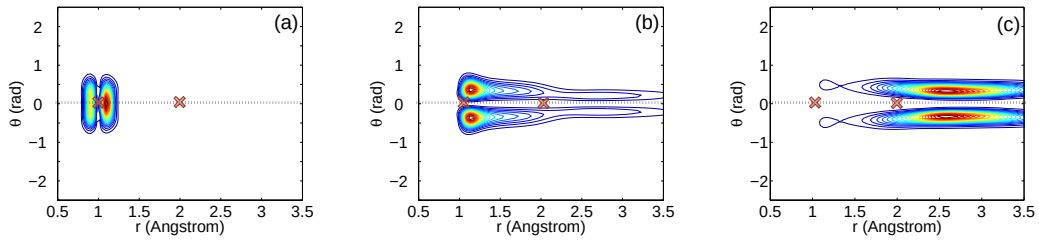

Figure 7.9: Snapshots of the probability density in the diabatic $^1\pi\pi^*$ state at 30 fs (a), the diabatic $^1\pi\sigma^*$ state at 30 fs (b) and the diabatic ground state at 30 fs (c), for the (1,0) initial condition. The crosses indicate the locations of the two conical intersections.

For the (1,1) initial condition, the WP in $^1\pi\pi^*$ state possesses two nodal lines. This feature is still present at 20 fs, as shown in Fig. 7.10 (a). Fig. 7.10 (b) reveals that both nodal lines have disappeared in the $^1\pi\sigma^*$ state. While the initial WP placed in the $^1\pi\pi^*$ state was an antisymmetric function of θ, we have a symmetric wavefunction in the $^1\pi\sigma^*$ state.

Fig. 7.11 (a) and Fig. 7.11 (b) show the nuclear density in the $^1\pi\pi^*$ state at 20 fs and in the $^1\pi\sigma^*$ state at 30 fs, respectively, for the (1,2) initial preparation. As expected, there are two nodal lines in the $^1\pi\pi^*$ state along the coupling coor-

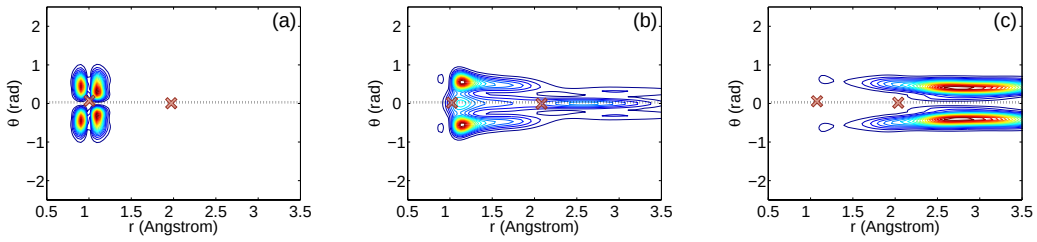

Figure 7.10: Snapshots of the probability density in the diabatic $^1\pi\pi^*$ state at 20 fs (a), the diabatic $^1\pi\sigma^*$ state at 30 fs (b) and the diabatic ground state at 30 fs (c), for the (1,1) initial condition. The crosses indicate the locations of the two conical intersections.

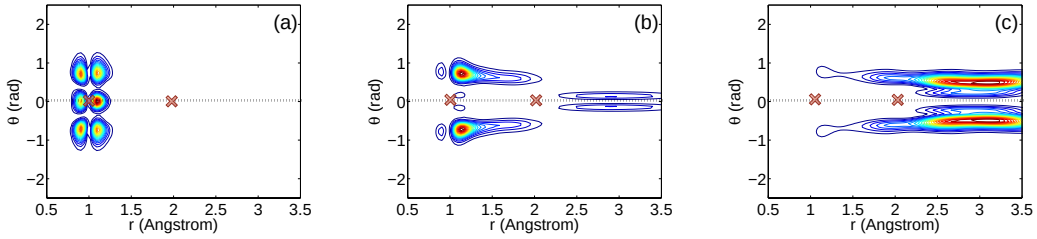

Figure 7.11: Snapshots of the probability density in the diabatic $^1\pi\pi^*$ state at 20 fs (a), the diabatic $^1\pi\sigma^*$ state at 30 fs (b) and the diabatic ground state at 30 fs (c), for the (1,2) initial condition. The crosses indicate the locations of the two conical intersections.

dinate. As before, the nodal line in the stretching coordinate disappears after the transition through the $^1\pi\pi^*$-$^1\pi\sigma^*$ conical intersection, while an additional nodal line is created at $\theta = 0$ in the WP in the $^1\pi\sigma^*$ state.

In the discussion of the population decay of the $^1\pi\pi^*$ state, we have pointed out that an "odd-even" effect exists for $n_r = 1$ when successive quanta are put into the coupling mode. This effect can be understood from the inspection of the WPs in Figs. 7.9 - 7.11. As a function of θ, the central part of the WP (close to $\theta = 0$) tends to move along the diabatic path at the conical intersection, while the wing parts prefer to follow the adiabatic path. For the (1,1) initial condition, the initial wavefunction in the $^1\pi\pi^*$ state has a nodal line at $\theta = 0$. Therefore, the WP will preferentially go around the conical intersection, following the adiabatic

pathway, which implies a switch to the $^1\pi\sigma^*$ diabatic state. This explains why the decay of the diabatic $^1\pi\pi^*$ population is faster in this case than for the other two initial conditions.

The projected nuclear densities obtained for the (2,0), (2,1) and (2,2) initial conditions are qualitatively similar and are therefore not shown. With increasing excitation of the coupling mode, the distribution of density along θ becomes more delocalized. This leads to preferentially adiabatic motion of the WP at the conical intersection, implying the faster decay of the population of the diabatic $^1\pi\pi^*$ state.

7.2.4.2 The $^1\pi\sigma^*$-S_0 conical intersection

After the population transfer from the $^1\pi\pi^*$ state to the $^1\pi\sigma^*$ state, the WP quickly reaches the $^1\pi\sigma^*$-S_0 conical intersection due to the strongly repulsive character of the $^1\pi\sigma^*$ PE function. Fig. 7.9 (b), Fig. 7.10 (b) and Fig. 7.11 (b) show the probability density projected on the $^1\pi\sigma^*$ state at 30 fs, for the (1,0), (1,1) and (1,2) initial conditions respectively. Parts of the WP have already passed the second conical intersection. It is seen that the $^1\pi\sigma^*$ probability density abruptly drops in the region of the $^1\pi\sigma^*$-S_0 conical intersection, especially in the outer wings.

For the (1,0) initial condition, the nuclear density in the diabatic S_0 state, after having passed through both conical intersections, is shown in Fig. 7.9 (c) at $t = 30$ fs. Although the diabatic WP is an even function of θ and there is thus no nodal line at $\theta = 0$, the density is clearly bifurcated, reflecting the splitting of the WP by the steep lower cone of the adiabatic surface near the $^1\pi\sigma^*$-S_0 conical intersection (see Fig. 7.3 (c)).

For the (1,1) initial condition, the WP projected on the diabatic S_0 state is shown in Fig. 7.10 (c). It is an antisymmetric function of θ and it has an exact nodal line at $\theta = 0$. It can again be seen that the density is forced away from $\theta = 0$ by the steep lower cone of the $^1\pi\sigma^*$-S_0 conical intersection.

For the (1,2) initial condition, the WP in the diabatic S_0 state (Fig. 7.11 (c)) is again an even function of θ. It is seen that increasing excitation of the coupling

mode spreads the WP in the θ direction. This reduces the probability density in the immediate vicinity of the conical intersections.

As discussed previously, the excitation of the coupling mode broadens the probability density along θ, resulting in a more adiabatic pathway. In addition, the presence of a nodal line at $\theta = 0$ also favors transfer between diabatic states. These two mechanisms govern the population transfer at the second conical intersection and thus affect the dissociation probabilities. Among the (1,0), (1,1) and (1,2) initial conditions, only the (1,1) case results in a WP in the $^1\pi\sigma^*$ state without a nodal line at $\theta = 0$. This WP hits the second conical intersection with a significant probability at $\theta = 0$, amplifying the flux along the diabatic path (that is towards the lower adiabatic dissociation limit).

For (2,0), (2,1) and (2,2) initial conditions, the odd-even effect is not visible because of the higher initial energies. As previously found in the photoinduced dynamics of pyrrole [89, 93], excitation of the coupling mode spreads the nuclear density along θ, thus enhancing the dissociation probability towards the upper adiabatic limit.

We do not observe reflection and subsequent capture of the WP in the bound part of the ground-state surface for any initial condition. This reflects the fact that both dissociation channels are open and that the excess energy cannot be absorbed by other degrees of freedom in our two dimensional model.

7.3 Summary

We have investigated the quantum WP dynamics following the excitation of the $S_1(^1\pi\pi^*)$ state of phenol. A two-dimensional model has been constructed, which includes the OH stretching motion and the internal rotation of the OH group. The repulsive PE function of the dark $^1\pi\sigma^*$ excited state of phenol crosses the PE functions of the $^1\pi\pi^*$ and S_0 states, resulting in two conical intersections.

We have computed the adiabatic PE surfaces, DMs and TDMs with the CASSCF method. A diabatic two-mode three-state Hamiltonian has been constructed via an analytic ansatz for the three-state diabatic PE matrix and a least-squares fit of the eigenvalues to the *ab initio* data. The resulting diabatic

PE surfaces, as well as DMs and TDMs, are smooth functions of the nuclear coordinates.

The ultrafast photoinduced dynamics of phenol has been investigated using the time-dependent quantum WP propagation method. We have calculated the lifetime of the $^1\pi\pi^*$ state, as well as the branching ratio between the two dissociation channels, for various initial vibrational levels. The results show that (i) the photodissociation rate is dramatically enhanced when one quantum of the OH stretching mode is excited, and (ii) the excitation of the coupling mode has a noticeable impact on the lifetime of the $^1\pi\pi^*$ state and the branching ratio of the two dissociation channels. For the (1,n_θ) initial conditions, we observe an odd-even effect with respect to the number n_θ of quanta in the coupling mode. For the (2,n_θ) initial conditions, increasing excitation of the coupling mode results in a shortening of the lifetime of the $^1\pi\pi^*$ state and an increase of the flux in the upper adiabatic dissociation channel.

We also have developed an intuitive picture of the photodissociation dynamics through two conical intersections. The interplay of two conical intersections can have a profound influence on the WP dynamics. In the case of phenol, the symmetry of the nuclear wavefunction plays a key role for the understanding of the dynamics at the conical intersections. When the WP switches between diabatic surfaces, its symmetry with respect to the coupling mode changes. The resulting node structure of the nuclear WP is "felt" by the second conical intersection, with pronounced implications for the branching ratio of dissociation. The second conical intersection acts as a sensitive "detector" for the nonadiabatic dynamics occurring at the first conical intersection.

Chapter 8

Quantum dissipative dynamics of pyrrole

In this chapter, the influence of vibrational relaxation on the photoinduced dynamics of pyrrole via the $^1A_2$–S_0 conical intersection is investigated within the reduced density matrix formalism. The system involves the $^1A_2$–S_0 conical intersection and takes the dominant tuning (NH stretching) and the dominant coupling coordinate into account. We consider the coupling of the system to an environment which represents the other photo-inactive modes. This environment is modelled by a thermal bath composed of many independent harmonic oscillators. The system-bath coupling is defined to properly describe the vibrational energy transfer from the system to the bath. The reduced density matrix is propagated to explore the influence of the dissipation of the system energy on the internal-conversion dynamics of pyrrole.

8.1 Theoretical framework

8.1.1 Model Hamiltonian

The total Hamiltonian is

$$\hat{H} = \hat{H}_s + \hat{H}_b + \hat{H}_{sb}, \tag{8.1}$$

where $\hat{H}_s$, $\hat{H}_b$ and $\hat{H}_{sb}$ denote the system Hamiltonian, the bath Hamiltonian and the system-bath coupling Hamiltonian, respectively.

The system Hamiltonian in the present model is expressed in the diabatic basis:

$$\hat{H}_s = \hat{T}_N \begin{pmatrix} 1 & 0 \\ 0 & 1 \end{pmatrix} + \begin{pmatrix} V_{11} & V_{12} \\ V_{21} & V_{22} \end{pmatrix}, \tag{8.2}$$

where V_{11} and V_{22} describe the PE surfaces of the diabatic electronic states, correlating with the ground diabatic S_0 and $^1A_2$ states, respectively. The off-diagonal elements describe the electronic couplings between the two diabatic states. Here, the OH stretching coordinate is the tuning coordinate and the normal coordinate Q_{11} is the dominant coupling coordinate. The kinetic-energy operator $\hat{T}_N$ is given by:

$$\hat{T}_N = -\frac{\hbar^2}{2\mu}\frac{\partial^2}{\partial r^2} - \frac{1}{2}\omega_{11}\frac{\partial^2}{\partial Q_{11}^2}. \tag{8.3}$$

The details of this 2D model are discussed in Chapter 6.

The other photo-inactive vibrational modes are described by a bath composed of many independent harmonic oscillators:

$$\hat{H}_b = \sum_b \frac{\omega_b}{2}(\hat{P}_b^2 + \hat{Q}_b^2), \tag{8.4}$$

with the dimensionless coordinates Q_b and momenta P_b.

From the WP calculations in Chapter 6, we have already seen that a minor part of the nuclear WP enters the bound region of the S_0 surface. This part of the WP shows that the NH stretching motion is highly excited. Thus, we expect that the cooling of the OH vibration should enhance the internal-conversion probability. Therefore, in a first approximation, it is sufficient to consider only the vibrational relaxation of the tuning coordinate. Thus the system-bath interaction Hamiltonian is written as:

$$\hat{H}_{sb}^t = \{|\phi_1^d\rangle\langle\phi_1^d| + |\phi_2^d\rangle\langle\phi_2^d|\}\hat{K}\sum_b g_{t,b}\hat{Q}_{t,b}, \tag{8.5}$$

$$\hat{K} = \exp[-a_1(r - r_0)] \tag{8.6}$$

where we take the value of a_1 from the potential function of the S_0 state of pyrrole (see Chapter 6). The exponential decay of the system-bath coupling with r reflects the fact that the intramolecular vibrational relaxation involving the departing H-atom takes place in the bound region and vanishes in the dissociation limit (see Chapter 5).

The bath is characterized by a spectral density. Here we take the Ohmic form:

$$J(\omega) = \eta\omega\Theta(\omega)e^{-\frac{\omega}{\omega_c}}, \tag{8.7}$$

where η is a parameter describing the system-bath coupling strength and $\Theta(\omega)$ is the Heaviside step function. We assume that the cutoff frequency ω_c equals the fundamental vibrational frequency of the OH stretching mode. We assume zero temperature.

8.1.2 Quantum master equation

If we assume that the coupling between the bath and the system is weak, the motion of the reduced density operator follows the Redfield equation (see Chapter 5):

$$\frac{\partial}{\partial t}\hat{\rho}_s(t) = -i\hat{L}_s\hat{\rho}_s(t) + \hat{D}\hat{\rho}_s(t), \tag{8.8}$$

$$\hat{L}_s\bullet = -i[\hat{H}_s, \bullet], \tag{8.9}$$

$$\hat{D}\hat{\rho}_s(t) = -\int_0^\infty d\tau \quad (C(\tau)[\hat{K}, \hat{K}^{(I)}(-\tau)\hat{\rho}_s(t)] - C(-\tau)[\hat{K}, \hat{\rho}_s(t)\hat{K}^{(I)}(-\tau)]) . \tag{8.10}$$

In the present calculations, a coordinate-grid and a harmonic-oscillator basis are used to represent the tuning and coupling coordinates, respectively. This representation is called "MGBR", which has been discussed in Chapters 4 and 6.

8.1.3 Preparation of initial state

The initial state is prepared via the vertical excitation of selected vibrational states of the electronic ground state to the excited-state surface (see Chapter 5).

8.1.4 Propagation of reduced density matrix

In the present calculations, the split-operator technique is applied to disentangle the short-time propagations governed by $\hat{L}_s$ and $\hat{D}$. For the short-time propagation governed by the system Hamiltonian, we use the split-operator technique again. The FFT method is used to evaluated the kinetic-energy operator of the NH stretching coordinate. For the dissipative part in the quantum master equation, we use the Runge-Kutta method to propagate the density matrix for a finite time step. In the evaluation of the Redfield tensors, the Lamb shifts are neglected.

To construct the real parts of the Redfield tensors, the operators $\hat{K}$ and $\hat{K}^{(I)}(-\tau)$ are represented in the MGBR (see Chapter 5). Eq. 5.81 exhibits the procedure to perform this task for $\hat{K}$, while the evaluation of $\hat{K}^{(I)}(-\tau)$ follows the method proposed in the last subsection of Chapter 5. Since the dissipation takes place in the bound region and vanishes in the dissociation limit, we can define a box to describe this localized dissipation. The pseudo-eigenstates of this box are used to evaluate the matrix representation of $\hat{K}^{(I)}(-\tau)$ according to Eq. 5.82. The inner edge of the box is $r_{min} = 3.0$ au, which is the inner edge of the grid for the density-matrix propagation. The outer edge of the box is increased until convergence is achieved. This yields $r_{max} = 7.5$ au. The pseudo-eigenstates are obtained by the diagonalization of the Hamiltonian inside this box with the DVR technique. We use 60 Colbert-Miller DVR functions for r and 10 harmonic-oscillator basis functions for Q_c to construct the matrix representation of the Hamiltonian in this this box.

For the propagation of the reduced density matrix, we use 128 grid points for r, from 3.0 au to 15.8 au. For the coupling mode, we employ 10 harmonic-oscillator basis functions. The reduced density matrix is propagated for 160 fs with a time step 0.2 fs. The total propagation time is long enough to ensure that convergence is reached. To avoid reflection at the grid boundary, we activate the damping function for $r_{mask} > 12.5$ au.

8.1.5 Physical observables and probability density

The electronic population probabilities and dissociation probabilities have been gain an understanding of the essential features of the dissipative dynamics of pyrrole. We determine the dissociation probability by measuring the quantum flux passing through a surface at r_D=12 au in the dissociation limit.

To describe the internal-conversion dynamics, we define the population probability of the bound region [r_{min}, r_I] in the diabatic electronic ground state:

$$P_0^I(t) = \int_{r_{min}}^{r_I} dr \sum_m ...\rho^d_{0,0,m,m}(t,r,r). \tag{8.11}$$

We choose r_I=5.0 au to get a reasonable characterization of the bound region.

To obtain insight into dissipative dynamics, we have also calculated the nuclear probability density in the ith diabatic state (see Chapter 5), which is

$$\begin{aligned} \varrho_i^d(t,r,Q_c) &= \rho^d_{i,i}(t,r,r,Q_c,Q_c) & (8.12)\\ &= \sum_{m,n} \langle Q_c|\,\nu_m\rangle\, \rho^d_{i,i,m,n}(t,r,r)\, \langle \nu_n|\,Q_c\rangle\,. & (8.13) \end{aligned}$$

8.2 Results and discussion

In this section, we discuss the dependence of the internal-conversion dynamics of pyrrole on the system-bath coupling strength. Previous WP calculations have already exhibited the influence of the excitation of the NH stretching mode on the reaction rate. The ultrafast dynamics does not take place when the NH stretching motion is not excited. If one quantum of energy is put into the NH stretching mode, we observe an ultrafast decay of the excited-state population via the $^1A_2$–S_0 conical intersection. Only in this case, a minor part of the nuclear WP enters the bound region of the S_0 surface. For excitations beyond n_r=1, the WP passes the conical intersection once and dissociates directly. Thus, we select n_r=1 as the appropriate initial conditions for the investigation of the internal-conversion dynamics of pyrrole.

We have already calculated the quantum dissipative dynamics of pyrrole for the (1,0), (1,1) and (1,2) initial conditions. The results show that the general

features of the dynamics and their dependence on the system-bath coupling are similar in these different initial conditions. Therefore, for sake of brevity, we only discuss the quantum dissipative dynamics for the (1,0) initial condition.

8.2.1 Electronic population dynamics

To test the density-matrix propagation code, we have repeated the calculation of nonadiabatic dynamics through the A_2–S_0 conical intersection. Fig. 8.1 shows the time-dependent electronic-population probabilities.

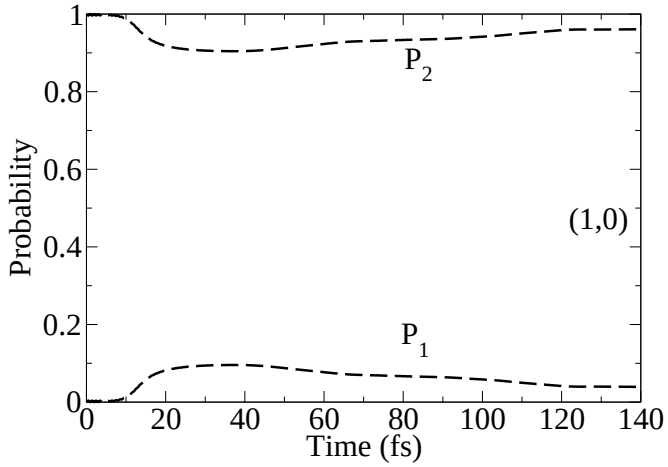

Figure 8.1: Population probabilities of the diabatic states for the initial (1,0) condition; P_1 the ground S_0 state, and P_2: the $^1A_2$ state.

The comparison of the results of the density-matrix calculation and the WP calculation (see Chapter 6) proves that the density matrix propagation reproduces the time evolution of the diabatic population correctly. We observe the fast population decay of P_2 in the first stage of the reaction and the slow recovery in the later stages. The mechanism behind this population dynamics has been discussed in Chapter 6.

For the directly dissociating part of the WP, the system-bath coupling cannot slow down the WP motion due to the ultrafast timescale. For the minor part of the WP entering the bound region, on the other hand, the coupling to the

environment can induce vibrational energy dissipation, thus leading to internal conversion. Because only a minor part of the WP can enter the bound region before dissociation, the effect of the vibrational damping on the overall population dynamics is rather small. Thus, we do not discuss the electronic population probabilities for $\eta \neq 0$.

8.2.2 Internal-conversion dynamics

Fig 8.2 shows the time-dependent probability in the bound region of the diabatic S_0 state, P^I, for different system-bath coupling strengths (from η=0 to η=1.2).

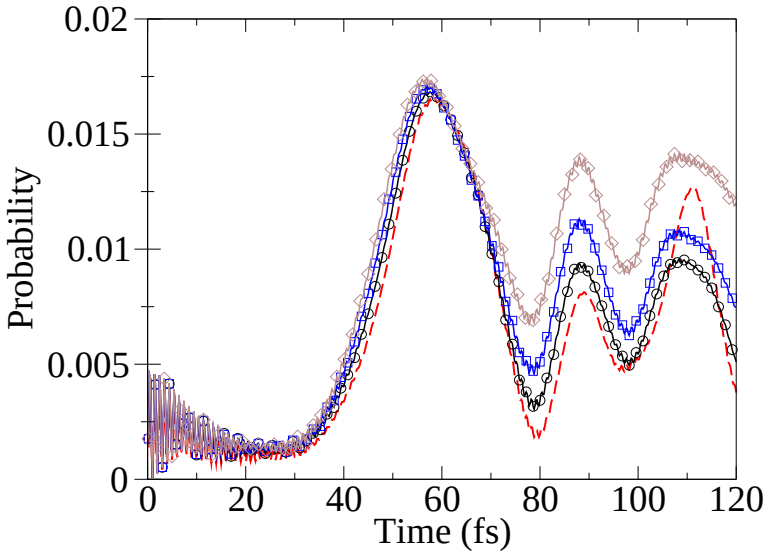

Figure 8.2: Internal-conversion probabilities obtained for different damping strengths for the initial (1,0) condition: $\eta = 0$ (dashed line), $\eta = 0.4$ (solid line with circles), $\eta = 0.8$ (solid line with squares) and $\eta = 1.2$ (solid line with diamonds).

For the isolated system (η=0), P^I remains nearly zero within 20 fs. P^I begins to increase at 40 fs and decrease at 60 fs. After a few recurrences, P^I eventually decays to zero. This behaviour of the time-dependent internal-conversion probability can be understood by the reaction mechanism. In the early stage of

the reaction, the WP is in the $^1A_2$ state before reaching the conical intersection. After the population transfer, the part of the WP with large excess kinetic energy continues to move towards large NH distances. Only the low-energy part of the WP, which is reflected by the attractive potential of the S_0 state, enters the bound region. Therefore, P^I begins to rise at 40 fs, at later time than the main nonadiabatic population transfer (30 fs). Because of the high excess energy in the OH stretching motion, the WP quickly oscillates in the bound region. In the absence of vibrational energy relaxation, P^I decays to zero.

Although the probability in the bound region of the S_0 state is rather small, we can observe the enhancement of P^I by the system-bath coupling. With increasing coupling strength η (from $\eta = 0$ to $\eta = 1.2$), we observe that the oscillations of P^I become less pronounced and that P^I does not decay to zero (see Fig. 8.2). This reflects the fact that the damping of the NH stretching motion by the heat bath captures a part of the WP in the bound region. In other words, the coupling of the system with the remaining vibrational modes enhances the internal-conversion probability.

The damping effect is not pronounced here and the internal-conversion probability remains rather small for the present initial condition. However, a more significant dissipation effect is expected when the NH stretching mode is not excited. The WP, which escapes from the well of the $^1\pi\sigma^*$ state by quantum tunnelling, moves slowly. The damping caused by the system-bath coupling them acts on a longer timescale. After the population transfer at the $^1A_2$–S_0 conical intersection, the WP moving on the S_0 state should be completely reflected back to the bound region, because its energy is lower than that of the upper dissociation limit. Therefore, a large amount of the WP should enter the bound region. This implies that the influence of system-bath coupling on the internal-conversion dynamics should become more pronounced.

8.2.3 The nuclear probability densities

To get more insight of the influence of the dissipation effects on the system dynamics, we provide a detailed picture of the time-dependent nuclear probability

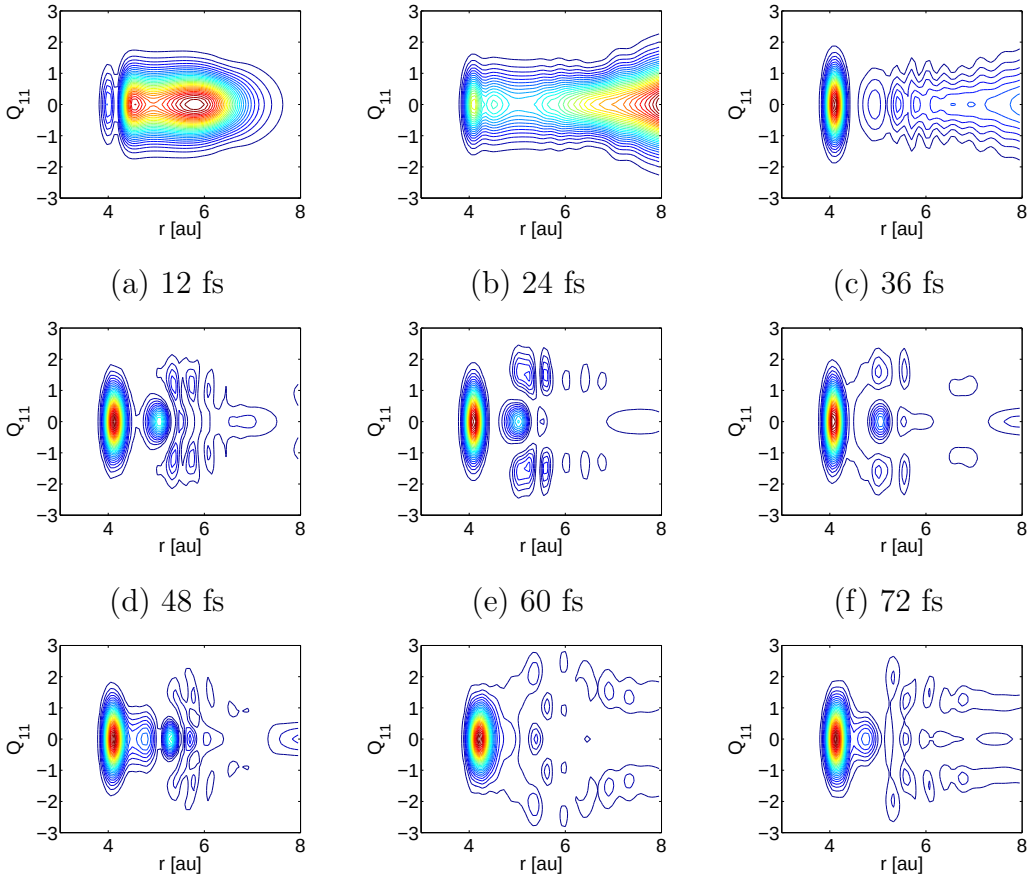

(a) 12 fs (b) 24 fs (c) 36 fs

(d) 48 fs (e) 60 fs (f) 72 fs

(g) 84 fs (h) 96 fs (i) 108 fs

Figure 8.3: Snapshots of the nuclear probability density in the diabatic $^1A_2$ state as function of r and Q_{11} at different times, for $\eta = 0$. The snapshots are taken every 12 fs.

densities as functions of r and Q_{11}, for the (1,0) initial condition. The time step for the presentation of the snapshot is 12 fs.

Figs. 8.3 and 8.4 show the probability densities of the diabatic $^1A_2$ and S_0 states, respectively, for the isolated system, $\eta = 0$. These figures do not provide new information but recall the results of the WP calculations in Chapter 6.

After the initial WP has been prepared by the vertical excitation, it moves on the PE surface of the diabatic $^1A_2$ state to the conical intersection within 12 fs, see Fig. 8.3 (a). The central part follows the diabatic pathway and a large part of the WP quickly moves towards the lower dissociation limit within 36 fs, see Fig. 8.3 (b) and (c). Afterwards, a little probability density remains in the

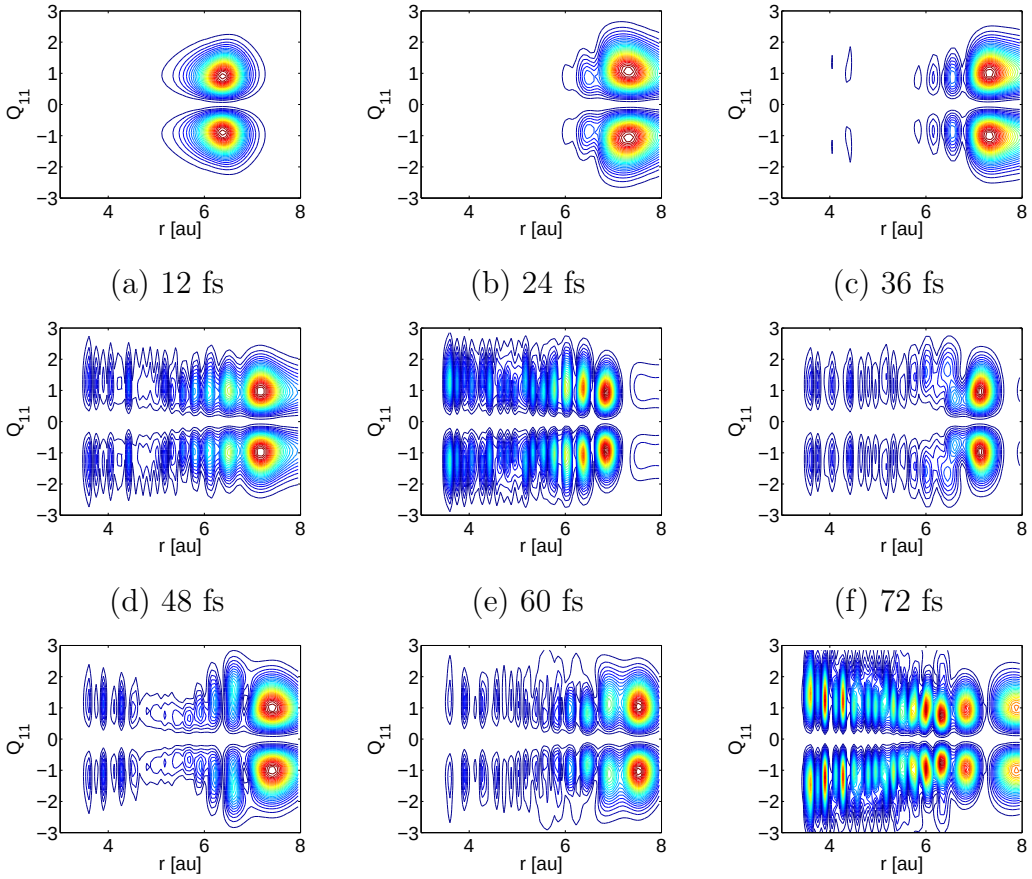

(a) 12 fs (b) 24 fs (c) 36 fs

(d) 48 fs (e) 60 fs (f) 72 fs

(g) 84 fs (h) 96 fs (i) 108 fs

Figure 8.4: Snapshots of the nuclear probability density in the diabatic S_0 state as function of r and Q_{11} at different times, for $\eta = 0$. The snapshots are taken every 12 fs.

FC and conical intersection regions, corresponding to the residual WP trapped by the well on the $^1A_2$ surface and the upper cone of the conical intersection, respectively. Note that the WP in the upper cone of the conical intersection exhibits a multi-node pattern.

At the conical intersection, the wing part of the WP will follow the adiabatic path towards the upper dissociation limit. A nodal line at Q_{11}=0 is created by the conical intersection, since the coupling operator is an odd function of Q_{11}, see Fig. 8.4. The high-energy part of the WP moves towards the upper dissociation limit directly, see Figs. 8.4 (b) and (c), while a tiny part with low energy is reflected and enters the bound region, see Figs. 8.4 (d)-(i). This part of the WP

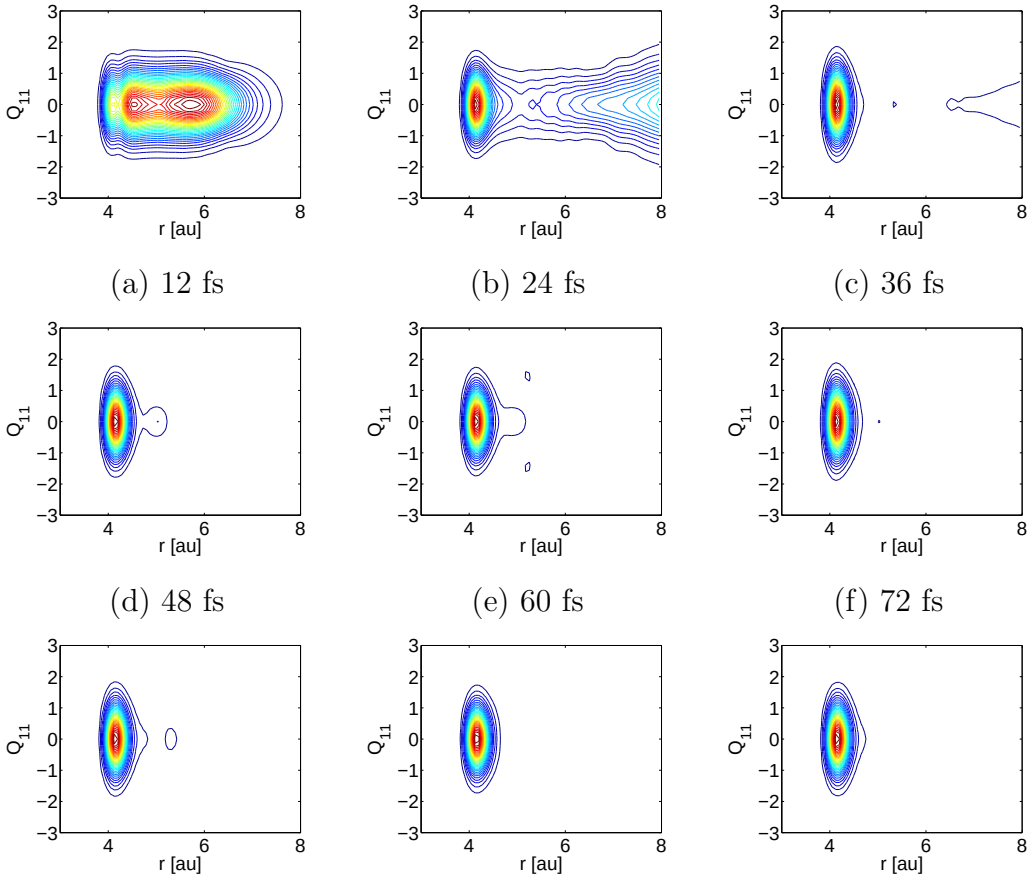

(a) 12 fs (b) 24 fs (c) 36 fs

(d) 48 fs (e) 60 fs (f) 72 fs

(g) 84 fs (h) 96 fs (i) 108 fs

Figure 8.5: Snapshots of the nuclear probability density in the diabatic $^1A_2$ state as function of r and Q_{11} at different times, for $\eta = 1.2$. The snapshots are taken every 12 fs

displays a multi-node structure, indicating the high vibrational excitation of the NH stretching mode.

Next, the time-dependent nuclear density probabilities are discussed when the system-bath coupling is taken into account. For sake of brevity, I show here the nuclear probability densities of $^1A_2$ and S_0 states in Figs. 8.5 and 8.6, respectively, for the case $\eta = 1.2$.

In the early stage of the reaction, the WP motion in the $^1A_2$ state is similar to the $\eta = 0$ case (see Figs. 8.3 (a)-(c) and 8.5 (a)-(c)). As a result of the repulsive PE surface of the $^1A_2$ state, the WP accesses the conical intersection quickly. The

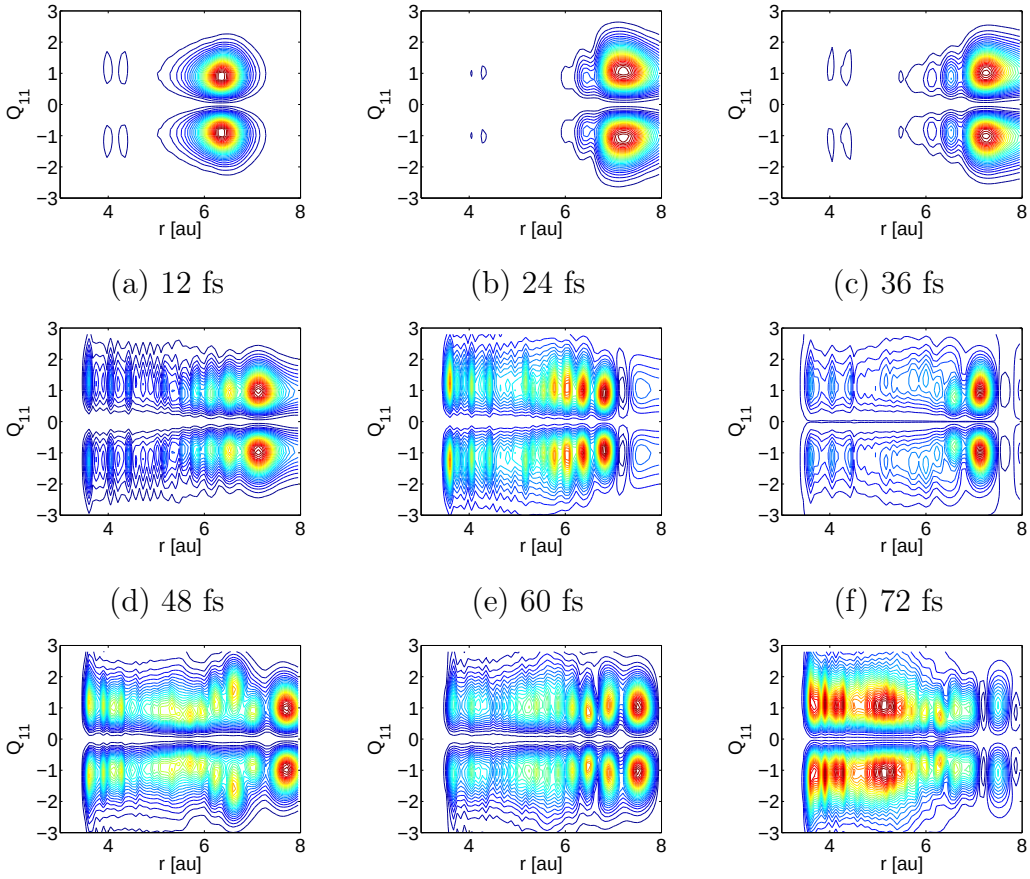

(a) 12 fs (b) 24 fs (c) 36 fs

(d) 48 fs (e) 60 fs (f) 72 fs

(g) 84 fs (h) 96 fs (i) 108 fs

Figure 8.6: Snapshots of the nuclear probability density in the diabatic S_0 state as function of r and Q_{11} at different times, for $\eta = 1.2$. The snapshots are taken every 12 fs

center part following the diabatic path moves towards the lower dissociation limit. Since this process takes place within 40 fs, the dissipation does not play a role here. After later time, however, the vibrational relaxation completely removes the probability density in the conical intersection region, see Figs. 8.5 (e)-(i). Only the WP trapped by the well of the $^1A_2$ state is left.

In the S_0 state, the nodal line at Q_{11}=0 is kept, because the system-bath interaction Hamiltonian of this model preserves the symmetry of the system. In the early stage of the reaction (up to 36 fs), only minor differences in the system dynamics exist between the $\eta = 0$ and $\eta = 1.2$ cases, see Figs. 8.6 (a)-(c).

Afterwards, the damping of the NH vibrational motion induced by the environment becomes obvious, see Figs. 8.6 (d)-(i). The multi-node structure of the NH vibrational WP is suppressed to a certain degree. This reflects the fact that the excess energy of the NH stretching motion is transferred to the environment. The vibrational cooling leads to the survival of more nuclear probability density in the bound region of the S_0 state. In other words, it enhances the internal-conversion probability.

8.3 Summary

We have explored the quantum dissipative dynamics of pyrrole through the $^1A_2$–S_0 conical intersection. The dissipation is introduced *via* the weak coupling of the NH stretching coordinate to a bath composed of many harmonic oscillators. The quantum master equation has been solved to explore the internal-conversion dynamics of pyrrole.

The physical observables, such as the electronic population probabilities and the internal-conversion probability, have been calculated to understand the quantum dissipative dynamics of pyrrole. The primary finding is that energy dissipation of the system leads to a non-zero probability for internal conversion. As expected, the probability of internal conversion is enhanced by increasing the system-bath coupling strength.

A rather detailed picture of the quantum dissipative dynamics of pyrrole has been developed in terms of time-dependent nuclear probability densities as functions of the tuning and coupling coordinates. The system-bath coupling induces a damping of the NH stretching motion and suppresses the fragmentation of the hot molecule.

While the internal-conversion probability is rather small for pyrrole, the computational method developed here can be used to explore the photoinduced dynamics of larger biomolecules. In the DNA pairs, for example, the hydrogen bond connects the two aromatic ring groups, therefore the dissociation channel is closed. After population transfer at the conical intersection, a large part of the WP can enter the bound region of the ground states without fragmentation. In this case,

the environment has sufficient time to induce vibrational relaxation of the system and to lead to internal conversion. Even with a rather small system-bath coupling strength, the internal conversion takes place on the picosecond timescale, see Ref [64]. Thus, an appropriate extension of the present calculations will be useful to explain the mechanism of the photostability of biomolecular systems.

Chapter 9

Conclusions and outlook

We have chosen pyrrole and phenol as representative systems to explore the photoinduced nonadiabatic dynamics of aromatic biomolecules. Models of reduced dimensionality have been developed which include the tuning coordinate (NH or OH stretching mode) and a few dominant coupling modes. The diabatic PE surfaces have been constructed on the basis of accurate *ab initio* multi-reference electronic-structure data. Time-dependent quantum WP methods have been used to explore the nonadiabatic dynamics at conical intersections. The influence of vibrational relaxation on the internal-conversion dynamics of pyrrole has been investigated in the framework of the reduced density-matrix formalism.

For pyrrole, we have systematically characterized the two lowest conical intersections [$^1A_2$–S_0 and $^1B_1$–S_0], exploying the CASSCF method. The coupling strengths of all symmetry-allowed coupling modes of these two conical intersections have been obtained. To understand the main features of the dynamics through the conical intersections, we have constructed 2D models including the NH stretching coordinate and the dominant coupling mode for each conical intersection. To explore the influence of multiple coupling modes on the dynamics, we have also developed multi-mode models by including additional weak coupling modes. The ultrafast nonadiabatic dynamics of pyrrole has been investigated using time-dependent quantum WP propagation methods.

For phenol, we have taken three states and two conical intersections [$^1\pi\pi^*$–$\pi\sigma^*$ and $\pi\sigma^*$–S_0] into account. Since these two conical intersections possess the

same coupling mode, it was sufficient to develop a 2D model. We have performed time-dependent quantum WP calculations to explore the ultrafast nonadiabatic dynamics of phenol.

In the quantum WP calculations of pyrrole and phenol, we have investigated the dependence of the nonadiabatic dynamics on the initial preparation of the system. The following conclusions can be draw from these calculations: (1) The photodissociation rate is dramatically enhanced when one quantum of the NH or OH stretching mode is excited. (2) the excitation of the strong coupling mode has a noticeable impact on the population transfer and the branching ratio of the two dissociation channels. In general, the excitation of the coupling mode will enhance the adiabatic pathway. (3) The inclusion of the weak coupling modes has a rather weak impact on the population dynamics, while they lead to the interesting effects in the nuclear probability densities.

These findings indicate that control of the photodissociation dynamics *via* mode-specific IR excitation, as recently demonstrated for ammonia [269–272], should be possible for these molecules. For phenol, theoretical studies have suggested that the branching ratio of photodissociation can be controlled by optimization of the excitating laser pulse [121].

Many aromatic biomolecules share similar photoinduced dynamical processes. After photoexcitation, the nuclear WP is transferred from the bright $^1\pi\pi^*$ excited state to a dark $^1\pi\sigma^*$ state through a conical intersection. Experimentally, it is difficult to obtain information about the nonadiabatic transition at the first conical intersection. The experiments provide information about the dynamics at the second conical intersection, *e.g. via* the branching ratio of the different dissociation channels. For the example of phenol, we have shown that the geometric phase induced by the first conical intersection has a pronounced effect on the dynamics at the second conical intersection. Therefore, the experimental results on the branching ratio contain information on the nonadiabatic dynamics occurring at the first conical intersection.

When the WP passes the second conical intersection, a part of it can be reflected and temporarily captured in the bound region of the ground state. In

few-mode systems, the excess energy can not be absorbed. In multi-mode systems, the excess energy in the tuning mode can be absorbed by other degrees of freedom, which results in the capture of the WP in the bound region of the electronic ground state. This interplay of conical intersections and vibrational energy relaxation explains the mechanism of the radiationless decay dynamics of aromatic biomolecules.

When pyrrole is excited with wavelengths shorter than 220 nm, the dynamics start from the optically bright $^1B_2(\pi\pi^*)$ and $^1A_1(\pi\pi^*)$ states. Therefore, a more comprehensive description of the photodissociation process involves five electronic states [S_0, $^1A_2(\pi\sigma^*)$, $^1B_1(\pi\sigma^*)$, $^1B_2(\pi\pi^*)$, and $^1A_1(\pi\pi^*)$] and several types of conical intersections, $\pi\pi^*$–$\pi\sigma^*$ [86], $\pi\sigma^*$–S_0 [89, 93], as well as $\pi\pi^*$–S_0 [267]. In addition, the $^2A_2$ and $^2B_1$ electronic states of the pyrrolyl radical are strongly coupled through a conical intersection [$^1A_2(\pi\sigma^*)$–$^1B_1(\pi\sigma^*)$] [265, 266]. Although each of these conical intersections has been characterized individually, a comprehensive picture of the dynamics of the photodissociation process has not been developed yet. Therefore, it is a great challenge to set up a more complete multi-state multi-mode model and to perform bechmark calculations for the photoinduced dynamics of pyrrole.

The experimental observations have shown that the photodissociation dynamics of phenol involves a remarkably limited number of the vibrational modes [95, 120]. Therefore, a systematic investigation should be performed to identify all relevant tuning and coupling modes. A reduced model including the strongly coupled modes should be constructed and the WP dynamics calculations should be performed for such extended model. Moreover, the effects of the coupling between the active modes and the inactive modes on the photoinduced dynamics of phenol should be explored in the future.

Previous calculations have shown that several aromatic biomolecules exhibit rather similar PE profiles, for instance indole. Therefore, the quantum dynamics of indole can be explored with the methods developed in the present thesis.

Many biologically relevant molecular systems contain hydrogen bonds (*e.g.*, the DNA pairs). Until now, the theoretical investigations of these systems have

exhibited the characteristic features of the excited-state PE surfaces, as well as their conical intersections with the ground state. These calculations have identified possible reaction channels of the photoinduced dynamics, but a treatment of the nonadiabatic nuclear dynamics is still missing. Thus, the quantum dynamics of these systems should be explored to understand their photophysical and photochemical properties, in particular their roles for the photostability of life.

Appendix A

Dimensionless normal coordinates

The small-amplitude vibrational motion of a polyatomic molecule with N atoms can be described by a group of uncoupled harmonic oscillators [209]. In this so-called normal-mode approximation, the molecular vibrational Hamiltonian is expressed as:

$$\hat{H} = \sum_{i=1}^{M} -\frac{1}{2}\frac{\partial^2}{\partial q_i^2} + \frac{1}{2}\omega_i^2 q_i^2. \tag{A.1}$$

The total number M of the normal modes is $3N-6$ (for nonlinear molecules) or $3N-5$ (for linear molecules). For each normal mode, q_i and ω_i are the coordinate and the frequency, respectively. In this approximation, the total vibrational wavefunction becomes the direct product of the wavefunctions for each normal mode.

Defining frequency-weighted dimensionless coordinates

$$Q_i = \sqrt{\omega_i} q_i, \tag{A.2}$$

the Hamiltonian becomes

$$\hat{H} = \sum_{i=1}^{M} \omega_i(-\frac{1}{2}\frac{\partial^2}{\partial Q_i^2} + \frac{1}{2}Q_i^2). \tag{A.3}$$

The Schrödinger equation for the ith mode is:

$$\omega_i(-\frac{1}{2}\frac{\partial^2}{\partial Q_i^2} + \frac{1}{2}Q_i^2)\psi_n(Q_i) \;\; = \;\; (n+\frac{1}{2})\omega_i\psi_n(Q_i). \tag{A.4}$$

In the calculation of the PE surfaces near conical intersections, we have to make displacements along different normal modes. However, the displacement vectors obtained from a standard package, like GAUSSIAN [31], are only valid in the vicinity of equilibrium configuration become the normal modes are expanded in Cartesian displacement coordinates. To perform finite displacements along normal modes, we express the normal-mode displacements as linear combinations of internal-coordinate displacements, like bond distances and bond angles.

The procedure for the construction of finite normal mode-like displacements has been described in detail in Ref. [276]. After calculating the Hessian at the reference geometry with a the standard package, we have obtained the transformation matrix $\mathbf{B}$ between the dimensionaless normal-mode coordinates $\{Q_i\}$ and Cartesian coordinates $\{x_i\}$

$$\mathbf{Q} = \mathbf{B}\mathbf{x}. \tag{A.5}$$

It is also possible to express the internal symmetry coordinates $\{s_i\}$ as a linear combination of the Cartesian coordinates $\{x_i\}$ via a matrix $\mathbf{C}$:

$$\mathbf{s} = \mathbf{C}\mathbf{x}. \tag{A.6}$$

Furthermore, a linear relation between internal symmetry coordinates $\{s_i\}$ and dimensionless normal coordinates $\mathbf{Q}$ is established via a matrix $\mathbf{L} = \mathbf{B}\mathbf{C}^{-\mathbf{1}}$:

$$\mathbf{Q} = \mathbf{L}\mathbf{s} = \mathbf{B}\mathbf{C}^{-\mathbf{1}}\mathbf{s}. \tag{A.7}$$

In other words, for finite displacements from the reference configuration, the coordinates $\{Q_i\}$ can be considered to be linear combinations of the symmetry coordinates $\{s_i\}$. Subsequently, a Cartesian geometry corresponding to a given displacement Q_i is constructed by explicitly considering the changes of internal bond length and bond angle variables in the transformation through an iterative scheme.

Appendix B

Bath correlation function

The importance of the reservoir correlation function for the dynamics of the system is apparent from the quantum master equation. In this appendix, we discuss general properties of this function.

Since $\hat{F}_m$ is a Hermitian operator, we obtain the property (see Eq. 5.33):

$$C^*_{mn}(t) = C_{nm}(-t). \tag{B.1}$$

Considering the Fourier transformation of this function:

$$C_{mn}(\omega) = \int_{-\infty}^{\infty} dt e^{i\omega t} C_{mn}(t), \tag{B.2}$$

we obtain the relation:

$$C_{nm}(-\omega) = \int_{-\infty}^{\infty} dt e^{i\omega t} C^*_{mn}(t). \tag{B.3}$$

In frequency space, the detail balance principle requires:

$$\frac{C_{mn}(\omega)}{C_{nm}(-\omega)} = \exp(\frac{\hbar\omega}{k_B T}) \tag{B.4}$$

where k_B is the Bolzmann constant and T is the temperature of the bath.

The transformation of the correlation function from the frequency domain to the time domain can be recast in terms of a half-side Fourier integral over positive ω:

$$\begin{aligned} C_{mn}(t) &= \int_{-\infty}^{\infty} d\omega \frac{1}{2\pi} e^{-i\omega t} C_{mn}(\omega), \\ &= \int_{0}^{\infty} d\omega \frac{1}{2\pi} \left[e^{-i\omega t} C_{mn}(\omega) + e^{i\omega t} e^{-\frac{\hbar\omega}{k_B T}} C_{nm}(\omega) \right] \end{aligned} \tag{B.5}$$

For the harmonic-oscillator bath, the spectral density $J(\omega)$ is a function in the frequency domain. Therefore we can use it to express $C(\omega)$. Then the half-side Fourier transformation of $C(\omega)$ generates $C(\tau)$, the bath correlation function in the time domain. This provides an alternative way to obtain Eq. 5.43 in Chapter 5.

Appendix C

List of abbreviations

AIMS	*Ab initio* multiple spawning
AT	Adenine-thymine
BO	Born-Oppenheimer
CASPT2	Complete-active-space perturbation theory 2
CASSCF	Complete-active-space self-consistent-field
CI	Configuration interaction
CID	Double excitation of configuration interaction
CIS	Single excitation of configuration interaction
CISD	Single and double excitations of configuration interaction
DM	Dipole moment
DVR	Discrete variational representation
FBR	finite basis representation
FC	Frank-Condon
FFT	Fast-Fourier-transformation
FOCI	First-order configuration interaction.
GC	Guanine-cytosine
HF	Hartree-Fock
IR	Infrared radiation
JT	Jahn-Teller
LCAO	linear combination of atomic orbitals

MCSCF	Milti-configuration self-consistent-field
MCTDH	Multi-configuration time-dependent Hartree
MGBR	Mix-grid-eigenstate representation
MO	Molecular orbital
MP	Møller-Plesset perturbation
MRCI	Multi-reference configuration interaction
PE	Potential energy
RT	Renner-Teller
SCF	Self-consistent-field
SOCI	Second-order configuration interactions
TDM	Transition dipole moment
UV	Ultraviolet
VBR	Variational basis representation
WP	Wave packet
2D	Two dimensional
3D	Three dimensional

Bibliography

[1] M. Wayne and B. Wayne, *Photochemistry*, Oxford University Press, New York, 1996.

[2] M. B. Robin, *Higher Excited State of Polyatomic Molecules*, Academic Press, New York, 1972.

[3] R. Schinke, *Photodissociation Dynamics*, Cambridge University Press, Cambridge, 1993.

[4] W. Domcke, D. R. Yarkony, and H. Köppel, *Conical Intersections: Electronic Structure, Dynamics and Spectroscopy*, World Scientific, Singapore, 2004.

[5] M. Born and J. R. Oppenheimer, Annu. Phys. (Leipzig) **84**, 457 (1927).

[6] J. Manz and L. Wöste, *Femtosecond Chemistry*, VCH, New York, 1994.

[7] A. H. Zewail, *Femtochemistry–Ultrafast Dynamics of the Chemical Bond*, World Scientific, Singapore, 1994.

[8] F. Hund, Z. Physik **40**, 742 (1927).

[9] I. von Neumann and E. Wigner, Physik Z **30**, 467 (1929).

[10] E. Teller, J. Phys. Chem. **41**, 109 (1937).

[11] H. Jahn and E. Teller, Proc. Roy. Soc. **161**, 220 (1937).

[12] E. Renner, Z. Physik **92**, 172 (1934).

[13] W. Kauzmann, *Quantum Chemistry*, Academic Press, New York, 1957.

[14] G. Herzberg and H. C. Longuet-Higgins, Disc. Faraday Soc. **35**, 77 (1963).

[15] H. E. Zimmerman, J. Am. Chem. Soc. **88**, 1566 (1966).

[16] W. T. A. M. van der Lugt and L. J. Oosterhoff, J. Am. Chem. Soc. **91**, 6042 (1969).

[17] T. Forster, Pure Appl. Chem. **24**, 443 (1970).

[18] R. C. Dougherty, J. Am. Chem. Soc. **93**, 7187 (1971).

[19] J. Michl, J. Am. Chem. Soc. **95**, 7948 (1973).

[20] J. Michl, Top. Curr. Chem. **46**, 1 (1974).

[21] L. Salem, J. Am Chem. Soc. **96**, 3486 (1974).

[22] H. C. Longuet-Higgins, Proc. R. Soc. London A **344**, 147 (1975).

[23] V. Bonačić-Koutecký, J. Koutecký, and J. Michl, Angew. Chem. Int. Ed. Engl **26**, 170 (1987).

[24] D. Yarkony, Rev. Mod. Phys. **68**, 985 (1996).

[25] D. Yarkony, Acc. Chem. Res. **31**, 511 (1998).

[26] D. Yarkony, J. Phys. Chem. A **105**, 6277 (2001).

[27] G. J. Atchity, S. S. Xantheas, and K. Ruedenberg, J. Chem. Phys. **95**, 1862 (1991).

[28] I. N. Ragazos, M. A. Robb, F. Bernardi, and M. Olivucci, Chem. Phys. Lett. **197**, 217 (1992).

[29] M. J. Berapark, M. A. Robb, and H. B. Schlegel, Chem. Phys. Lett. **223**, 269 (1994).

[30] F. Bernardi, M. A. Robb, and M. Olivucci, Chem. Soc. Reviews. **25**, 321 (1996).

[31] M. J. Frisch et al., `GAUSSIAN 98`, Gaussian, Inc., Pittsburgh PA, 2000.

[32] H. Lischka et al., COLUMBUS, an ab initio electronic structure program, release 5.9.1 (2006).

[33] M. Klessinger and J. Michl, *Excited States and Photochemistry of Organic Molecules*, VCH Publishers, New York, 1995.

[34] E. E. Nikitin, *Chemische Elementarprozesse, Ed. H. Hartmann*, Springer, Berlin, 1968.

[35] R. Englman and J. Jortner, J. Chem. Phys. **18**, 145 (1970).

[36] M. Desouter-Locomte, D. Dehareng, B. Leyh-Nihant, A. J. Praet, M. T. Lorquet, and J. C. Lorquet, J. Chem. Phys. **89**, 214 (1985).

[37] A. Kuppermann, *in Dynamics of Molecules and Chemical Reactions,*, Ed. R. E. Wyatt and J. Z. Zhang, Marcel Dekker, New York, 1996.

[38] B. Leptit and A. Kuppermann, Chem. Phys. Lett. **166**, 581 (1990).

[39] Y. S. M. Wu, A. Kuppermann, and B. Leptit, Chem. Phys. Lett. **186**, 319 (1991).

[40] A. Kuppermann and R. Abrol, Adv. Chem. Phys. **124**, 323 (2002).

[41] H. Köppel, W. Domcke, and L. S. Cederbaum, Adv. Chem. Phys. **57**, 59 (1984).

[42] W. Domcke and G. Stock, Adv. Chem. Phys. **100**, 1 (1997).

[43] H.-D. Meyer, U. Manthe, and L. S. Cederbaum, Chem. Phys. Lett. **165**, 73 (1990).

[44] U. Manthe, H.-D. Meyer, and L. S. Cederbaum, J. Chem. Phys. **97**, 3199 (1992).

[45] M. H. Beck, A. Jäckle, G. A. Worth, and H.-D. Meyer, Phys. Rep. **324**, 1 (2000).

[46] A. Raab, G. Worth, H.-D. Meyer, and L. S. Cederbaum, J. Chem. Phys. **110**, 1999 (1999).

[47] G. Worth, H.-D. Meyer, and L. S. Cederbaum, Chem. Phys. Lett. **229**, 451 (1999).

[48] G. A. Worth and M. A. Robb, Adv. Chem. Phys. **124**, 355 (2002).

[49] A. G. Worth and L. S. Cederbaum, Ann. Rev. Phys. Chem. **55**, 127 (2004).

[50] H. Wang and M. Thoss, J. Chem. Phys. **119**, 1289 (2003).

[51] H. Wang and M. Thoss, J. Chem. Phys. **124**, 034114 (2006).

[52] M. Thoss, W. H. Miller, and G. Stock, J. Chem. Phys. **112**, 10282 (2000).

[53] J. C. Tully, J. Chem. Phys. **93**, 1061 (1990).

[54] M. Barbatti, M. Ruckenbauer, and H. Lischka, J. Chem. Phys. **122**, 174307 (2005).

[55] M. Barbatti, G. Granucci, M. Persico, and H. Lischka, Chem. Phys. Lett. **401**, 276 (2005).

[56] M. Barbatti, G. Granucci, H. Lischka, M. Ruckenbauer, and M. Persico, Newton-X: a package for Newtonian dynamics close to the crossing seam (2006).

[57] R. Mitrić, V. Bonačić-Koutecký, J. Pittner, and H. Lischka, J. Chem. Phys. **125**, 024303 (2006).

[58] V. Bonačić-Koutecký and R. Mitrić, Chem. Rev. **105**, 11 (2005).

[59] A. Toniolo, S. Olsen, L. Manohar, and T. J. Martinez, Faraday Discuss. **127**, 149 (2004).

[60] J. D. Coe and T. J. Martinez, J. Am. Chem. Soc. **127**, 4560 (2005).

[61] J. D. Coe and T. J. Mattinez, J. Phys. Chem. **110**, 618 (2006).

[62] L. Seidner and W. Domcke, Chem. Phys. **186**, 27 (1994).

[63] A. Kühl and W. Domcke, Chem. Phys. **259**, 227 (2000).

[64] A. Kühl and W. Domcke, J. Chem. Phys. **116**, 263 (2002).

[65] S. Krempl, M. Winterstetter, L. Plöhn, and W. Domcke, J. Chem. Phys. **100**, 926 (1994).

[66] S. Krempl, M. Winterstetter, and W. Domcke, J. Chem. Phys. **102**, 6499 (1995).

[67] S. Krempl, W. Domcke, and M. Winterstetter, Chem. Phys. **206**, 63 (1996).

[68] B. Wolfseder and W. Domcke, Chem. Phys. **235**, 370 (1995).

[69] B. Wolfseder and W. Domcke, Chem. Phys. **259**, 113 (1996).

[70] P. R. Callis, Annu. Rev. Phys. Chem. **34**, 329 (1983).

[71] D. Creed, Photochem. Photobiol. **39**, 537 (1984).

[72] C. E. Crespo-Hernandez, B. Cohen, P. M. Hare, and B. Kohler, Chem. Rev. **104**, 1997 (2004).

[73] A. L. Sobolewski and W. Domcke, Europhysicsnews **37**, 20 (2006).

[74] P. A. Mullen and M. K. Orloff, J. Chem. Phys. **51**, 2276 (1969).

[75] W. M. Flicker, O. A. Mosher, and A. Kuppermann, J. Chem. Phys. **64**, 1315 (1976).

[76] C. D. Cooper, A. D. Williamson, J. C. Miller, and R. N. Compton, J. Chem. Phys. **73**, 1527 (1980).

[77] D. A. Blank, S. W. North, and Y. T. Lee, Chem. Phys. **187**, 35 (1994).

[78] H. Nakatsuji, O. Kitao, and T. Yonezawa, J. Chem. Phys. **83**, 723 (1985).

[79] H. Nakano, T. Tsuneda, T. Hashimoto, and K. Hirao, J. Chem. Phys. **104**, 2312 (1996).

[80] M. H. Palmer, I. C. Walker, and M. F. Guest, Chem. Phys. **238**, 179 (1998).

[81] O. Christiansen, J. Gauss, J. F. Stanton, and P. Jørgensen, J. Chem. Phys. **111**, 525 (1999).

[82] B. O. Roos, P.-A. Malmqvist, V. Molina, L. Serrano-Andrés, and M. Merchán, J. Chem. Phys. **116**, 7526 (2002).

[83] A. L. Sobolewski, W. Domcke, C. Dedonder-Lardeux, and C. Jouvet, Phys. Chem. Chem. Phys. **4**, 1093 (2002).

[84] P. Celani and H.-J. Werner, J. Chem. Phys. **119**, 5044 (2003).

[85] K. R. F. Somers, E. S. Kryachko, and A. Ceulemans, J. Phys. Chem. A. **107**, 5427 (2003).

[86] H. Köppel, E. V. Gromov, and A. B. Trofimov, Chem. Phys. **304**, 35 (2004).

[87] J. Wei, A. Kuczmann, J. Riedel, F. Renth, and F. Temps, Phys. Chem. Chem. Phys. **5**, 315 (2004).

[88] J. Wei, J. Riedel, A. Kuczmann, F. Renth, and F. Temps, Faraday. Discuss. **127**, 267 (2004).

[89] V. Vallet, Z. Lan, S. Mahapatra, A. L. Sobolewski, and W. Domcke, Faraday Discuss. **127**, 283 (2004).

[90] H. Lippert, H. H. Ritze, I. V. Hertel, and W. Radloff, ChemPhysChem **5**, 1423 (2004).

[91] B. Cronin, M. G. D. Nix, R. H. Qadiri, and M. N. R. Ashfold, Phys. Chem. Chem. Phys. **6**, 5031 (2004).

[92] R. Burcl, S. Carter, and N. C. Handy, Phys. Chem. Chem. Phys. **6**, 340 (2004).

[93] V. Vallet, Z. Lan, S. Mahapatra, A. L. Sobolewski, and W. Domcke, J. Chem. Phys **123**, 144307 (2005).

[94] B. Cronin, A. L. Devine, M. G. D. Nix, and M. N. R. Ashfold, Phys. Chem. Chem. Phys. **8**, 3440 (2006).

[95] M. N. R. Ashfold, B. Cronin, A. L. Devine, and M. G. D. Nix, Science **312**, 1637 (2006).

[96] R. J. Lipert, G. Bermudez, and S. D. Colson, J. Phys. Chem. **92**, 3801 (1988).

[97] J. A. Syage, Z. Phys. D. **30**, 1 (1994).

[98] N. Mikami, Bull. Chem. Soc. Jpn. **68**, 683 (1995).

[99] T. S. Zwier, Annu. Rev. Phys. Chem. **47**, 205 (1996).

[100] R. M. Helm, H. P. Vogel, and H. J. Neusser, J. Phys. Chem. **11**, 4496 (1998).

[101] G. Pino et al., Phys. Chem. Chem. Phys. **2**, 893 (2000).

[102] S. Ishiuchi et al., J. Chem. Phys. **117**, 7083 (2002).

[103] O. David, D. Dedonder-Lardeux, and C. Jouvet, Int. Rev. Phys. Chem. **21**, 449 (2002).

[104] C. M. Tseng, Y. T. Lee, and C. K. Ni, J. Chem. Phys. **121**, 2459 (2004).

[105] Y. Yamada, T. Ebata, M. Kayano, and N. Mikami, J. Chem. Phys. **120**, 7400 (2004).

[106] M. Kayano, T. Ebata, Y. Yamada, and N. Mikami, J. Chem. Phys. **120**, 7410 (2004).

[107] J. Lorentzon, P. A. Malmqvist, M. Fülscher, and B. O. Roos, Theor. Chim. Acta. **91**, 91 (1995).

[108] T. Etaba, N. Mizuochi, T. Watanabe, and N. Mikami, J. Phys. Chem. A **100**, 546 (1996).

[109] G. Gregoire, D. Dedonder-Lardeux, C. Jouvet, S. Matrenchard, and D. Solgadi, J. Phys. Chem. A **105**, 5971 (2001).

[110] H. Watanabe and S. Iwata, J. Chem. Phys. **105**, 420 (1996).

[111] S. Schumm, M. Gerhards, W. Roth, H. Gier, and K. Kleinermanns, Chem. Phys. Lett. **263**, 126 (1996).

[112] S. Re and Y. Osamura, J. Phys. Chem. **102**, 3798 (1998).

[113] W. H. Fang, J. Chem. Phys. **112**, 1204 (2000).

[114] W. H. Fang and R. Z. Liu, J. Chem. Phys. **113**, 5253 (2000).

[115] G. Granucci, J. T. Hynes, P. Millié, and T. H. Tran-Thi, J. Am. Chem. Soc. **122**, 12243 (2000).

[116] A. L. Sobolewski and W. Domcke, J. Phys. Chem. **105**, 9275 (2001).

[117] K. Daigoku, S. Ishiuchi, M. Sakai, M. Fujii, and K. Hashimoto, J. Chem. Phys. **119**, 5149 (2003).

[118] W. Domcke and A. L. Sobolewski, Science **302**, 1693 (2003).

[119] Z. Lan, W. Domcke, V. Vallet, A. L. Sobolewski, and S. Mahapatra, J. Chem. Phys **122**, 224315 (2005).

[120] M. G. D. Nix, A. L. Devine, B. Cronin, R. N. Dixon, and M. N. R. Ashfold, J. Chem. Phys. **125**, 133318 (2006).

[121] M. Abe, Y. Ohtsuki, Y. Fujimura, Z. Lan, and W. Domcke, J. Chem. Phys **124**, 224316 (20056).

[122] A. L. Sobolewski and W. Domcke, Chem. Phys. Lett. **293**, 2315 (1999).

[123] H. Lippert et al., J. Phys. Chem. A **107**, 8239 (2004).

[124] C. Dedonder-Lardeux, C. Jouvet, S. Perun, and A. L. Sobolewski, Phys. Chem. Chem. Phys. **5**, 5118 (2003).

[125] H. Lippert, V. Stert, C. P. Schulz, I. V. Hertel, and W. Radloff, Phys. Chem. Chem. Phys. **6**, 2718 (2004).

[126] H. Lippert, H.-H. Ritze, I. V. Hertel, and W. Radloff, Chem. Phys. Lett. **398**, 526 (2004).

[127] H.-H. Ritze, H. Lippert, V. Stert, W. Radloff, and I. V. Hertel, J. Chem. Phys. **120**, 3619 (2004).

[128] M. F. Lin, C. M. Tseng, Y. T. Lee, and C. K. Ni, J. Chem. Phys **123**, 124303 (2005).

[129] A. Sur and P. M. Johnson, J. Chem. Phys. **84**, 1206 (1986).

[130] R. J. Lipert and S. D. Colson, J. Phys. Chem. **93**, 135 (1989).

[131] C. P. Schick, S. D. Carpenter, and P. M. Weber, J. Phys. Chem. A **103**, 10470 (1999).

[132] B. Cronin, M. G. D. Nix, A. L. Devine, and M. N. R. Dixon, R. N. snd Ashfold, Phys. Chem. Chem. Phys. **8**, 599 (2006).

[133] H. J. Jensen, H. Koch, P. Jørgensen, and J. Olsen, Chem. Phys. **119**, 297 (1988).

[134] J. M. O. Matos and B. O. Roos, J. Am. Chem. Soc. **110**, 7664 (1988).

[135] M. P. Fülscher, L. Serrano-Andrés, and B. O. Roos, J. Am. Chem. Soc. **119**, 6168 (1997).

[136] A. Broo and A. Holmen, J. Phys. Chem. **101**, 3589 (1997).

[137] A. Broo, J. Phys. Chem. **102**, 526 (1998).

[138] N. J. Kim et al., J. Phys. Chem. A **104**, 6552 (2000).

[139] B. Menucci, A. Toniolo, and J. Tomasi, J. Phys. Chem. A **105**, 4749 (2001).

[140] B. Menucci, A. Toniolo, and J. Tomasi, J. Phys. Chem. A **105**, 7126 (2001).

[141] E. L. Rachofsky, J. B. A. Roos, M. Krauss, and O. Osman, J. Phys. Chem. A **105**, 190 (2001).

[142] S. Matsika, J. Phys. Chem. A **108**, 7854 (2004).

[143] S. Perun, A. L. Sobolewski, and W. Domcke, Chem. Phys. **313**, 107 (2005).

[144] S. Perun, A. L. Sobolewski, and W. Domcke, J. Am. Chem. Soc. **127**, 6257 (2005).

[145] M. Z. Zgierski, S. Patchkovskii, and E. C. Lim, J. Chem. Phys **123**, 081101 (2005).

[146] C. M. Marian, J. Chem. Phys. **122**, 104314 (2005).

[147] H. Chen and S. Li, J. Phys. Chem. **109**, 8443 (2005).

[148] H. Chen and S. Li, J. Chem. Phys. **124**, 154315 (2006).

[149] H. Chen and S. Li, J. Phys. Chem. **110**, 12360 (2006).

[150] D. Roca-Sanjuán, M. Rubio, M. Mechán, and L. Serrano-Andrés, J. Phys. Chem. **125**, 084302 (2006).

[151] W. C. Chung et al., Phys. Chem. Chem. Phys. (to be published).

[152] N. J. Kim et al., J. Chem. Phys. **113**, 10051 (2000).

[153] D. C. Lührs, J. Viallon, and I. Fischer, Phys. Chem. Chem. Phys. **3**, 1827 (2001).

[154] H. Kang, K. T. Lee, B. Jund, Y. J. Ko, and S. K. Kim, J. Am. Chem. Soc. **124**, 12958 (2002).

[155] H. Kang, K. T. Lee, and S. K. Kim, Chem. Phys. Lett. **359**, 213 (2002).

[156] H. Kang, B. Jung, and S. K. Kim, J. Chem. Phys. **118**, 6717 (2003).

[157] I. Hünig et al., ChemPhysChem. **5**, 147 (2004).

[158] S. Ullrich, T. Schultz, M. Z. Zgierski, and A. Stolow, J. Am. Chem. Soc. **126**, 2262 (2004).

[159] M. Zierhut, W. Roth, and I. Fischer, Phys. Chem. Chem. Phys. **6**, 5178 (2004).

[160] N. J. Kim, H. Kang, Y. D. Park, and S. K. Kim, Phys. Chem. Chem. Phys. **6**, 2802 (2004).

[161] T. Pancur, N. K. Schwalb, F. Renth, and F. Temps, Chem. Phys. **313**, 199 (2005).

[162] C. Canuel et al., J. Chem. Phys. **122**, 074316 (2005).

[163] H.-H. Ritze et al., J. Chem. Phys. **122**, 224302 (2005).

[164] A. L. Sobolewski and W. Domcke, Phys. Chem. Chem. Phys. **6**, 2723 (2004).

[165] V. Guallar, A. Douhal, M. Moreno, and J. M. Lluch, J. Phys. Chem. A **103**, 6251 (1999).

[166] M. K. Shukla and J. Leszcynski, J. Phys. Chem. A **106**, 4709 (2002).

[167] A. L. Sobolewski, W. Domcke, and C. Huttig, Proc. Nat. Acad. Sci. **102**, 17903 (2005).

[168] S. Perun, A. L. Sobolewski, and W. Domcke, J. Phys. Chem. A (Submitted).

[169] M. Born and K. Huang, *Dynamical Theory of Crystal Lattices*, Oxford Univ. Press, New York, 1985.

[170] M. Baer, Adv. Chem. Phys. **124**, 39 (2002).

[171] M. Bixon and J. Jortner, J. Chem. Phys. **48**, 715 (1968).

[172] M. Bixon and J. Jortner, J. Chem. Phys. **50**, 4061 (1969).

[173] M. Baer, Mol. Phys. **40**, 1011 (1980).

[174] C. A. Mead and D. G. Truhlar, J. Chem. Phys. **77**, 6090 (1982).

[175] A. Vibók, G. J. Halász, and M. Baer, Chem. Phys. Lett. **399**, 7 (2004).

[176] T. Vértesi, A. Vibók, G. J. Halász, and M. Baer, J. Chem. Phys. **120**, 2565 (2004).

[177] T. Vértesi, A. Vibók, G. J. Halász, and M. Baer, J. Chem. Phys. **120**, 8420 (2006).

[178] T. Vértesi, A. Vibók, G. J. Halász, and M. Baer, J. Chem. Phys. **121**, 4000 (2006).

[179] H.-J. Werner and W. Meyer, J. Chem. Phys. **75**, 5802 (1980).

[180] R. J. Cave and N. D. Newton, J. Chem. Phys. **106**, 9213 (1997).

[181] C. Petrongolo, G. Hirsch, and R. J. Buenker, Mol. Phys. **70**, 825 (1990).

[182] M. Peric, R. J. Buenker, and Peyerimhoff, Mol. Phys. **70**, 673 (1990).

[183] G. Hirsch, R. J. Buenker, and C. Petrongolo, Mol. Phys. **70**, 835 (1990).

[184] D. Yarkony, J. Phys. Chem. **102**, 8073 (1998).

[185] T. Pacher, L. S. Cederbaum, and H. Köppel, J. Chem. Phys. **12**, 7367 (1988).

[186] L. S. Cederbaum, J. Schirmer, and H.-D. Meyer, J. Phys. A **22**, 2427 (1989).

[187] K. Ruedenberg and G. J. Atchity, J. Chem. Phys. **99**, 3799 (1993).

[188] W. Domcke and C. Woywod, Chem. Phys. Lett. **216**, 362 (1993).

[189] W. Domcke, C. Woywod, and M. Stengle, Chem. Phys. Lett. **226**, 257 (1994).

[190] C. Woywod, M. Stengle, W. Domcke, H. Flöthmann, and R. Schinke, J. Chem. Phys. **107**, 7282 (1997).

[191] D. Simah, B. Hartke, and H.-J. Werner, J. Chem. Phys. **111**, 4523 (1999).

[192] H. Nakamura and D. G. Truhlar, J. Chem. Phys. **115**, 10353 (2001).

[193] MOLPRO is a package of ab initio programs written by H.-J. Werner and P. J. Knowles, with contributions from R. D. Amos, A. Berning, D. L. Cooper, M. J. O. Deegan, A. J. Dobbyn, F. Eckert, C. Hampel, G. Hetzer, T. Leininger, R. Lindh, A. W. Lloyd, W. Meyer, M. E. Mura, A. Nicklaß, P. Palmieri, K. Peterson, R. Pitzer, P. Pulay, G. Rauhut, M. Schütz, H. Stoll, A. J. Stone and T. Thorsteinsson.

[194] C. Woywod, W. Domcke, A. L. Sobolewski, and H. J. Werner, J. Chem. Phys. **100**, 1400 (1994).

[195] H. Köppel, J. Gronki, and S. Mahapatra, J. Chem. Phys. **115**, 2337 (2002).

[196] F. Bernardi, S. De, M. Olivucci, and M. A. Robb, J. Am Chem. Soc. **112**, 1737 (1990).

[197] B. Simon, Phys. Rev. Lett. **51**, 2167 (1983).

[198] M. V. Berry, Proc. R. Soc. London A **392**, 45 (1984).

[199] A. Shapere and F. Wilczek, *Geometric Phases in Physics*, World Scientific, Singapore, 1989.

[200] J. W. Zwanziger, M. Koenig, and A. Pines, Ann. Rev. Phys. Chem. **41**, 601 (1990).

[201] C. A. Mead, Rev. Mod. Phys. **64**, 51 (1992).

[202] L. S. Cederbaum, E. Gindensperger, and I. Burghardt, Phys. Rev. Lett. **94**, 113003 (2005).

[203] E. Gindensperger, I. Burghardt, and L. S. Cederbaum, J. Chem. Phys. **124**, 144103 (2006).

[204] E. Gindensperger, I. Burghardt, and L. S. Cederbaum, J. Chem. Phys. **124**, 144104 (2006).

[205] A. Szabo and N. S. Ostlund, *Modern Quantum Chemistry*, McGraw-Hill, New York, 1989.

[206] A. R. Leach, *Molecule Modeling, 2nd Ed.*, Pearson Education, Hong Kong, 2001.

[207] M. W. Schmidt and M. S. Gordon, Annu. Rev. Phys. Chem. **49**, 233 (1998).

[208] B. O. Roos, *in Ab initio Methods in Quantum Chemistry, Part 2*, Ed. K.P. Lawley, John Wiley & Sons Ltd, Chichester, 1987.

[209] E. B. Wilson, J. C. Decius, and P. C. Cross, *Molecular vibrations*, McGraw-Hill, New York, 1995.

[210] B. Podolsky, Phys. Rev. **32**, 812 (1928).

[211] J. Tennyson and B. T. Sutcliffe, J. Chem.. Phys. **77**, 4061 (1982).

[212] B. T. Sutcliffe, Mol. Phys. **48**, 561 (1983).

[213] N. C. Handy, Mol. Phys. **61**, 207 (1987).

[214] S. Carter, Mol. Phys. **48**, 745 (1984).

[215] H. Meyer, Annu. Rev. Phys. Chem. **53**, 141 (2002).

[216] J. E. Hadder and H. Frederick, J. Chem. Phys. **97**, 3500 (1992).

[217] D. Feit, J. A. Fleck, and A. Steiger, J. Comput. Phys. **47**, 412 (1982).

[218] D. Kosloff and R. A. Kosloff, J. Comput. Phys. **52**, 35 (1983).

[219] H. Tal-Ezer and R. Kosloff, J. Chem. Phys. **81**, 3967 (1984).

[220] T. J. Park and J. Light, J. Chem. Phys. **85**, 5870 (1986).

[221] R. Kosloff, J. Phys. Chem. **92**, 2087 (1988).

[222] C. Leforestier et al., J. Comput. Phys. **94**, 59 (1991).

[223] R. Kosloff, Annu. Rev. Phys. Chem. **45**, 145 (1994).

[224] G. C. Schatz, J. Chem. Phys. **100**, 12839 (1996).

[225] D. O. Harris, G. G. Engerholm, and W. D. Gwinn, J. Chem. Phys. **43**, 1515 (1965).

[226] A. S. Dickinson and P. R. Certain, J. Chem. Phys. **49**, 4209 (1968).

[227] J. Light, I. P. Hamilton, and J. V. Lill, J. Chem. Phys. **82**, 1400 (1985).

[228] Z. Bačić and J. Light, Annu. Rev. Phys. Chem. **40**, 469 (1989).

[229] U. Manthe and H. Köppel, J. Chem. Phys. **93**, 345 (1990).

[230] J. C. Light and T. Carrington Jr., Adv. Chem. Phys. **114**, 263 (2000).

[231] D. T. Colbert and W. H. Miller, J. Chem. Phys. **96**, 1 (1992).

[232] R. T. Skodje, R. Sadeghi, H. Köppel, and J. L. Krause, J. Chem. Phys. **101**, 1725 (1994).

[233] U. Manthe, H. D. Meyer, and L. S. Cederbaum, J. Chem. Phys. **97**, 9062 (1992).

[234] R. Kosloff and D. Kosloff, J. Comput. Phys. **63**, 363 (1986).

[235] D. Neuhasuer and M. Baer, J. Chem. Phys. **90**, 4351 (1989).

[236] S. Mahapatra and N. Sathyamurthy, J. Chem. Soc., Faraday Trans. **97**, 9062 (1997).

[237] G. C. Schatz and M. A. Ratner, *Quantum Mechanics in Chemistry*, Dover Publications,, New York, 2002.

[238] W. H. Louisell, *Quantum Statistical Propetties of Radition*, Wiley, New York, 1973.

[239] V. May and O. Kühn, *Charge and Energy Transfer Dnamics in Molecular systems*, Willey-VCH, Berlin, 2000.

[240] U. Weiss, *Quantum dissipative systems*, World Scientific, Singapore, 1993.

[241] K. Blum, *Density Matrix Theory and Applications*, Plenum Press, New York, 1996.

[242] J. Shao, J. Chem. Phys. **120**, 5053 (2004).

[243] G. Lindblad, Math. Phys. **48**, 119 (1976).

[244] R. Kosloff, M. A. Ratner, and W. B. Davis, J. Chem. Phys. **106**, 7036 (1997).

[245] D. A. Lidar, Z. Bihary, and K. B. Whaley, Chem. Phys. **268**, 35 (2001).

[246] D. M. Lockwood, M. Ratner, and R. Kosloff, Chem. Phys. **268**, 55 (2001).

[247] S. Nakajima, Progr. Theor. Phys. **20**, 948 (1958).

[248] R. Zwanzig, J. Chem. Phys. **33**, 1338 (1960).

[249] F. Bloch, Phys. Rev. **70**, 460 (1946).

[250] W. T. Pollard and R. A. Friesner, J. Chem. Phys. **100**, 5054 (1994).

[251] W. T. Pollard, A. K. Felts, and R. A. Friesner, Adv. Chem. Phys. **XCIII**, 77 (1996).

[252] D. Egorova, *Phd. Thesis*, TUM, Munich, 2002.

[253] Y. Tanimura and P. Wolynes, Phys. Rev. A **43**, 4131 (1991).

[254] Y. Tanimura and P. Wolynes, J. Chem. Phys. **96**, 8485 (1992).

[255] B. B. Laird, J. Budimir, and J. L. Skinner, J. Chem. Phys. **94**, 4391 (1992).

[256] A. Suárez, R. Silbey, and I. Oppenheim, J. Chem. Phys. **94**, 5101 (1992).

[257] C. Meier and D. J. Tannor, J. Chem. Phys. **111**, 3365 (1999).

[258] H. P. Breuer, B. Kappler, and F. Petruccione, Phys. Rev. A **59**, 1633 (1999).

[259] H. P. Breuer, B. Kappler, and F. Petruccione, Annu. Phys. **291**, 36 (2001).

[260] D. Egogrova, M. Thoss, W. Domcke, and W. Haobin, J. Chem. Phys. **119**, 2761 (2003).

[261] Y. Yan and R. Xu, Annu. Rev. Phys. Chem. **56**, 187 (2005).

[262] B. Hellsing and H. Metiu, Chem. Phys. Lett. **127**, 45 (1986).

[263] M. Berman, R. Kosloff, and H. Tal-Ezer, J. Phys. A **25**, 1283 (1992).

[264] U. Banin, A. Barrana, S. Ruhman, and R. Kosloff, J. Chem. Phys. **101**, 8461 (1994).

[265] A. J. Gianola et al., J. Phys. Chem. **108**, 10326 (2004).

[266] A. Motzke, Z. Lan, C. Woywod, and W. Domcke, Chem. Phys. **329**, 50 (2006).

[267] M. Barbatti, M. Vazdar, A. J. A. Aquino, M. Eckert-Maksić, and H. Lischka, J. Chem. Phys. **125**, 164323 (2006).

[268] T. H. Dunning, J. Chem. Phys. **90**, 1007 (1989).

[269] A. Bach, J. M. Hutchison, R. J. Holiday, and F. F. Crim, J. Phys. Chem. A **116**, 4955 (2002).

[270] A. Bach, J. M. Hutchison, R. J. Holiday, and F. F. Crim, J. Phys. Chem. A **116**, 9315 (2002).

[271] A. Bach, J. M. Hutchison, R. J. Holiday, and F. F. Crim, J. Phys. Chem. **107**, 10490 (2003).

[272] M. L. Hause, Y. H. Yoon, and F. F. Crim, J. Chem. Phys. **125**, 174309 (2006).

[273] H. D. Bist, J. C. D. Brand, and D. R. Williams, J. Mol. Spectrosc. **24**, 402 (1967).

[274] R. Baer, D. M. Charutz, R. Kosloff, and M. Baer, J. Chem. Phys. **105**, 9141 (1996).

[275] A. L. Sobolewski, Chem. Phys. **115**, 469 (1987).

[276] C. Woywod, W. C. Livingood, and J. H. Frederick, J. Chem. Phys. **114**, 1631 (2001).